

CHARACTERIZING FAINT SUBMILLIMETER GALAXIES WITH CLUSTER
LENSING

A DISSERTATION SUBMITTED TO THE GRADUATE DIVISION OF THE
UNIVERSITY OF HAWAI'I IN PARTIAL FULFILLMENT OF THE
REQUIREMENTS FOR THE DEGREE OF

DOCTOR OF PHILOSOPHY

IN

ASTRONOMY

August 2017

By
Li-Yen Hsu

Dissertation Committee:

Lennox L. Cowie, Chairperson
Amy J. Barger
John G. Learned
David B. Sanders
Jonathan P. Williams

© Copyright 2017
by
Li-Yen Hsu
All Rights Reserved

To that astronomy textbook my undergraduate classmate gave to me ten years ago

Acknowledgements

Coming to Hawaii for a Ph.D. is one of the most special experiences in my life. It has been a wonderful journey but also not an easy one. The support of my family was very important for me to finish this dissertation. I would like to thank my thesis advisor, Len, who always pointed me to clear directions and made this thesis possible. I appreciate his guidance and patience for the past four years. Together with Len, Amy has also provided a lot of input on my work. Her ideas and suggestions had great impact on me. Both Len and Amy have given me enough assists and encouraged me to explore different possibilities. I would also like to thank my two 699 advisors, Harald Ebeling and Alan Stockton, as well as my advisors at IPAC, Caltech, Vandana Desai and Eric Murphy. Working with them was very great experience and helped me build my knowledge and skills in optical, near-infrared, X-ray, and radio astronomy. Finally, I would like to thank all my friends who have helped me or hanged out with me, including IfA class 2011, former IfA students, and other friends I met in Hawaii and California. They have made my last six years colorful and memorable.

Abstract

Based on the measurements of the integrated background light from extragalactic sources, it is known that about half of the starlight is absorbed by dust and re-radiated into the far-infrared (FIR). It is therefore important to study both the unobscured and dust-obscured populations of galaxies across cosmic time for a full picture of the star formation in our universe. At $z > 1$, the FIR emission from galaxies is redshifted to the submillimeter. However, surveys made with single-dish submillimeter telescopes are confusion limited at low fluxes (< 2 mJy at $850 \mu\text{m}$) and can only detect ultra-luminous galaxies. Consequently, we have little information about fainter submillimeter galaxies (SMGs), which are actually the major contributors to the submillimeter background light and therefore the dominant star-formers in the dusty universe. Determining how much these faint SMGs overlap the optically selected samples is critical to fully account for the cosmic star formation history. Observations of massive cluster fields are the best way to study faint galaxies, thanks to gravitational lensing. To explore the faint submillimeter population, we have been observing nine galaxy clusters with the SCUBA-2 camera on the James Clerk Maxwell Telescope. We also used interferometric observations with the Karl G. Jansky Very Large Array and the Submillimeter Array to determine the accurate positions of our detected sources. Our observations have discovered a population of faint SMGs that are undetected in deep radio, optical, and near-infrared images. This suggests that a significant fraction of the galaxies with infrared luminosities $< 10^{12} L_\odot$ may be hidden from optical surveys and would not be included in the UV star formation history.

Table of Contents

Acknowledgements	iv
Abstract	v
List of Tables	viii
List of Figures	x
Chapter 1: Introduction	1
1.1 Submillimeter Galaxies	1
1.2 The Limit of Wide-field Submillimeter Surveys	2
1.3 The Hawaii SCUBA-2 Lensing Cluster Survey	3
1.4 Counterpart Identification with Interferometric Observations	6
1.5 The Content of this Dissertation	6
Chapter 2: Number Counts at 450 and 850 microns	12
2.1 Introduction	12
2.2 Observations and Data Reduction	14
2.3 Number Counts	17
2.3.1 Pure Noise Maps	17
2.3.2 Source Extraction	17
2.3.3 Submillimeter Flux Ratios and Redshift Estimates	18
2.3.4 De-lensed Raw Number Counts	20
2.3.5 Simulations and Corrected Number Counts	21
2.3.6 Results	23

2.3.7	The Effect of Multiplicity	24
2.4	Discussion	28
2.4.1	Extragalactic Background Light	28
2.4.2	Redshift Distributions	33
2.5	Summary	35
Chapter 3: Radio-detected Faint Submillimeter Galaxies		51
3.1	Introduction	51
3.2	Data	53
3.2.1	SCUBA-2 Images	53
3.2.2	VLA Images	53
3.2.3	HST Images and Photometry	59
3.2.4	Spitzer Images and Photometry	59
3.2.5	Other Ancillary Data and Photometric Catalogs	60
3.3	Sample Selection	60
3.3.1	SCUBA-2 Source Extraction	60
3.3.2	Flux Deboosting	61
3.3.3	Confusion Limit at $850\ \mu\text{m}$	62
3.3.4	VLA Source Extraction	63
3.3.5	Counterpart Identification at 3 GHz	64
3.3.6	Lens Models	66
3.4	Properties of Radio-detected Submillimeter Sources	67
3.4.1	Dust Temperatures and IR SFRs	67
3.4.2	Radio SFRs	73
3.4.3	UV SFRs	75
3.4.4	$850\ \mu\text{m}$ Flux Density to SFR Conversion	76
3.4.5	Individual Sources	77
3.5	Detectability of the Submillimeter sources	80
3.5.1	Bias and Redshift Distribution	80

3.5.2	Optical-near-infrared Colors	83
3.6	Summary	84
Chapter 4: SMA-detected Faint Submillimeter Galaxies		99
4.1	Introduction	99
4.2	Data	100
4.2.1	SCUBA-2 Observations	100
4.2.2	SMA Observations	100
4.2.3	HST and Spitzer Images	102
4.2.4	K_s -band Images	104
4.2.5	VLA Images	105
4.3	Results	105
4.3.1	SMA Detections and Multi-wavelength Counterparts	105
4.3.2	Redshift Estimates	106
4.3.3	Lens Models	109
4.4	Discussion	110
4.5	Summary	116
Chapter 5: Conclusions and Future Directions		126
Appendix: Simulations for Submillimeter Number Counts, Flux Ratios, and Source Plane Redshift Estimates		133

List of Tables

1.1	Coordinates of the Nine Cluster Fields and a Summary of Their SCUBA-2 Observations through March 2017	4
2.1	Summary of JCMT/SCUBA-2 Observations	16
2.2	The Combined Differential Number Counts at 450 μm and 850 μm	25
2.3	Best-fit Broken Power Laws for the Combined Differential Number Counts at 450 μm and 850 μm	26
3.1	Summary of JCMT/SCUBA-2 Observations	55
3.2	Summary of VLA Observations, Including Calibrators and the On-source Integration Times for Each Configuration/band Pairings.	57
3.3	Synthesized Beams of the 3 and 6 GHz Images for Each Field	59
3.4	Coordinates and Redshifts, As Well As SCUBA-2 and VLA Flux Densities of the 3 GHz Identified Sample of 850 μm Sources	68
3.5	Lens Models Used for Each Source and the Resulting Magnification Value .	69
3.6	<i>Herschel</i> and ALMA 1.1 mm Flux Densities from Rawle et al. (2016) and González-López et al. (2017)	71
3.7	Dust Temperatures, IR Luminosities, and SFRs	72
4.1	Summary of JCMT/SCUBA-2 Observations	101
4.2	Summary of SMA Observations	103

4.3	Synthesized Beam Sizes and Position Angles As Well As Central Sensitivities of the SMA Images	104
4.4	Positions and Flux Densities of the SCUBA-2 Sources and Their SMA Detections	106
4.5	Lens Models Used for Each Cluster Field	111
4.6	Redshifts, Lensing Magnifications, De-lensed Submillimeter Flux Densities, and Observed K_s -band Magnitudes of the SMA Sources	112

List of Figures

1.1	Distributions of the observed and estimated intrinsic fluxes for the 450 μm and 850 μm sources	5
2.1	850 μm -to-450 μm and 450 μm -to-850 μm flux ratios as functions of $(\text{S}/\text{N})_{450\mu\text{m}} \times (\text{S}/\text{N})_{850\mu\text{m}}$	18
2.2	Differential number counts for individual fields	21
2.3	Combined differential number counts	22
2.4	Comparison of SCUBA-2 850 μm flux and SMA 860 μm flux for sources in CDF-N	27
2.5	CDF-N 850 μm differential number counts for the SMA observed SCUBA-2 sources	28
2.6	Cumulative EBL as a function of flux at 450 and 850 μm	29
2.7	Combined differential number counts multiplied by the flux	30
2.8	850 μm -to-450 μm flux ratio as a function of 450 μm flux and 450 μm -to-850 μm flux ratio as a function of 850 μm flux	31
3.1	850 μm and 450 μm S/N maps	54
3.2	Boosting factor as a function of detection S/N for MACS J0416.1-2403 . . .	64
3.3	3 GHz and <i>HST</i> /ACS false-color images for the 3 GHz identified sample of SCUBA-2 sources	70
3.4	FIR SEDs of the 3 GHz identified sample of SCUBA-2 sources	74
3.4	(Continued)	75

3.5	Comparison between the radio SFRs and the IR+UV SFRs	76
3.6	Comparison between the 850 μm flux densities and IR SFRs/luminosities	78
3.7	K_s -band images of 0416-4 and 0717-2	80
3.8	Close-up <i>HST</i> /ACS false-color image of 0717-1	81
3.9	Counterpart identification rate as a function of observed 850 μm flux density	81
3.10	Expected observed 3 GHz flux density as a function of redshift with different observed 850 μm flux densities	83
3.11	$K - 4.5 \mu\text{m}$ color versus redshift	84
4.1	Multi-wavelength images for the SMA-detected SMGs	107
4.1	(Continued)	108
4.2	K_s -to-870 μm flux ratios versus 870 μm flux densities for (sub)millimeter- identified SMGs	113
4.3	K_s -to-850 μm flux ratios versus 850 μm flux densities for radio-identified SMGs	114
4.4	Histograms of the K_s -to-870 μm flux ratios	115
A1	Comparison of input and recovered median submillimeter flux ratios	135

Chapter 1

Introduction

1.1 Submillimeter Galaxies

Understanding how the most massive galaxies formed and how the star formation rate (SFR) density of the universe evolves with cosmic time (i.e., star formation history; see Madau & Dickinson 2014) is crucial to constrain the models for galaxy formation and evolution. The discovery of the far-infrared (FIR) Extragalactic Background Light (EBL) had demonstrated that about half of the starlight at optical and ultraviolet (UV) wavelengths are absorbed by dust and re-radiated into the FIR (Puget et al. 1996; Fixsen et al. 1998; Dole et al. 2006). Thus, it is important to study both the unobscured and dust-obscured populations of galaxies across cosmic time for a full accounting of the cosmic star formation history.

At $z > 1$, the rest-frame FIR light is redshifted into submillimeter wavelengths. Surveys made with single-dish telescopes have resolved the submillimeter background into distinct sources, a population of submillimeter galaxies (SMGs; reviewed by Blain et al. 2002 and Casey et al. 2014). SMGs are some of the most massively star-forming galaxies in the universe, many of which cannot be easily picked out in the rest-frame UV or optical samples due to their high dust extinction. Many studies have shown that SMGs contribute a significant fraction of the star formation at high redshifts (e.g., Barger et al. 2000, 2012, 2014; Chapman et al. 2005; Wang et al. 2006; Serjeant et al. 2008; Wardlow et al. 2011;

Casey et al. 2013; Cowie et al. 2017). Mapping these galaxies is therefore key to understand the dust-obscured portion of the star formation history and galaxy evolution as a whole. In addition, submillimeter flux remains almost invariant over $z \sim 1\text{--}8$ due to the negative K -correction of the thermal dust emission at submillimeter wavelengths, making high-redshift galaxies easier to detect in the submillimeter than at other wavelengths such as radio and optical.

1.2 The Limit of Wide-field Submillimeter Surveys

Direct searches for SMGs using interferometry are very inefficient due to the small field of views. Therefore, deep and wide-field surveys with single-dish submillimeter/FIR telescopes are the most efficient approach to search for SMGs. The SCUBA-2 camera (Holland et al. 2013) on the James Clerk Maxwell Telescope (JCMT) is currently the most powerful instrument for such observations. It covers 16 times the area of the previous SCUBA camera (Holland et al. 1999) and has the fastest mapping speed at 450 and 850 μm among the instruments at the same wavelengths. Additionally, JCMT has better angular resolution (beam FWHM $\sim 7''.5$ at 450 μm and $\sim 14''.5$ at 850 μm) than other single-dish telescopes such as the *Herschel Space Observatory* (Pilbratt et al. 2010) and the Atacama Pathfinder Experiment (APEX; Güsten et al. 2006).

However, blank-field observations with even the 15-meter JCMT become confusion limited (Condon 1974) at < 2 mJy at 850 μm . The confusion limits arise because the low spatial resolution of single-dish telescopes leads to blending of multiple faint sources within a single beam. This prevents the detection of fainter galaxies with infrared luminosities $< 10^{12}L_\odot$. As a result, there is little information about fainter SMGs, which actually contribute $\sim 80\%$ of the 850 μm EBL (e.g., Chen et al. 2013; Hsu et al. 2016) and therefore most of the dusty star formation. The goal of this dissertation is to understand these sources in detail and place them in the context of galaxy selections at other wavelengths.

1.3 The Hawaii SCUBA-2 Lensing Cluster Survey

Observations of massive lensing cluster fields are the best way to reach fainter detection limits, thanks to gravitational lensing. Lensed sources are magnified at all wavelengths, and their images benefit from enhanced spatial resolution. In addition, cluster member galaxies are typically quiescent galaxies at $z \sim 0.5$ which do not have much dust emission, making clusters transparent lenses in the submillimeter. We have been undertaking a program, the Hawaii SCUBA-2 Lensing Cluster Survey, to map nine massive clusters, including the northern five clusters in the *HST* Frontier Fields program (Lotz et al. 2017). Our observations were carried out in band 1 ($\tau_{225\text{GHz}} < 0.05$), band 2 ($0.05 < \tau_{225\text{GHz}} < 0.08$), or good band 3 ($0.08 < \tau_{225\text{GHz}} < 0.1$) weather conditions. Table 1.1 summarizes the coordinates of these clusters and our observations through March 2017. Other ancillary data of these fields include images taken with the Subaru telescope, the *Spitzer* and *Herschel Observatories*, and the Karl G. Jansky Very Large Array (VLA).

This program provides the largest sample of faint SMGs ever for interferometric follow-up and multi-wavelength studies. So far we have detected more than 200 450 μm sources and 900 850 μm sources above a 4σ detection threshold. Figure 1.1 shows the distribution of the observed and estimated intrinsic fluxes of the sources in all the nine fields. Thanks to the lensing amplification, we are able to detect sources down to intrinsic fluxes of ~ 1 mJy at 450 μm and ~ 0.1 mJy at 850 μm , which are much lower than the luminosities probed by all the other surveys including *Spitzer*, *Herschel*, ALMA LABOCA (ALESS; Hodge et al. 2013) surveys and the ALMA 1.3 mm imaging of the Hubble Ultra Deep Field (Dunlop et al. 2017). Our primary selection is performed at 850 μm since the stronger K -correction effect at this band results in a wider redshift range of the detected sources. Nevertheless, 450 μm data are also very useful. 450 μm detections associated with the 850 μm sources provide not only another set of flux measurements for constructing the FIR spectral energy distributions (SEDs), but also smaller positional uncertainties.

Table 1.1: Coordinates of the Nine Cluster Fields and a Summary of Their SCUBA-2 Observations through March 2017

Fields	R.A.	Decl.	Exposure (hr)	σ_{850} (mJy/beam)	σ_{450}
A2744	00 14 21.2	-30 23 50.1	4.6/10.0/2.5	0.65	10.5
A370	02 39 53.1	-01 34 35.0	28.5/1.5/7.0	0.38	2.58
MACS J0416.1-2403	04 16 08.9	-24 04 28.7	24.5/2.0/4.0	0.35	2.30
MACS J0717.5+3745	07 17 34.0	37 44 49.0	32.2/10.5/1.5	0.31	1.95
MACS J1149.5+2223	11 49 36.3	22 23 58.1	29.0/3.5/3.4	0.30	1.63
A1689	13 11 29.0	-01 20 17.0	22.4/1.9/0	0.39	2.34
RXJ1347.5-1145	13 47 30.5	-11 45 09.0	24.5/3.5/2.9	0.33	1.90
MACS J1423.8+2404	14 23 48.3	24 04 47.0	36.5/20.5/1.6	0.28	1.86
A2390	21 53 36.8	17 41 44.2	17.4/36.0/9.0	0.32	2.84

Clusters in bold text are *HST* Frontier Fields. Observed hours in band 1/2/3 weather are shown in Column 4. Columns 5 and 6 are the sensitivities at the centers of the 850 μm and 450 μm images.

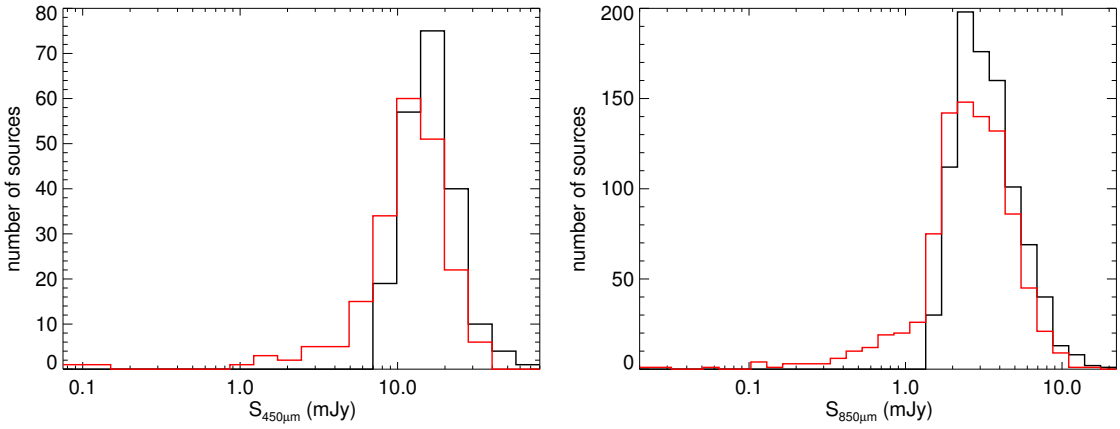


Figure 1.1: Distributions of the observed fluxes (black histograms) and the estimated intrinsic fluxes (red histograms) for the $450\mu\text{m}$ (left) and $850\mu\text{m}$ (right) sources, assuming source planes at $z = 2.2$ and $z = 2.8$, respectively (Hsu et al. 2016; Chapter 2). The lens models we use here are from Limousin et al. (2007) for A1689, Richard et al. (2010) for A2390, Limousin et al. (2010) for MACS J1423.8+2404, the Cluster Lensing And Supernova survey with Hubble (CLASH) archive for RXJ1347.5–1145, and the *HST* Frontier Field archive (the CATS team) for the five Frontier Fields. While the individual magnifications may have substantial uncertainties caused by models, source positions and redshifts, on average these effects should not change the overall flux distributions too much.

1.4 Counterpart Identification with Interferometric Observations

Identifying the correct counterparts to SMGs at other wavelengths is always challenging because single-dish submillimeter telescopes suffer large positional uncertainties due to their low spatial resolution. Traditionally, radio interferometric images (primarily 1.4 GHz surveys with the VLA; e.g., Ivison et al. 2002; Chapman et al. 2003) and mid-infrared (MIR) observations (primarily *Spitzer*/MIPS 24 μm images; e.g., Pope et al. 2006; Dye et al. 2008) are used to measure the positions of SMGs. However, these methods are biased against faint and/or very high-redshift SMGs since the emission at these wavelengths do not benefit from a negative K -correction. The completeness of radio identification depends on the depth of the radio images as well as the faintness of the SMGs. The variety of MIR spectral types in galaxies is large and does not always map directly to the FIR luminosity. Submillimeter interferometry is therefore a more reliable way to identify the correct counterparts to faint SMGs. It is also a way to confirm whether a submillimeter source is a single object or a blend of multiples. Nevertheless, radio interferometry is still an effective alternative for bright SMGs since submillimeter interferometry is observationally more expensive. In this dissertation, we use both the VLA and the Submillimeter Array (SMA; Ho et al. 2004) to identify our SCUBA-2 sources.

1.5 The Content of this Dissertation

Because of the confusion limits of blank-field surveys, most of the SMGs in the literature and the extinction-corrected UV population are disjoint (e.g., Barger et al. 2014; Cowie et al. 2017). We wish to make direct comparison between the two populations in the same SFR regime and determine the fraction of faint SMGs that are already included in the UV-inferred star formation history. Observations of cluster fields will allow us to probe this nearly unexplored submillimeter flux regime where the current sample size is very small.

We present deep submillimeter number counts using the SCUBA-2 data of both cluster and blank fields in Chapter 2. Because of the lensing magnification, our measurements highly constrain the number counts at fluxes fainter than 1 mJy and 0.2 mJy at 450 and 850 μ m, respectively. Integrating our counts shows that the majority of the EBL at each wavelength is contributed by faint sources with $L_{\text{IR}} < 10^{12}L_{\odot}$, corresponding to luminous infrared galaxies (LIRGs) or normal galaxies. In Chapter 3, we cross-match SCUBA-2 maps with 3 and 6 GHz images from the Janksy-VLA Frontier Fields Legacy Survey for three *HST* Frontier Fields. Within the *HST*/ACS coverage, we found radio detections for about one-third of the lensed 850 μ m sources. These radio-identified faint SMGs have lower redshift distribution and lower dust temperatures than the brighter SMGs in the literature. However, the fact that about two-thirds of the sources are not detected in the VLA images illustrates the need of submillimeter interferometry to obtain a complete and unbiased sample of faint SMGs. Chapter 4 presents our SMA follow-ups of faint SMGs in cluster fields. Based on the near-infrared-to-submillimeter flux ratios of these sources, most of them are extremely dusty and/or at very high redshifts. This suggests that many faint SMGs are missed by optical surveys and would not be included in the UV star formation history. Finally, we summarize the conclusions of this dissertation and the future directions for the studies of faint SMGs.

References

- Barger, A. J., Cowie, L. L., Chen, C.-C., Owen, F. N., Wang, W.-H., Casey, C. M., Lee, N., Sanders, D. B., & Williams, J. P. 2014, ApJ, 784, 9
- Barger, A. J., Cowie, L. L., & Richards, E. A. 2000, AJ, 119, 2092
- Barger, A. J., Wang, W.-H., Cowie, L. L., Owen, F. N., Chen, C.-C., & Williams, J. P. 2012, ApJ, 761, 89
- Blain, A. W., Smail, I., Ivison, R. J., Kneib, J.-P., & Frayer, D. T. 2002, Phys. Rep., 369, 111
- Casey, C. M., Chen, C.-C., Cowie, L., Barger, A., Capak, P., Ilbert, O., Koss, M., Lee, N., Le Floc'h, E., Sanders, D. B., & Williams, J. P. 2013, MNRAS, 436, 1919
- Casey, C. M., Narayanan, D., & Cooray, A. 2014, Phys. Rep., 541, 45
- Chapman, S. C., Blain, A. W., Ivison, R. J., & Smail, I. R. 2003, Nature, 422, 695
- Chapman, S. C., Blain, A. W., Smail, I., & Ivison, R. J. 2005, ApJ, 622, 772
- Chen, C.-C., Cowie, L. L., Barger, A. J., Casey, C. M., Lee, N., Sanders, D. B., Wang, W.-H., & Williams, J. P. 2013, ApJ, 776, 131
- Condon, J. J. 1974, ApJ, 188, 279
- Cowie, L. L., Barger, A. J., Hsu, L.-Y., Chen, C.-C., Owen, F. N., & Wang, W.-H. 2017, ApJ, 837, 139

- Dole, H., Lagache, G., Puget, J.-L., Caputi, K. I., Fernández-Conde, N., Le Floc'h, E., Papovich, C., Pérez-González, P. G., Rieke, G. H., & Blaylock, M. 2006, A&A, 451, 417
- Dunlop, J. S., McLure, R. J., Biggs, A. D., Geach, J. E., Michałowski, M. J., Ivison, R. J., Rujopakarn, W., van Kampen, E., Kirkpatrick, A., Pope, A., Scott, D., Swinbank, A. M., Targett, T. A., Artxaga, I., Austermann, J. E., Best, P. N., Bruce, V. A., Chapin, E. L., Charlot, S., Cirasuolo, M., Coppin, K., Ellis, R. S., Finkelstein, S. L., Hayward, C. C., Hughes, D. H., Ibar, E., Jagannathan, P., Khochfar, S., Koprowski, M. P., Narayanan, D., Nyland, K., Papovich, C., Peacock, J. A., Rieke, G. H., Robertson, B., Vernstrom, T., Werf, P. P. v. d., Wilson, G. W., & Yun, M. 2017, MNRAS, 466, 861
- Dye, S., Eales, S. A., Artxaga, I., Serjeant, S., Dunlop, J. S., Babbedge, T. S. R., Chapman, S. C., Cirasuolo, M., Clements, D. L., Coppin, K. E. K., Dunne, L., Egami, E., Farrah, D., Ivison, R. J., van Kampen, E., Pope, A., Pridley, R., Rieke, G. H., Schael, A. M., Scott, D., Simpson, C., Takagi, T., Takata, T., & Vaccari, M. 2008, MNRAS, 386, 1107
- Fixsen, D. J., Dwek, E., Mather, J. C., Bennett, C. L., & Shafer, R. A. 1998, ApJ, 508, 123
- Güsten, R., Nyman, L. Å., Schilke, P., Menten, K., Cesarsky, C., & Booth, R. 2006, A&A, 454, L13
- Ho, P. T. P., Moran, J. M., & Lo, K. Y. 2004, ApJ, 616, L1
- Hodge, J. A., Karim, A., Smail, I., Swinbank, A. M., Walter, F., Biggs, A. D., Ivison, R. J., Weiss, A., Alexander, D. M., Bertoldi, F., Brandt, W. N., Chapman, S. C., Coppin, K. E. K., Cox, P., Danielson, A. L. R., Dannerbauer, H., De Breuck, C., Decarli, R., Edge, A. C., Greve, T. R., Knudsen, K. K., Menten, K. M., Rix, H.-W., Schinnerer, E., Simpson, J. M., Wardlow, J. L., & van der Werf, P. 2013, ApJ, 768, 91
- Holland, W. S., Bintley, D., Chapin, E. L., Chrysostomou, A., Davis, G. R., Dempsey, J. T., Duncan, W. D., Fich, M., Friberg, P., Halpern, M., Irwin, K. D., Jenness, T., Kelly, B. D., MacIntosh, M. J., Robson, E. I., Scott, D., Ade, P. A. R., Atad-Ettedgui,

- E., Berry, D. S., Craig, S. C., Gao, X., Gibb, A. G., Hilton, G. C., Hollister, M. I., Kycia, J. B., Lunney, D. W., McGregor, H., Montgomery, D., Parkes, W., Tilanus, R. P. J., Ullom, J. N., Walther, C. A., Walton, A. J., Woodcraft, A. L., Amiri, M., Atkinson, D., Burger, B., Chuter, T., Coulson, I. M., Doriese, W. B., Dunare, C., Economou, F., Niemack, M. D., Parsons, H. A. L., Reintsema, C. D., Sibthorpe, B., Smail, I., Sudiwala, R., & Thomas, H. S. 2013, MNRAS, 430, 2513
- Holland, W. S., Robson, E. I., Gear, W. K., Cunningham, C. R., Lightfoot, J. F., Jenness, T., Ivison, R. J., Stevens, J. A., Ade, P. A. R., Griffin, M. J., Duncan, W. D., Murphy, J. A., & Naylor, D. A. 1999, MNRAS, 303, 659
- Hsu, L.-Y., Cowie, L. L., Chen, C.-C., Barger, A. J., & Wang, W.-H. 2016, ApJ, 829, 25
- Ivison, R. J., Greve, T. R., Smail, I., Dunlop, J. S., Roche, N. D., Scott, S. E., Page, M. J., Stevens, J. A., Almaini, O., Blain, A. W., Willott, C. J., Fox, M. J., Gilbank, D. G., Serjeant, S., & Hughes, D. H. 2002, MNRAS, 337, 1
- Limousin, M., Ebeling, H., Ma, C.-J., Swinbank, A. M., Smith, G. P., Richard, J., Edge, A. C., Jauzac, M., Kneib, J.-P., Marshall, P., & Schrabbback, T. 2010, MNRAS, 405, 777
- Limousin, M., Richard, J., Jullo, E., Kneib, J.-P., Fort, B., Soucail, G., Elíasdóttir, Á., Natarajan, P., Ellis, R. S., Smail, I., Czoske, O., Smith, G. P., Hudelot, P., Bardeau, S., Ebeling, H., Egami, E., & Knudsen, K. K. 2007, ApJ, 668, 643
- Lotz, J. M., Koekemoer, A., Coe, D., Grogin, N., Capak, P., Mack, J., Anderson, J., Avila, R., Barker, E. A., Borncamp, D., Brammer, G., Durbin, M., Gunning, H., Hilbert, B., Jenkner, H., Khandrika, H., Levay, Z., Lucas, R. A., MacKenty, J., Ogaz, S., Porterfield, B., Reid, N., Robberto, M., Royle, P., Smith, L. J., Storrie-Lombardi, L. J., Sunnquist, B., Surace, J., Taylor, D. C., Williams, R., Bullock, J., Dickinson, M., Finkelstein, S., Natarajan, P., Richard, J., Robertson, B., Tumlinson, J., Zitrin, A., Flanagan, K., Sembach, K., Soifer, B. T., & Mountain, M. 2017, ApJ, 837, 97
- Madau, P. & Dickinson, M. 2014, ARA&A, 52, 415

- Pilbratt, G. L., Riedinger, J. R., Passvogel, T., Crone, G., Doyle, D., Gageur, U., Heras, A. M., Jewell, C., Metcalfe, L., Ott, S., & Schmidt, M. 2010, *A&A*, 518, L1
- Pope, A., Scott, D., Dickinson, M., Chary, R.-R., Morrison, G., Borys, C., Sajina, A., Alexander, D. M., Daddi, E., Frayer, D., MacDonald, E., & Stern, D. 2006, *MNRAS*, 370, 1185
- Puget, J.-L., Abergel, A., Bernard, J.-P., Boulanger, F., Burton, W. B., Desert, F.-X., & Hartmann, D. 1996, *A&A*, 308, L5
- Richard, J., Smith, G. P., Kneib, J.-P., Ellis, R. S., Sanderson, A. J. R., Pei, L., Targett, T. A., Sand, D. J., Swinbank, A. M., Dannerbauer, H., Mazzotta, P., Limousin, M., Egami, E., Jullo, E., Hamilton-Morris, V., & Moran, S. M. 2010, *MNRAS*, 404, 325
- Serjeant, S., Dye, S., Mortier, A., Peacock, J., Egami, E., Cirasuolo, M., Rieke, G., Borys, C., Chapman, S., Clements, D., Coppin, K., Dunlop, J., Eales, S., Farrah, D., Halpern, M., Mauskopf, P., Pope, A., Rowan-Robinson, M., Scott, D., Smail, I., & Vaccari, M. 2008, *MNRAS*, 386, 1907
- Wang, W.-H., Cowie, L. L., & Barger, A. J. 2006, *ApJ*, 647, 74
- Wardlow, J. L., Smail, I., Coppin, K. E. K., Alexander, D. M., Brandt, W. N., Danielson, A. L. R., Luo, B., Swinbank, A. M., Walter, F., Weiβ, A., Xue, Y. Q., Zibetti, S., Bertoldi, F., Biggs, A. D., Chapman, S. C., Dannerbauer, H., Dunlop, J. S., Gawiser, E., Ivison, R. J., Knudsen, K. K., Kovács, A., Lacey, C. G., Menten, K. M., Padilla, N., Rix, H.-W., & van der Werf, P. P. 2011, *MNRAS*, 415, 1479

Chapter 2

Number Counts at 450 and 850 microns

Note: This chapter originally appeared as Hsu et al. (2016), with co-authors Lennox L. Cowie, Chian-Chou Chen, Amy J. Barger, and Wei-Hao Wang.

2.1 Introduction

FIR and submillimeter number counts provide fundamental constraints on empirical models (e.g., Valiante et al. 2009; Béthermin et al. 2011) and semi-analytical simulations (Hayward et al. 2013a,b; Cowley et al. 2015; Lacey et al. 2015) for galaxy evolution. Many measurements of the submillimeter number counts were made with SCUBA (Smail et al. 1997; Hughes et al. 1998; Barger et al. 1999; Eales et al. 1999, 2000; Cowie et al. 2002; Scott et al. 2002; Smail et al. 2002; Borys et al. 2003; Serjeant et al. 2003; Webb et al. 2003; Wang et al. 2004; Coppin et al. 2006; Knudsen et al. 2008; Zemcov et al. 2010). Similar results have been obtained with other single-dish telescopes and instruments, such as *Herschel* (Oliver et al. 2010; Berta et al. 2011), the Large APEX Bolometer Camera (LABOCA; Siringo et al. 2009) at 870 μm on the Atacama Pathfinder Experiment (APEX; Güsten et al. 2006; Weiß et al. 2009), and the AzTEC camera (Wilson et al. 2008) at 1.1 mm on both the JCMT (e.g., Perera et al. 2008; Austermann et al. 2009, 2010) and the Atacama Submillimeter Telescope Experiment (ASTE, Ezawa et al. 2004; e.g., Scott et al. 2010, 2012; Arétxaga et al. 2011; Hatsukade et al. 2011).

The biggest challenge for measuring the FIR number counts is the poor spatial resolution of single-dish telescopes. For example, the beamsize of the JCMT at 850 μm is $\sim 14''$; for *Herschel*, it is 18'', 26'', and 36'' at 250 μm , 350 μm , and 500 μm , respectively. Poor resolution imposes a fundamental limitation, the confusion limit (Condon 1974), preventing us from resolving faint sources that contribute the majority of the EBL. Another issue caused by the poor resolution is source blending. Interferometric observations (e.g., Wang et al. 2011; Barger et al. 2012; Smolčić et al. 2012; Hodge et al. 2013; Bussmann et al. 2015; Simpson et al. 2015) and semi-analytical models (Hayward et al. 2013a,b; Cowley et al. 2015) have shown that close pairs within the large beam sizes are common.

Observations of massive galaxy clusters can push the detection limits toward fainter sources, thanks to gravitational lensing effects (e.g., Smail et al. 1997, 2002; Cowie et al. 2002; Knudsen et al. 2008; Johansson et al. 2011; Chen et al. 2013a,b), though the positional uncertainties still cause large uncertainties in the lensing amplifications and the intrinsic fluxes (Chen et al. 2011). Serendipitous detection obtained within the deep, high-resolution ($\sim 1''$) imaging taken by the Atacama Large Millimeter/submillimeter Array (ALMA) has allowed several measurements of number counts at 870 μm (Karim et al. 2013; Simpson et al. 2015), 1.1 mm (Carniani et al. 2015), 1.2 mm (Ono et al. 2014; Fujimoto et al. 2016) and 1.3 mm (Hatsukade et al. 2013; Carniani et al. 2015). However, the small-scale clustering between the random detections and the main targets may bias the counts (e.g., Oteo et al. 2016). Unbiased measurements of submillimeter and millimeter number counts with ALMA still require imaging large areas of the sky (Hatsukade et al. 2016).

The SCUBA-2 camera (Holland et al. 2013) on the JCMT is currently the most powerful instrument to search for SMGs in wide fields. It covers 16 times the area of the previous SCUBA camera and has the fastest mapping speed at 450 μm and 850 μm among all the single-dish FIR telescopes. Here we present the 450 μm and 850 μm number counts constructed based on the SCUBA-2 observations of six cluster fields, A1689, A2390, A370, MACS J0717.5+3745, MACS J1149.5+2223, and MACS J1423.8+2404. To constrain the bright-end counts, we also include data from three blank fields, CDF-N, CDF-S, and

COSMOS. We combine our measurements from all these fields in order to explore the widest possible flux range. This chapter is structured as follows. The details of the observations and data reduction are described in Section 4.2. In Section 2.3, we explain our methodology for constructing the number counts and present our results. We discuss our results and their implications in Section 2.4. Section 2.5 summarizes our results. Throughout this chapter, we assume the concordance Λ CDM cosmology with $H_0 = 70 \text{ km s}^{-1} \text{ Mpc}^{-1}$, $\Omega_M = 0.27$, and $\Omega_\Lambda = 0.73$ (Larson et al. 2011).

2.2 Observations and Data Reduction

We combined all of our SCUBA-2 data taken between October 2011 and January 2015, as well as the archival data of A1689 (PI: Holland) and COSMOS (PI: Casey; Casey et al. 2013). We used the CV DAISY scan pattern to observe our cluster fields, which detects sources out to a radius of $\sim 6'$ and therefore covers the strong lensing regions of the clusters. We also used the PONG-900 scan pattern on the two CDF fields in order to cover larger areas to find rarer bright sources. Most of our observations were carried out under band 1 (the driest weather; $\tau_{225\text{GHz}} < 0.05$) or band 2 ($0.05 < \tau_{225\text{GHz}} < 0.08$) conditions, but there are also data taken under good band 3 conditions ($0.08 < \tau_{225\text{GHz}} < 0.1$). The archival data of A1689 and COSMOS were taken under band 1 conditions with the CV DAISY and PONG-900 modes, respectively. We summarize the details of these observations in Table 2.1.

Following Chen et al. (2013a,b), we reduced the data using the Dynamic Iterative Map Maker (DIMM) in the SMURF package from the STARLINK software (Chapin et al. 2013). DIMM performs pre-processing and cleaning of the raw data (e.g., down-sampling, dark subtraction, concatenation, flat-fielding), as well as iterative estimations to remove different signals from astronomical signal and noise. We adopted the standard “blank field” configuration file, which is commonly used for extragalactic surveys to detect low signal-to-noise point sources. We ran DIMM on each bolometer subarray individually for a given scan and then used the MOSAIC_JCMT_IMAGES recipe from the Pipeline for Combing

and Analyzing Reduced Data (PICARD) to coadd the reduced subarray maps into a single scan map.

We then flux calibrated each scan with the primary calibrator observed closest in time (Dempsey et al. 2013). These calibrators are all compact bright sources such as Uranus, CRL618, CRL2688, and Arp220. We first reduced these calibrators with the “bright compact” configuration file and compared the derived flux conversion factors (FCFs) with the standard values provided in the SCUBA-2 data reduction manual (491 Jy pW⁻¹ at 450 μ m and 537 Jy pW⁻¹ at 850 μ m, derived with the “bright compact” configuration file). The resulting FCF values we obtained match these standard values to within 10%, confirming the reliability of the calibrators we used. We then reduced the calibrators again using the same method used for the science maps with the “blank field” configuration file to derive a new set of FCFs. The derived values are on average $\sim 16\%$ and 20% higher than the standard FCFs at 450 μ m and 850 μ m, respectively. We applied these FCFs to the the science scans.

After each scan was reduced and flux calibrated, we used MOSAIC_JCMT_IMAGES again to combine all the products into the final maps. Finally, to maximize the detectability of point sources, we applied a matched filter to our maps using the PICARD recipe SCUBA2_MATCHED_FILTER. Before running the matched filter, the recipe convolved the maps with a broad Gaussian and subtracted these maps from the original maps in order to remove low spatial frequency structures. We adopted the default FWHM values for the broad Gaussian (20'' at 450 μ m and 30'' at 850 μ m). The processed point-spread function (PSF) used for matched-filtering is a Gaussian with a convolved broader Gaussian subtracted off, which gives a Mexican-hat-like wavelet.

Table 2.1: Summary of JCMT/SCUBA-2 Observations

Field	RA	Dec	Scan Mode	Weather	Exposure (hr)	Survey Area (arcmin ²)	$\bar{\sigma}$ (mJy beam ⁻¹)
A1689	13 11 29.0	-01 20 17.0	CV DAISY	1+2	20.4+1.9	[120.2,125.3]	[4.44,0.69]
A2390	21 53 36.8	17 41 44.2	CV DAISY	1+2+3	11.4+21.5+9.0	[126.1,131.6]	[7.14,0.66]
A370	02 39 53.1	-01 34 35.0	CV DAISY	1+2+3	24.0+1.5+7.0	[121.5,125.9]	[5.46,0.73]
MACS J0717.5+3745	07 17 34.0	37 44 49.0	CV DAISY	1+2+3	24.2+3.5+1.5	[127.0,127.3]	[4.62,0.73]
MACS J1149.5+2223	11 49 36.3	22 23 58.1	CV DAISY	1+2+3	6.0+2.0+2.4	[−,121.9]	[−,1.23]
MACS J1423.8+2404	14 23 48.3	24 04 47.0	CV DAISY	1+2+3	9.0+8.5+1.6	[−,123.5]	[−,0.97]
CDF-N	12 36 49.0	62 13 53.0	CV DAISY+PONG-900	1+2+3	12.0+46.3+13.8	[−,429.8]	[−,1.44]
CDF-S	03 32 28.0	-27 48 30.0	CV DAISY+PONG-900	1+2+3	3.7+53.1+5.5	[−,314.3]	[−,1.75]
COSMOS	10 00 24.0	02 24 00.0	PONG-900	1	38.0	[379.5,377.3]	[5.65,0.99]

Columns 5 & 6: The weather conditions (band 1, 2, or 3) and the corresponding observed hours. Column 7: The total observed area that we used for source detection at 450 μm and 850 μm . The 450 μm data of MACS J1149, MACS J1423, CDF-N, and CDF-S are shallow and are not used for constructing the number counts. Note that for a cluster field, the effective area on the source plane would be smaller than the quoted value here. Column 8: Average 1 σ sensitivity within the survey area at 450 μm and 850 μm . These are the noise values measured from the reduced images, and the effect of confusion noise is not included.

2.3 Number Counts

2.3.1 Pure Noise Maps

In order to estimate the number of fake sources contaminating the number counts that we measured from our science maps, we need to generate source-free maps with only pure noise for each of our fields. These maps are sometimes referred to as jackknife maps in the literature. Following Chen et al. (2013a,b), we subtracted two maps that were each produced by coadding roughly half of the flux-calibrated data. In doing so, the real sources are subtracted off, and the residual maps are source-free maps. We then rescaled the value of each pixel by a factor of $\sqrt{t_1 \times t_2}/(t_1 + t_2)$, with t_1 and t_2 representing the integration time of each pixel from the two maps. Finally, we applied the matched-filter with the same procedure for the science maps.

2.3.2 Source Extraction

We have shown in previous work that sources detected above a 4σ level have a low contamination rate (Chen et al. 2013a,b). However, for computing number counts, we can use a lower detection threshold where there are still significantly more true sources than false detections. In Chen et al. (2013b), we extracted sources down to $\sim 2\sigma$. However, here we use 3σ as our detection threshold¹. We experimented with different detection thresholds and binning in order to extend the faint end of the counts while keeping good signal-to-noise ratio (S/N) throughout all the flux bins at the same time. We found that using 3σ leads to better S/N in the number counts than using lower thresholds, especially at the faint end.

We first generated the PSFs by averaging all the primary calibrators, the ones we used for deriving the FCFs. Following the methodology of source extraction in Chen et al. (2013a,b), we identified the pixel with the maximum S/N, subtracted this pixel and its surroundings using the PSF centered and scaled at the position and value of this pixel, and then searched for the next maximum S/N. We iterated this process until the 3σ threshold

¹Note that the confusion noise is not included in the flux errors of detected sources.

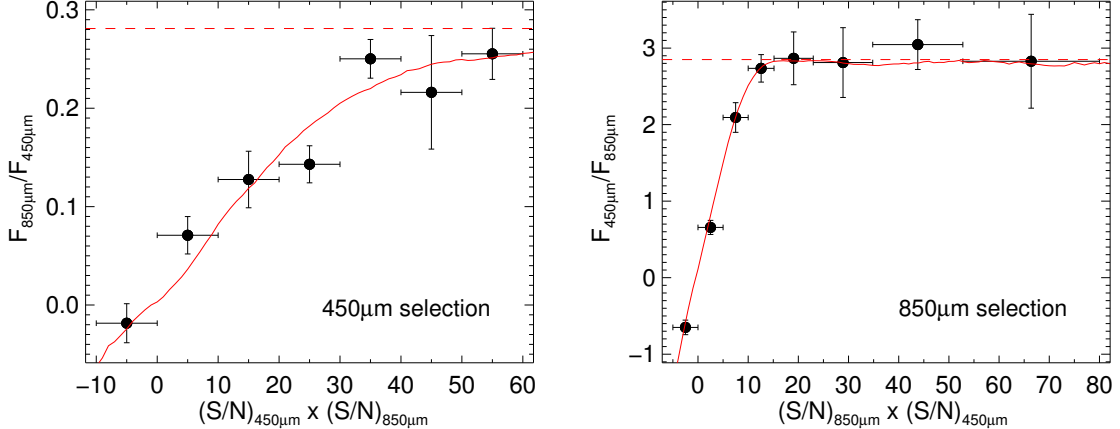


Figure 2.1: $850\mu\text{m}$ -to- $450\mu\text{m}$ (upper) and $450\mu\text{m}$ -to- $850\mu\text{m}$ (lower) flux ratios against $(S/N)_{450\mu\text{m}} \times (S/N)_{850\mu\text{m}}$ for 4σ detected sources in the cluster fields at $450\mu\text{m}$ and $850\mu\text{m}$, respectively. In each bin, we took the median of the flux ratios and calculated the error using bootstrapping. Note that for $850\mu\text{m}$ detected sources we use logarithmic bins at $(S/N)_{450\mu\text{m}} \times (S/N)_{850\mu\text{m}} > 10$ in order to improve the number statistics. We ran simulations in which we populated the source-free pure noise maps with sources with constant flux ratios. Red dashed lines are the input constant flux ratios (0.281 and 2.85) of the simulations, and the red solid lines are what we measured from the simulated maps, which show good agreement with our measurements from the science maps.

was hit. We ran the source extraction on both the science maps and the pure noise maps. The ratio of the total number of sources from the pure noise maps and from the science maps ($= N_{\text{false}}/N_{\text{total}}$) is $\sim 55\%$ (22%) at 450 (850) μm . The effect of false sources is subtracted in the computation of number counts, as we will describe in Section 2.3.4 and 2.3.5.

2.3.3 Submillimeter Flux Ratios and Redshift Estimates

In order to obtain the intrinsic flux of a lensed source, both the lens model of the cluster and the redshift of the source are required. However, since we do not have redshift measurements for individual sources, we simply adopted estimated median redshifts of the lensed $450\mu\text{m}$ and $850\mu\text{m}$ sources to compute our de-lensed number counts. Note that what we need to estimate are the “observed median redshifts” of the lensed populations, which would be higher than the real median redshifts of the distributions (e.g., Weiß et al. 2013). This is

because sources at higher redshifts have higher probability of being lensed and generally have higher lensing magnifications, causing a selection bias (e.g., Hezaveh & Holder 2011). We leave the discussion of the blank-field sources and their redshift distributions to Section 4.3.2.

We estimated the two median redshifts by exploring the flux ratios between 450 μm and 850 μm for all the 4σ detected sources in the cluster fields. At 450 (850) μm , we took the flux and position of a detected source and then measured the flux value at the same position on the 850 (450) μm map. In Figure 2.1, we plot the 850 μm -to-450 μm and 450 μm -to-850 μm flux ratios against the product of S/N at 450 μm and at 850 μm . In each bin of $(\text{S/N})_{450\mu\text{m}} \times (\text{S/N})_{850\mu\text{m}}$, we took the median of the flux ratios and calculated the error using bootstrapping. We can see that the flux ratio increases with increasing S/N product and then flattens. The lower (negative) measured flux ratios at lower (negative) $(\text{S/N})_{450\mu\text{m}} \times (\text{S/N})_{850\mu\text{m}}$ are a result of the mismatch between the positions of the 450 μm and 850 μm flux peaks due to lower S/N. We compared the measured flux ratios with what we measured from simulated maps, which were produced by populating the pure noise maps with sources with constant flux ratios. A detailed description of how we performed such simulations is left to the Appendix. In Figure 2.1, red dashed lines are the input constant flux ratios of the simulations, and the red solid lines are what we measured from the simulated maps, which show good agreement with our measurements from the science maps. We therefore conclude that the values of the two dashed lines correspond to the median flux ratios of the 450 μm and 850 μm selected populations in the cluster fields.

To convert flux ratios to redshifts, we assumed a modified blackbody spectral energy distribution (SED) of the form $S_\nu \propto (1 - e^{-\tau(\nu)})B_\nu(T)$, where $\tau(\nu) = (\nu/\nu_0)^\beta$ and $\nu_0 = 3000$ GHz. Assuming $\beta = 1.5$, we determined the redshifts from our estimated median flux ratios for a dust temperature of 30 K, 40 K, or 50 K. The corresponding redshifts for the 450 μm sources are $z \sim 1.5$, 2.2, or 2.8. At 850 μm , we obtained $z \sim 2.0$, 2.8, or 3.5. The final number counts shown in this chapter are based on source plane redshifts of 2.2 and 2.8 for 450 μm and 850 μm , respectively. We chose these values because they are the central values of the different SED models used. However, we will show in Section 2.3.6 that using

$z = 1.5$, 2.8 at $450\text{ }\mu\text{m}$ and $z = 2.0$, 3.5 at $850\text{ }\mu\text{m}$ does not change our results significantly, and that the computation of the number counts is not sensitive to the adopted source plane redshifts.

2.3.4 De-lensed Raw Number Counts

To compute the de-lensed, differential number counts, we corrected all the source fluxes in the cluster fields using the publicly available software LENSTOOL (Kneib et al. 1996), which allows us to generate magnification maps with the angular sizes of our SCUBA-2 maps. We therefore used the lens models from the LENSTOOL developers (CATS team) for A1689 (Limousin et al. 2007), A2390 (Richard et al. 2010), MACS J1423.8+2404 (Limousin et al. 2010), and the three Frontier Fields (Hubble Frontier Field archive²). For each source from a science or pure noise map, we calculated its number density by inverting the detectable area, which is the area in which this source can be detected above the 3σ threshold. For a source in a cluster field, the detectable area is defined on the source plane. We then computed the number counts by summing up the number densities of the sources in each flux bin with errors based on Poisson statistics (Gehrels 1986). Finally, we subtracted the counts of the pure noise maps from the counts of the science maps to produce the pure source counts.

While the discrepancy in the magnifications between different lens models can be a factor of a few at the cluster center, the effect on the measured number counts is not significant. This is the same as the effect caused by the different source plane redshifts, as we discussed in Section 2.3.3. Although there are uncertainties in the lens models, the source plane redshifts, and the positions of the submillimeter sources, the de-lensed flux and detectable area of a source are directly related, causing little change in the slope and normalization of the measured number counts.

²<https://archive.stsci.edu/pub/hlsp/frontier/>

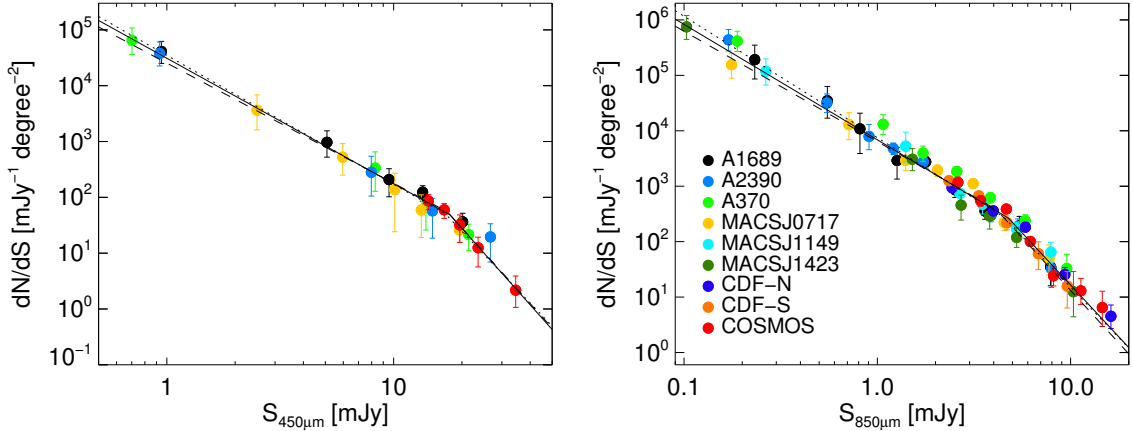


Figure 2.2: Differential number counts for all the fields at 450 μm (upper) and 850 μm (lower), assuming source plane redshifts of 2.2 (450 μm) and 2.8 (850 μm) for de-lensing. Solid lines are the best-fit broken power law models. Dotted lines are the best-fit models to the number counts computed with source plane redshifts of 1.5 and 2.0. Dashed lines are the best-fit models to the number counts computed with source plane redshifts of 2.8 and 3.5. We do not show the counts using these different source plane redshifts for clarity.

2.3.5 Simulations and Corrected Number Counts

The pure source counts we computed above, however, still do not represent the true underlying submillimeter populations because the fluxes of the sources are boosted and there is incompleteness. The cause of the flux boost is the statistical fluctuations of the flux measurements for flux-limited observations, known as the Eddington bias (Eddington 1913). Following Chen et al. (2013a,b), we ran Monte Carlo simulations to estimate the underlying count model at each wavelength. We first generated a simulated map by randomly populating sources in the pure noise map, drawn from an assumed model and convolved with the PSF. The count model we used is in the form of a broken power law

$$\frac{dN}{dS} = \begin{cases} N_0 \left(\frac{S}{S_0}\right)^{-\alpha} & \text{if } S \leq S_0 \\ N_0 \left(\frac{S}{S_0}\right)^{-\beta} & \text{if } S > S_0 \end{cases} \quad (2.1)$$

For the cluster fields, we populated the sources in the source plane and projected them onto the image plane using LENSTOOL.

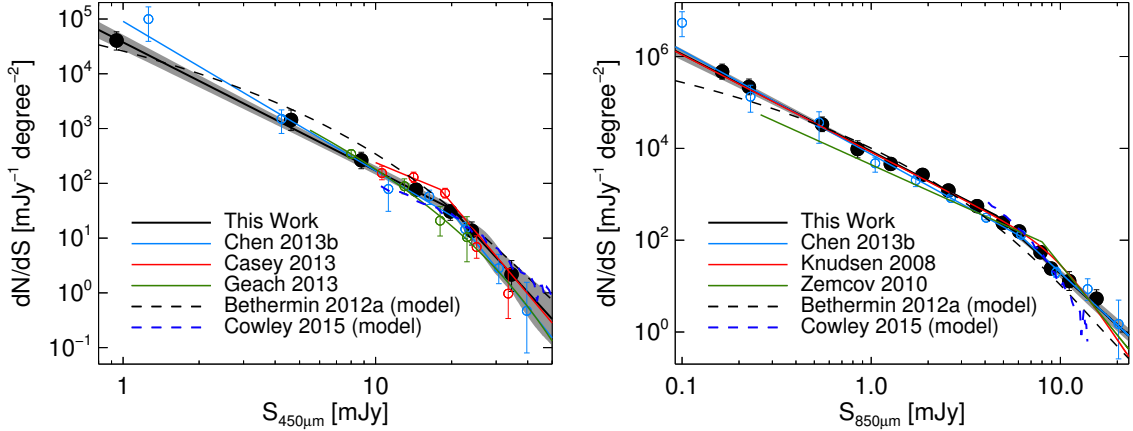


Figure 2.3: Combined differential number counts from all the available fields. Solid black lines are the best-fit broken power law models with 1σ error regions in gray shading. The values of the counts and the best-fit parameters are summarized in Table 2.2 and 2.3, respectively. In both panels, we show the best-fit count models for a few other observational results as colored solid lines, and the model predictions from Béthermin et al. (2012a) and Cowley et al. (2015) as black and purple dashed lines, respectively. For the observational results from the literature, the measured number counts are shown as colored circles if their values are available from these papers. Blue lines and circles are from Chen et al. (2013b). At 450 μ m, the results from Casey et al. (2013) and Geach et al. (2013) are shown in the upper panel as red and green lines/circles, respectively. At 850 μ m, two count models from SCUBA cluster surveys are plotted in the lower panel as red (Knudsen et al. 2008) and green (Zemcov et al. 2010) lines. Note that the original models from Cowley et al. (2015) are cumulative, and we converted these models to differential counts using flux intervals of 1 mJy and 0.2 mJy at 450 μ m and 850 μ m, respectively. Using smaller flux intervals would make the resulting differential counts less smooth.

For each simulated map we reran our source extraction and computed the recovered counts using the same method and flux bins used for the science map. We repeated the simulation 50 times for each input model and then averaged the recovered counts from these simulations. In order to measure the actual counts we adopted an iterative procedure. Using the ratios between the averaged recovered counts and the input counts, we renormalized the observed raw counts in each bin from the science map. We then did a χ^2 fit to the corrected observed counts using a broken power law. This fit was then used as the input model for the next iteration. We continued until the corrected counts matched the corrected counts of the previous iteration within 1σ throughout all the flux bins. It took only two or three iterations to converge for each field.

2.3.6 Results

We show the corrected number counts for all the fields together at both $450\text{ }\mu\text{m}$ and $850\text{ }\mu\text{m}$ in Figure 2.2. Thanks to the lensing magnification, we are able to detect counts down to fluxes fainter than 1 mJy and 0.2 mJy in several fields at $450\text{ }\mu\text{m}$ and $850\text{ }\mu\text{m}$, respectively. The solid lines represent the best-fit broken power law models for the counts. In each panel, we also show the best-fit model for the counts computed with a lower source plane redshift ($z = 1.5$ at $450\text{ }\mu\text{m}$ and $z = 2.0$ at $850\text{ }\mu\text{m}$) with the dotted line and the best-fit model to the counts computed with a higher source plane redshift ($z = 2.8$ at $450\text{ }\mu\text{m}$ and $z = 3.5$ at $850\text{ }\mu\text{m}$) with the dashed line. We can see that the results are not very sensitive to the assumed redshifts.

In order to better constrain our count model at each wavelength, we combined the counts from all the fields. The results are shown in Figure 2.3, which are weighted averages of the corrected counts from each field (black circles). We assigned a weight for each flux bin of a field in the following way. For each field, we used the final count model we obtained (Section 2.3.5) to run the same simulation 50 times and obtained the 1σ scatter of the recovered counts in each flux bin. We then normalized this scatter by the average of the recovered counts. The inverse square of the scatter is adopted as the weight. We also

show various results from the literature. The combined number counts and the best-fit parameters of the models are summarized in Table 2.2 and Table 2.3.

2.3.7 The Effect of Multiplicity

Semi-analytical simulations have shown that source blending could impact the number counts obtained from single-dish observations (Hayward et al. 2013a; Cowley et al. 2015). Some recent studies with ALMA observations have also discussed the effect of multiplicity on the number counts (Hodge et al. 2013; Karim et al. 2013; Simpson et al. 2015). In Chen et al. (2013b), we used the SMA detected sample in CDF-N (Barger et al. 2014) to obtain the multiple fraction as a function of flux at $S_{850\mu\text{m}} > 3.5$ mJy, and we computed the multiplicity-corrected CDF-N 850 μm number counts above 3.5 mJy, assuming that all the blends split into two equal components. There is one incorrect coefficient in Equation (4) of Chen et al. (2013b), which should instead be written as

$$\frac{dN_{\text{corr}}(S)}{dS} = \frac{dN_{\text{orig}}(S)}{dS} \times (1 - f_{\text{mul}}(S)) + f_{\text{mul}}(2S) \times 2 \times \frac{dN_{\text{orig}}(2S)}{dS}, \quad (2.2)$$

where f_{mul} is the multiple fraction of the SMA detected SCUBA-2 sources as a function of flux, and dN_{corr}/dS and dN_{orig}/dS are the multiplicity-corrected and the original SCUBA-2 counts, respectively³. However, this correction does not significantly change the result of Chen et al. (2013b). The systematic changes introduced by multiplicity are still smaller than the statistical errors of the counts.

Computing multiplicity corrections is difficult because the multiple fractions at different fluxes are still not well determined. For SCUBA-2 selected sources, Simpson et al. (2015) found a multiple fraction of $61^{+19}_{-15}\%$ (17 out of 28) at $S_{850\mu\text{m}} > 4$ mJy using ALMA, while Barger et al. (2014) found a multiple fraction of only $12.5^{+12.1}_{-6.8}\%$ (3 out of 24) at $S_{850\mu\text{m}} > 3.5$ mJy using SMA. The much lower multiple fraction from Barger et al. (2014) can be

³When the flux ratio of the doublets equals x/y , with $x + y = 1$, Equation (2) becomes $dN_{\text{corr}}(S)/dS = dN_{\text{orig}}(S)/dS \times (1 - f_{\text{mul}}(S)) + f_{\text{mul}}(S/x) \times dN_{\text{orig}}(S/x)/dS + f_{\text{mul}}(S/y) \times dN_{\text{orig}}(S/y)/dS$

Table 2.2: The Combined Differential Number Counts at 450 μm and 850 μm

$S_{450\mu\text{m}}$ (mJy)	dN/dS (mJy $^{-1}$ deg $^{-2}$)	$S_{850\mu\text{m}}$ (mJy)	dN/dS (mJy $^{-1}$ deg $^{-2}$)
0.94	40579^{+17834}_{-13496}	0.16	$468599^{+215679}_{-147442}$
4.63	1438^{+741}_{-510}	0.23	$217910^{+105487}_{-70715}$
8.77	$263.9^{+105.7}_{-79.2}$	0.55	33138^{+15129}_{-9975}
14.45	$76.58^{+18.52}_{-15.96}$	0.85	9650^{+4984}_{-3444}
19.76	$30.53^{+10.02}_{-9.39}$	1.27	4576^{+1114}_{-826}
24.05	$13.55^{+6.17}_{-6.09}$	1.87	2646^{+345}_{-309}
34.53	$2.17^{+1.72}_{-1.10}$	2.56	1209^{+140}_{-129}
		3.63	$552.1^{+47.6}_{-44.5}$
		4.96	$238.6^{+31.3}_{-24.8}$
		6.06	$155.4^{+18.8}_{-16.9}$
		7.85	$54.52^{+21.06}_{-13.99}$
		8.93	$24.16^{+6.12}_{-4.59}$
		11.14	$12.88^{+7.79}_{-4.84}$
		15.52	$5.31^{+3.02}_{-1.79}$

Table 2.3: Best-fit Broken Power Laws for the Combined Differential Number Counts at 450 μm and 850 μm

Wavelengths (μm)	N_0 ($\text{mJy}^{-1} \deg^{-2}$)	S_0 (mJy)	α	β
450	$33.3^{+44.0}_{-18.1}$	$20.1^{+6.8}_{-5.1}$	$2.34^{+0.14}_{-0.17}$	$5.06^{+5.03}_{-1.52}$
850	342^{+56}_{-80}	$4.59^{+0.26}_{-0.38}$	$2.12^{+0.06}_{-0.07}$	$3.73^{+0.59}_{-0.47}$

caused by the sensitivities of their SMA maps, which only allow detections of secondary SMGs brighter than 3 mJy. The multiple fraction is simply sensitive to the depth of the follow-up interferometric observations. However, Chen et al. (2013b) showed that most of the sources with a single SMA detection in CDF-N have flux measurements that statistically agree with those made by SCUBA-2. Using a larger SMA detected sample in CDF-N (31 4σ detected sources; Cowie et al. 2016, in preparation), we again compare the fluxes measured by SCUBA-2 and by SMA for the sources with a single SMA detection. We show the comparison in Figure 2.4. The two fluxes statistically agree with each other for most of the sources. The median flux ratio of SMA to SCUBA-2 is 0.96 ± 0.06 . This suggests that most secondary sources that are missed by SMA would be faint and unlikely to affect the bright-end counts. These sources would be unlikely to increase the faint-end counts significantly, either, since they contribute a small fraction of the faint sources based on the broken power law model.

Instead of computing the multiplicity corrections by assuming the multiple fractions, here we use another approach to examine the effect of multiplicity on the number counts. We took the SMA detected sample in CDF-N (Cowie et al. 2016, in preparation) and their corresponding SCUBA-2 sources to compute two sets of number counts. We corrected the SCUBA-2 counts for Eddington bias using simulations. For the SMA sources, we simply took their fluxes and computed the detectable areas and number counts as if they were detected in our SCUBA-2 map. Note that these sources comprise a incomplete sample at

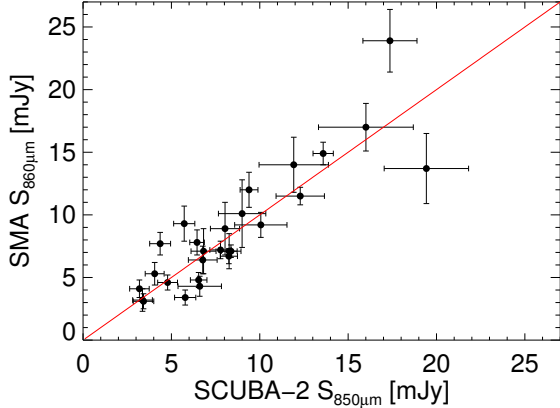


Figure 2.4: Comparison of SCUBA-2 850 μm flux and SMA 860 μm flux for the SCUBA-2 4σ detected sources in CDF-N with a single SMA detection.

$S_{850\mu\text{m}} > 3 \text{ mJy}$ because only 29 out of 81 SCUBA-2 sources above this flux (19 out of 29 at $S_{850\mu\text{m}} > 6 \text{ mJy}$) have SMA observations. We did not apply any completeness correction since we are only attempting to see whether there is a significant difference between these two sets of counts. The comparison is shown in Figure 2.5. We can see small deviations at both the faint and bright ends, but the two sets of counts are essentially consistent within their uncertainties.

Although Simpson et al. (2015) found a multiple fraction of 61% at $S_{850\mu\text{m}} > 4 \text{ mJy}$, their differential counts constructed from ALMA and SCUBA-2 still statistically agree with each other at $S_{870\mu\text{m}} \lesssim 15 \text{ mJy}$ (see their Figure 6). The effect of multiplicity is more obvious in the cumulative counts at $S_{870\mu\text{m}} \gtrsim 10 \text{ mJy}$. If we plot the cumulative EBL, the ALMA and SCUBA-2 results of Simpson et al. (2015) would deviate at $S_{870\mu\text{m}} > 5 \text{ mJy}$, which is well above the confusion limit of the JCMT. As we will discuss in Section 2.4.1, the majority of the EBL comes from sources fainter than our detection limits at both wavelengths, and this conclusion is not affected by multiplicity.

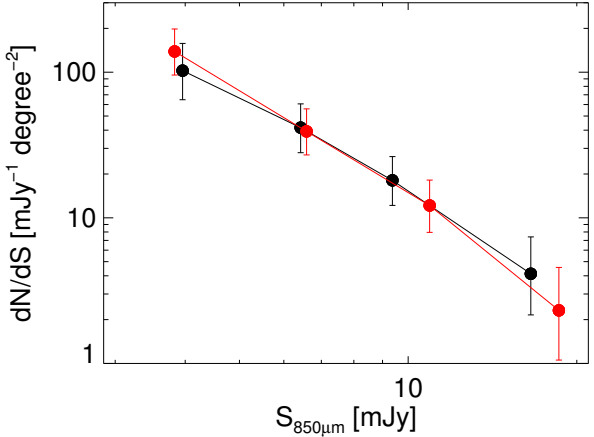


Figure 2.5: CDF-N 850 μm differential number counts for the SMA observed SCUBA-2 sources. The black and red circles represent the counts based on SCUBA-2 and SMA fluxes, respectively. These counts are lower than the counts for CDF-N shown in Figure 2.2 because we did not apply any completeness correction. Note that the flux bins for the two sets are different.

2.4 Discussion

2.4.1 Extragalactic Background Light

We plot the cumulative EBL as a function of flux at both wavelengths in Figure 2.6. Without gravitational lensing, our surveys would be limited to sources with $S_{450\mu\text{m}} \gtrsim 10$ mJy or $S_{850\mu\text{m}} > 2$ mJy. However, sources fainter than these limits contribute the majority of the EBL at both wavelengths. If we use the measurement by Fixsen et al. (1998) as the total EBL, $\sim 90\%$ of the 450 μm background comes from sources fainter than 10 mJy and $\sim 80\%$ of the 850 μm background comes from sources fainter than 2 mJy. These numbers would not change significantly even if we consider the effect of multiplicity. Our result also suggests there is at least $\sim 50\%$ of the EBL with $S_{450\mu\text{m}} < 1.0$ mJy. If we integrate the 450 μm differential count down to the lower flux limit in the upper panel of Figure 2.2, there is still at least $\sim 40\%$ of the EBL with $S_{450\mu\text{m}} < 0.7$ mJy that is not resolved by our SCUBA-2 maps. Most of these faint SMGs would have $L_{\text{IR}} < 10^{12}L_{\odot}$, corresponding to

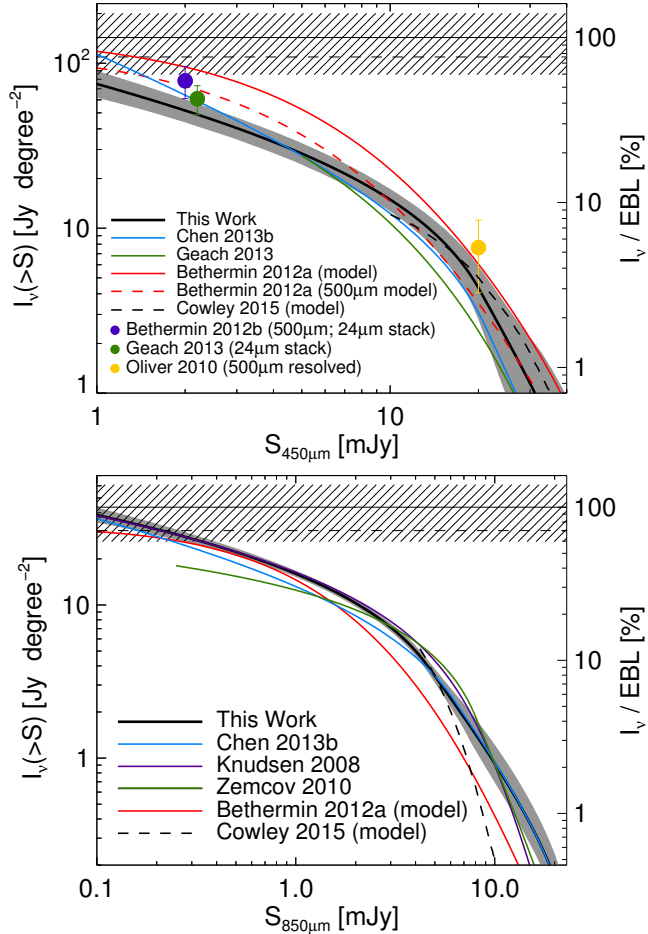


Figure 2.6: Cumulative EBL as a function of flux at $450 \mu m$ (upper) and $850 \mu m$ (lower). The thick solid black curves are calculated from our best-fit broken power law models (Table 3) with 1σ error regions in gray shading. The horizontal black dashed line (Puget et al. 1996) and the horizontal solid line with the hatched regions (Fixsen et al. 1998) are the EBL measured with the *COBE* satellite. The blue curves represent our previous results from Chen et al. (2013b). The predictions at $450/500 \mu m$ and $850 \mu m$ from Béthermin et al. (2012a) are shown as solid and dashed red curves. The black dashed curves are the predictions from Cowley et al. (2015). The green curve in the upper panel represents the result of the SCUBA-2 $450 \mu m$ map of the COSMOS field from Geach et al. (2013). The purple and green curves in the lower panel are the results based on SCUBA cluster surveys from Knudsen et al. (2008) and Zemcov et al. (2010), respectively. In the upper panel, some results of the $24 \mu m$ stacking on the $450 \mu m$ (Geach et al. 2013) and $500 \mu m$ (Béthermin et al. 2012b) maps and the directly resolved $500 \mu m$ background light (Oliver et al. 2010) are shown as colored circles.

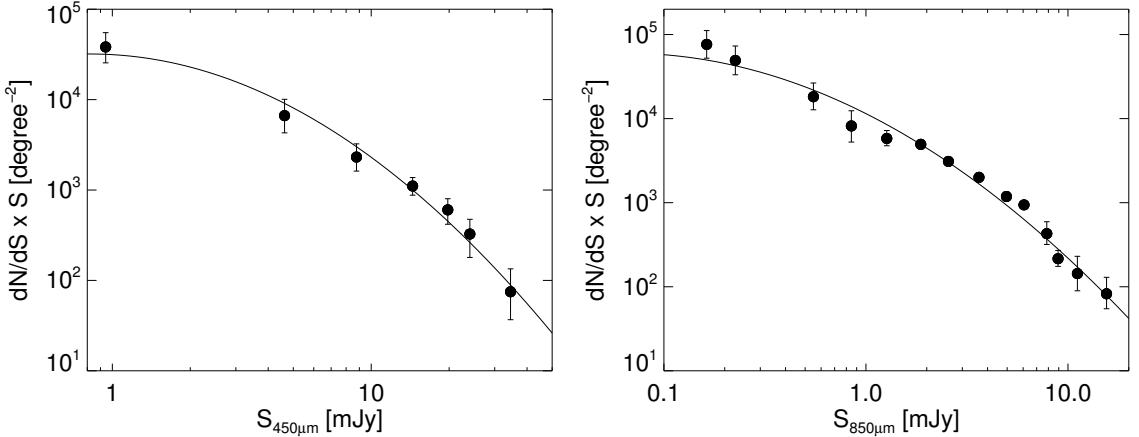


Figure 2.7: Combined differential number counts (from Figure 2.3) multiplied by the flux. Because the total EBL is essentially the integral of such curves, the curve for each wavelength must turn over at some point such that the derived cumulative EBL does not significantly exceed the total EBL measured by the *COBE* satellite. Solid black curves are second order polynomial fits to the log-log plots. The estimated turnovers are at $\sim 0.8 \text{ mJy}$ at $450 \mu\text{m}$ and $\sim 0.06 \text{ mJy}$ at $850 \mu\text{m}$ based on the polynomial fits.

LIRGs or normal galaxies. However, note that all these fractions of the EBL we calculate here depend on which measurement of the total EBL we assume, as well as its uncertainty.

We note that the faint-end slopes (α) of the number counts should become less than one at fluxes fainter than 1 mJy at $450 \mu\text{m}$ and 0.1 mJy at $850 \mu\text{m}$. In Figure 2.7, we show the combined differential number counts (from Figure 2.3) multiplied by the flux. Because the total EBL equals the integral of $dN/dS \times S$ over S , $dN/dS \times S$ must turn over at some point such that the derived cumulative EBL does not significantly exceed the total EBL measured by the *COBE* satellite. Using second order polynomial fits to the log-log plots in Figure 2.7, the estimated turnovers (where α becomes one) are at $\sim 0.8 \text{ mJy}$ at $450 \mu\text{m}$ and $\sim 0.06 \text{ mJy}$ at $850 \mu\text{m}$. Sources with these fluxes would contribute the most to the EBL. If we again assume a modified blackbody SED with $\beta = 1.5$ and a dust temperature of 40 K , $S_{450\mu\text{m}} \sim 0.8 \text{ mJy}$ and $S_{850\mu\text{m}} \sim 0.06 \text{ mJy}$ correspond to $L_{\text{IR}} \sim 1.3 \times 10^{11} L_\odot$ at $z = 2.2$ and $\sim 3.4 \times 10^{10} L_\odot$ at $z = 2.8$, respectively.

We also show other measurements and model predictions of the EBL from the literature in Figure 2.6. All of the observational results are consistent with ours within 1σ (note

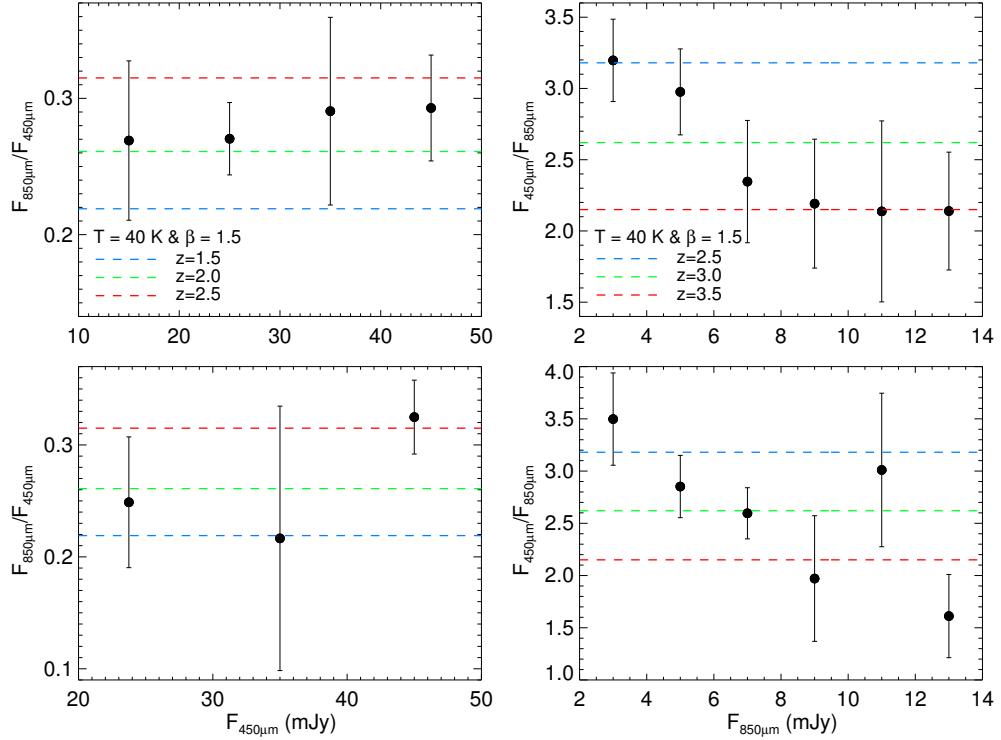


Figure 2.8: $850\mu\text{m}$ -to- $450\mu\text{m}$ flux ratio as a function of $450\mu\text{m}$ flux (left) and $450\mu\text{m}$ -to- $850\mu\text{m}$ flux ratio as a function of $850\mu\text{m}$ flux (right) for 4σ detected sources from the $450\mu\text{m}$ and $850\mu\text{m}$ maps, respectively, for our cluster fields (upper) and blank fields (lower). In each flux bin, we took the median of the flux ratios and calculated the error using bootstrapping. Unlike Figure 2.1, the data points are corrected for the effect of image noises on the flux ratio measurements, which is done by running simulations in which we populated sources with constant flux ratios. Some predicted flux ratios of a modified blackbody SED with $\beta = 1.5$ and a dust temperature of 40 K at several redshifts are shown as colored dashed lines for comparison.

that the 1σ spread of all the other cumulative EBL curves are not shown in Figure 2.6). There is, however, significant disagreement between the $450\text{ }\mu\text{m}$ model from Béthermin et al. (2012a) and our result. This difference is mainly caused by the discrepancy in the differential number counts at $S_{450\mu\text{m}} \sim 2\text{--}15\text{ mJy}$ (see Figure 2.3), where the model slightly overproduces sources.

Viero et al. (2013) quantified the fraction of the EBL that originates from galaxies identified in the UV/optical/near-infrared by stacking K -selected sources on various *Spitzer* and *Herschel* maps at different wavelengths. They were able to resolve $65\%\pm12\%$ of the EBL at $500\text{ }\mu\text{m}$ ($2.60\text{ nW m}^{-2}\text{ sr}^{-1}$ or 0.434 MJy sr^{-1}) based on the measurement by Lagache et al. (2000). If we correct their result using the EBL measured by Fixsen et al. (1998), their sample contributes $\sim 70\%$ of the EBL at $500\text{ }\mu\text{m}$ ($2.37\text{ nW m}^{-2}\text{ sr}^{-1}$ or 0.395 MJy sr^{-1}), which includes $\sim 10\%$, 40% , and 20% coming from normal galaxies, LIRGs, and ULIRGs, respectively. For comparison, we can assume an extreme case, where all of the $450\text{ }\mu\text{m}$ sources lie at $z = 2.8$ and have a modified blackbody SED with $\beta = 1.5$ and $T = 50\text{ K}$ (see Section 2.3.3). In such a case, galaxies with $L_{\text{IR}} < 10^{12}L_{\odot}$ would have $S_{450\mu\text{m}} \lesssim 3.4\text{ mJy}$, which still contribute $\sim 75\%$ of the EBL and cannot be fully accounted for by the normal galaxies and LIRGs in Viero et al. (2013). If we assume a lower dust temperature or a lower redshift, galaxies with $L_{\text{IR}} < 10^{12}L_{\odot}$ would contribute even more to the EBL. This is consistent with recent SMA (Chen et al. 2014) and ALMA (Kohno et al. 2016; Fujimoto et al. 2016) observations, which suggest that many faint SMGs may not be included in the UV star formation history.

Because the majority of sources that contribute the submillimeter EBL have $L_{\text{IR}} < 10^{12}L_{\odot}$, a full accounting of the cosmic star formation history requires a thorough understanding of the galaxies with FIR luminosities corresponding to LIRGs and normal star-forming galaxies. It is therefore critical to determine how much the submillimeter- and UV-selected samples overlap at this luminosity range. Future work using interferometry is needed to determine the fraction of faint SMGs that is already included in the UV population as a function of submillimeter flux.

2.4.2 Redshift Distributions

As described in Section 2.3.3, we used a statistical approach to explore the submillimeter flux ratios for both 450 μm and 850 μm selected samples from the cluster fields. If we do the same exercise on the blank-field data and again use a modified blackbody SED with $\beta = 1.5$, $T = 40$ K, the median redshifts of the 450 μm and 850 μm populations would be 2.0 and 2.6, respectively. These are in rough agreement with the median redshifts (2.06 ± 0.10 and 2.43 ± 0.12) from the simulations of Zavala et al. (2014). Béthermin et al. (2015) also presented the median redshift of dusty galaxies as a function of wavelength, flux limit, and lensing selection bias based on their empirical model (Béthermin et al. 2012a). The 4σ detection limits for our blank-field 450 μm , cluster 450 μm , blank-field 850 μm , and cluster 850 μm images are ~ 18 , 10, 2, and 2 mJy, respectively. According to Figure 3 of Béthermin et al. (2015), these flux cuts correspond to median redshifts of $z \sim 1.9$, $1.8 \lesssim z \lesssim 2.4$, $z \sim 2.4$ and $2.4 \lesssim z \lesssim 2.8$, respectively. These also roughly agree with our estimated median redshifts. Note that for our cluster fields, the corresponding redshifts are shown as intervals, because the relations in Figure 3 of Béthermin et al. (2015) are for all galaxies and “strongly lensed” galaxies, while our SCUBA-2 maps extend out to radii of $\sim 6'$ and therefore detect both strongly and weakly lensed sources.

In Figure 2.8, we show the 850 μm -to-450 μm and 450 μm -to-850 μm flux ratios versus the observed 450 μm and 850 μm fluxes, respectively, for both our cluster and blank-field data. The main difference between Figures 2.1 and 2.8 is that we correct the data points in Figure 2.8 for the effect of image noise on the flux ratio measurements. This is again done by running simulations in which we generated sources with constant flux ratios, and a detailed description is left to the Appendix. In Figure 2.8, we also show some predicted flux ratios of a modified blackbody SED with $\beta = 1.5$ and a dust temperature of 40 K at several redshifts. At 850 μm , a clear relation between the flux ratio and the observed flux can be seen in both the cluster and blank fields. This relation can be explained by a redshift evolution if the SEDs of these galaxies do not change significantly with redshift. Since the observed 850 μm flux of an SMG remains almost invariant over $z = 1\text{--}8$ due to the strong

negative K -correction, the variation of the flux ratio we see here might be a result of “cosmic downsizing” (Cowie et al. 1996), where SMGs at higher redshifts have higher gas fractions and therefore higher luminosities and star formation rates (e.g., Heavens et al. 2004; Bundy et al. 2006; Franceschini et al. 2006; Dye et al. 2008; Mobasher et al. 2009; Magliocchetti et al. 2011). Note that although the variation can be explained by an evolution in dust temperature, it would be interpreted as brighter sources having lower temperatures, which conflicts with many studies of dusty star-forming galaxies (e.g., Casey et al. 2012; U et al. 2012; Lee et al. 2013; Symeonidis et al. 2013).

Another possible factor that can cause the redshift variation we see here would be lensing bias, in which brighter sources contain a higher fraction of high-redshift, lensed galaxies. For the sources in our cluster fields, although their redshifts are needed to compute the precise lensing magnifications, the changes in their magnifications are much more sensitive to the source positions than to the redshifts. As a consequence, we can use the magnification maps for $z = 2.2$ and $z = 2.8$ that we generated using LENSTOOL (see Section 2.3.4) to quantify how strong the lensing effect is for each source. We do not see any correlation between the observed flux and the magnification for our lensed sources. This suggests that these brighter sources in the cluster fields are generally not more strongly lensed and are simply brighter intrinsically.

We also cannot rule out the possibility of galaxy–galaxy strong lensing events (which are not included in the cluster lens models) that cause lensing bias in both the blank and cluster fields. Theoretical predictions (e.g., Blain 1996; Perrotta et al. 2002, 2003; Negrello et al. 2007; Paciga et al. 2009; Béthermin et al. 2012a; Wardlow et al. 2013) showed that the fraction of strongly lensed sources increases with the observed submillimeter flux. Wide-area, flux-density limited surveys with *Herschel* have successfully discovered many bright, strongly lensed SMGs (e.g., Negrello et al. 2010; Conley et al. 2011; Wardlow et al. 2013). However, at the flux range of our SCUBA-2 sources, these galaxy–galaxy strong lensing events should be rare and should have little effect on the observed redshift distribution. If we take the count models from Béthermin et al. (2012a), 850 μm sources with fluxes of 3,

5, 7, 9, 11, and 13 mJy (corresponding to the flux bins in Figure 2.8) have lensing fractions of $\sim 1\%$, 2% , 3% , 5% , 7% , and 10% , respectively. Although a fraction of 10% might cause a significant effect, the lensing fractions in the four faintest $850 \mu\text{m}$ flux bins in Figure 2.8 are too small to produce the variation of redshift we see in both cluster and blank fields. Therefore, we conclude that lensing bias only has a minor effect on the observed redshift distribution and a downsizing scenario is the most likely cause.

On the other hand, we do not see a clear relation between the submillimeter flux ratio and the $450 \mu\text{m}$ flux, mainly because of the large uncertainties due to small number statistics. Deeper $450 \mu\text{m}$ maps obtained in the future should improve our measurements. However, a nearly flat distribution for the lensed sources shown in Figure 2.8 is in agreement with Roseboom et al. (2013). This result might still be consistent with a downsizing scenario, given that the observed $450 \mu\text{m}$ flux of an SMG does decrease with the redshift. The observed distribution of flux ratios might be flattened due to a mixture of high-redshift bright and low-redshift faint objects in the same flux bin. A similar trend is also seen in Figure 3 of Béthermin et al. (2015), where the median redshift of $450 \mu\text{m}$ sources between flux-density cuts of 10 and 50 mJy (the flux range shown in Figure 2.8) changes less than that of $850 \mu\text{m}$ sources between flux-density cuts of 2 and 14 mJy (the flux range shown in Figure 2.8) in both full samples and strongly lensed samples. Again, if we take the count models from Béthermin et al. (2012a), $450 \mu\text{m}$ sources with fluxes of 15, 25, 35, and 45 mJy (corresponding to the flux bins in Figure 2.8) have galaxy–galaxy lensing fractions of $\sim 1\%$, 2% , 4% , and 7% , respectively, which have little effect on the observed redshift distribution.

2.5 Summary

Using the SCUBA-2 camera mounted on the JCMT, we present deep number counts at 450 and $850 \mu\text{m}$. We combine data of six lensing cluster fields (A1689, A2390, A370, MACS J0717.5+3745, MACS J1149.5+2223, and MACS J1423.8+2404) and three blank fields (CDF-N, CDF-S, and COSMOS) to measure the counts over a wide flux range at

each wavelength. Thanks to gravitational lensing, we are able to detect counts at fluxes fainter than 1 mJy and 0.2 mJy in several fields at 450 μm and 850 μm , respectively. With the large number of cluster fields, our combined data highly constrain the faint end of the number counts. By integrating the number counts we measure, we found that the majority of EBL at each wavelength is contributed by sources that are fainter than the detection limit of our blank-field images. Most of these faint sources would have $L_{\text{IR}} < 10^{12} L_{\odot}$, corresponding to LIRGs or normal galaxies. By comparing our result with the 500 μm stacking of K -selected sources from Viero et al. (2013), we conclude that the K -selected LIRGs and normal galaxies still cannot fully account for the EBL that originates from sources with $L_{\text{IR}} < 10^{12} L_{\odot}$. This is consistent with recent SMA (Chen et al. 2014) and ALMA (Kohno et al. 2016) observations, which suggest that many faint SMGs may not be included in the UV star formation history. We also explore the submillimeter flux ratio between the two wavelengths for our 450 μm and 850 μm selected sources. At 850 μm , we find a clear relation between the flux ratio with the observed flux. This relation can be explained by a redshift evolution if the SEDs of these SMGs do not change significantly with redshift, where galaxies at higher redshifts have higher luminosities and star formation rates. On the other hand, we do not see a clear relation between the flux ratio and 450 μm flux.

References

- Aretxaga, I., Wilson, G. W., Aguilar, E., Alberts, S., Scott, K. S., Scoville, N., Yun, M. S., Austermann, J., Downes, T. P., Ezawa, H., Hatsukade, B., Hughes, D. H., Kawabe, R., Kohno, K., Oshima, T., Perera, T. A., Tamura, Y., & Zeballos, M. 2011, MNRAS, 415, 3831
- Austermann, J. E., Aretxaga, I., Hughes, D. H., Kang, Y., Kim, S., Lowenthal, J. D., Perera, T. A., Sanders, D. B., Scott, K. S., Scoville, N., Wilson, G. W., & Yun, M. S. 2009, MNRAS, 393, 1573
- Austermann, J. E., Dunlop, J. S., Perera, T. A., Scott, K. S., Wilson, G. W., Aretxaga, I., Hughes, D. H., Almaini, O., Chapin, E. L., Chapman, S. C., Cirasuolo, M., Clements, D. L., Coppin, K. E. K., Dunne, L., Dye, S., Eales, S. A., Egami, E., Farrah, D., Ferrusca, D., Flynn, S., Haig, D., Halpern, M., Ibar, E., Ivison, R. J., van Kampen, E., Kang, Y., Kim, S., Lace, C., Lowenthal, J. D., Mauskopf, P. D., McLure, R. J., Mortier, A. M. J., Negrello, M., Oliver, S., Peacock, J. A., Pope, A., Rawlings, S., Rieke, G., Roseboom, I., Rowan-Robinson, M., Scott, D., Serjeant, S., Smail, I., Swinbank, A. M., Stevens, J. A., Velazquez, M., Wagg, J., & Yun, M. S. 2010, MNRAS, 401, 160
- Barger, A. J., Cowie, L. L., Chen, C.-C., Owen, F. N., Wang, W.-H., Casey, C. M., Lee, N., Sanders, D. B., & Williams, J. P. 2014, ApJ, 784, 9
- Barger, A. J., Cowie, L. L., & Sanders, D. B. 1999, ApJ, 518, L5

Barger, A. J., Wang, W.-H., Cowie, L. L., Owen, F. N., Chen, C.-C., & Williams, J. P. 2012, ApJ, 761, 89

Berta, S., Magnelli, B., Nordon, R., Lutz, D., Wuyts, S., Altieri, B., Andreani, P., Aussel, H., Castañeda, H., Cepa, J., Cimatti, A., Daddi, E., Elbaz, D., Förster Schreiber, N. M., Genzel, R., Le Floc'h, E., Maiolino, R., Pérez-Fournon, I., Poglitsch, A., Popesso, P., Pozzi, F., Riguccini, L., Rodighiero, G., Sanchez-Portal, M., Sturm, E., Tacconi, L. J., & Valtchanov, I. 2011, A&A, 532, A49

Béthermin, M., Daddi, E., Magdis, G., Sargent, M. T., Hezaveh, Y., Elbaz, D., Le Borgne, D., Mullaney, J., Pannella, M., Buat, V., Charmandaris, V., Lagache, G., & Scott, D. 2012a, ApJ, 757, L23

Béthermin, M., De Breuck, C., Sargent, M., & Daddi, E. 2015, A&A, 576, L9

Béthermin, M., Dole, H., Lagache, G., Le Borgne, D., & Penin, A. 2011, A&A, 529, A4

Béthermin, M., Le Floc'h, E., Ilbert, O., Conley, A., Lagache, G., Amblard, A., Arumugam, V., Aussel, H., Berta, S., Bock, J., Boselli, A., Buat, V., Casey, C. M., Castro-Rodríguez, N., Cava, A., Clements, D. L., Cooray, A., Dowell, C. D., Eales, S., Farrah, D., Franceschini, A., Glenn, J., Griffin, M., Hatziminaoglou, E., Heinis, S., Ibar, E., Ivison, R. J., Kartaltepe, J. S., Levenson, L., Magdis, G., Marchetti, L., Marsden, G., Nguyen, H. T., O'Halloran, B., Oliver, S. J., Omont, A., Page, M. J., Panuzzo, P., Papageorgiou, A., Pearson, C. P., Pérez-Fournon, I., Pohlen, M., Rigopoulou, D., Roseboom, I. G., Rowan-Robinson, M., Salvato, M., Schulz, B., Scott, D., Seymour, N., Shupe, D. L., Smith, A. J., Symeonidis, M., Trichas, M., Tugwell, K. E., Vaccari, M., Valtchanov, I., Vieira, J. D., Viero, M., Wang, L., Xu, C. K., & Zemcov, M. 2012b, A&A, 542, A58

Blain, A. W. 1996, MNRAS, 283, 1340

Borys, C., Chapman, S., Halpern, M., & Scott, D. 2003, MNRAS, 344, 385

Bundy, K., Ellis, R. S., Conselice, C. J., Taylor, J. E., Cooper, M. C., Willmer, C. N. A., Weiner, B. J., Coil, A. L., Noeske, K. G., & Eisenhardt, P. R. M. 2006, *ApJ*, 651, 120

Bussmann, R. S., Riechers, D., Fialkov, A., Scudder, J., Hayward, C. C., Cowley, W. I., Bock, J., Calanog, J., Chapman, S. C., Cooray, A., De Bernardis, F., Farrah, D., Fu, H., Gavazzi, R., Hopwood, R., Ivison, R. J., Jarvis, M., Lacey, C., Loeb, A., Oliver, S. J., Pérez-Fournon, I., Rigopoulou, D., Roseboom, I. G., Scott, D., Smith, A. J., Vieira, J. D., Wang, L., & Wardlow, J. 2015, *ApJ*, 812, 43

Carniani, S., Maiolino, R., De Zotti, G., Negrello, M., Marconi, A., Bothwell, M. S., Capak, P., Carilli, C., Castellano, M., Cristiani, S., Ferrara, A., Fontana, A., Gallerani, S., Jones, G., Ohta, K., Ota, K., Pentericci, L., Santini, P., Sheth, K., Vallini, L., Vanzella, E., Wagg, J., & Williams, R. J. 2015, ArXiv e-prints

Casey, C. M., Berta, S., Béthermin, M., Bock, J., Bridge, C., Burgarella, D., Chapin, E., Chapman, S. C., Clements, D. L., Conley, A., Conselice, C. J., Cooray, A., Farrah, D., Hatziminaoglou, E., Ivison, R. J., le Floc'h, E., Lutz, D., Magdis, G., Magnelli, B., Oliver, S. J., Page, M. J., Pozzi, F., Rigopoulou, D., Riguccini, L., Roseboom, I. G., Sanders, D. B., Scott, D., Seymour, N., Valtchanov, I., Vieira, J. D., Viero, M., & Wardlow, J. 2012, *ApJ*, 761, 139

Casey, C. M., Chen, C.-C., Cowie, L., Barger, A., Capak, P., Ilbert, O., Koss, M., Lee, N., Le Floc'h, E., Sanders, D. B., & Williams, J. P. 2013, *MNRAS*, 436, 1919

Chapin, E. L., Berry, D. S., Gibb, A. G., Jenness, T., Scott, D., Tilanus, R. P. J., Economou, F., & Holland, W. S. 2013, *MNRAS*, 430, 2545

Chen, C.-C., Cowie, L. L., Barger, A. J., Casey, C. M., Lee, N., Sanders, D. B., Wang, W.-H., & Williams, J. P. 2013a, *ApJ*, 762, 81

—. 2013b, *ApJ*, 776, 131

Chen, C.-C., Cowie, L. L., Barger, A. J., Wang, W.-H., & Williams, J. P. 2014, ApJ, 789, 12

Chen, C.-C., Cowie, L. L., Wang, W.-H., Barger, A. J., & Williams, J. P. 2011, ApJ, 733, 64

Condon, J. J. 1974, ApJ, 188, 279

Conley, A., Cooray, A., Vieira, J. D., González Solares, E. A., Kim, S., Aguirre, J. E., Amblard, A., Auld, R., Baker, A. J., Beelen, A., Blain, A., Blundell, R., Bock, J., Bradford, C. M., Bridge, C., Brisbin, D., Burgarella, D., Carpenter, J. M., Chanial, P., Chapin, E., Christopher, N., Clements, D. L., Cox, P., Djorgovski, S. G., Dowell, C. D., Eales, S., Earle, L., Ellsworth-Bowers, T. P., Farrah, D., Franceschini, A., Frayer, D., Fu, H., Gavazzi, R., Glenn, J., Griffin, M., Gurwell, M. A., Halpern, M., Ibar, E., Ivison, R. J., Jarvis, M., Kamenetzky, J., Krips, M., Levenson, L., Lupu, R., Mahabal, A., Maloney, P. D., Maraston, C., Marchetti, L., Marsden, G., Matsuhara, H., Mortier, A. M. J., Murphy, E., Naylor, B. J., Neri, R., Nguyen, H. T., Oliver, S. J., Omont, A., Page, M. J., Papageorgiou, A., Pearson, C. P., Pérez-Fournon, I., Pohlen, M., Rangwala, N., Rawlings, J. I., Raymond, G., Riechers, D., Rodighiero, G., Roseboom, I. G., Rowan-Robinson, M., Schulz, B., Scott, D., Scott, K., Serra, P., Seymour, N., Shupe, D. L., Smith, A. J., Symeonidis, M., Tugwell, K. E., Vaccari, M., Valiante, E., Valtchanov, I., Verma, A., Viero, M. P., Vigroux, L., Wang, L., Wiebe, D., Wright, G., Xu, C. K., Zeimann, G., Zemcov, M., & Zmuidzinas, J. 2011, ApJ, 732, L35

Coppin, K., Chapin, E. L., Mortier, A. M. J., Scott, S. E., Borys, C., Dunlop, J. S., Halpern, M., Hughes, D. H., Pope, A., Scott, D., Serjeant, S., Wagg, J., Alexander, D. M., Almaini, O., Artxaga, I., Babbedge, T., Best, P. N., Blain, A., Chapman, S., Clements, D. L., Crawford, M., Dunne, L., Eales, S. A., Edge, A. C., Farrah, D., Gaztañaga, E., Gear, W. K., Granato, G. L., Greve, T. R., Fox, M., Ivison, R. J., Jarvis, M. J., Jenness, T., Lacey, C., Lepage, K., Mann, R. G., Marsden, G., Martinez-Sansigre, A., Oliver, S., Page, M. J., Peacock, J. A., Pearson, C. P., Percival, W. J., Priddey, R. S., Rawlings,

- S., Rowan-Robinson, M., Savage, R. S., Seigar, M., Sekiguchi, K., Silva, L., Simpson, C., Smail, I., Stevens, J. A., Takagi, T., Vaccari, M., van Kampen, E., & Willott, C. J. 2006, MNRAS, 372, 1621
- Cowie, L. L., Barger, A. J., & Kneib, J.-P. 2002, AJ, 123, 2197
- Cowie, L. L., Songaila, A., Hu, E. M., & Cohen, J. G. 1996, AJ, 112, 839
- Cowley, W. I., Lacey, C. G., Baugh, C. M., & Cole, S. 2015, MNRAS, 446, 1784
- Dempsey, J. T., Friberg, P., Jenness, T., Tilanus, R. P. J., Thomas, H. S., Holland, W. S., Bintley, D., Berry, D. S., Chapin, E. L., Chrysostomou, A., Davis, G. R., Gibb, A. G., Parsons, H., & Robson, E. I. 2013, MNRAS, 430, 2534
- Dye, S., Eales, S. A., Arétxaga, I., Serjeant, S., Dunlop, J. S., Babbedge, T. S. R., Chapman, S. C., Cirasuolo, M., Clements, D. L., Coppin, K. E. K., Dunne, L., Egami, E., Farrah, D., Ivison, R. J., van Kampen, E., Pope, A., Priddey, R., Rieke, G. H., Schael, A. M., Scott, D., Simpson, C., Takagi, T., Takata, T., & Vaccari, M. 2008, MNRAS, 386, 1107
- Eales, S., Lilly, S., Gear, W., Dunne, L., Bond, J. R., Hammer, F., Le Fèvre, O., & Crampton, D. 1999, ApJ, 515, 518
- Eales, S., Lilly, S., Webb, T., Dunne, L., Gear, W., Clements, D., & Yun, M. 2000, AJ, 120, 2244
- Eddington, A. S. 1913, MNRAS, 73, 359
- Ezawa, H., Kawabe, R., Kohno, K., & Yamamoto, S. 2004, in Society of Photo-Optical Instrumentation Engineers (SPIE) Conference Series, Vol. 5489, Ground-based Telescopes, ed. J. M. Oschmann, Jr., 763–772
- Fixsen, D. J., Dwek, E., Mather, J. C., Bennett, C. L., & Shafer, R. A. 1998, ApJ, 508, 123
- Franceschini, A., Rodighiero, G., Cassata, P., Berta, S., Vaccari, M., Nonino, M., Vanzella, E., Hatziminaoglou, E., Antichi, J., & Cristiani, S. 2006, A&A, 453, 397

Fujimoto, S., Ouchi, M., Ono, Y., Shibuya, T., Ishigaki, M., Nagai, H., & Momose, R. 2016, ApJS, 222, 1

Geach, J. E., Chapin, E. L., Coppin, K. E. K., Dunlop, J. S., Halpern, M., Smail, I., van der Werf, P., Serjeant, S., Farrah, D., Roseboom, I., Targett, T., Arumugam, V., Asboth, V., Blain, A., Chrysostomou, A., Clarke, C., Ivison, R. J., Jones, S. L., Karim, A., Mackenzie, T., Meijerink, R., Michałowski, M. J., Scott, D., Simpson, J. M., Swinbank, A. M., Alexander, D. M., Almaini, O., Aretxaga, I., Best, P., Chapman, S., Clements, D. L., Conselice, C., Danielson, A. L. R., Eales, S., Edge, A. C., Gibb, A. G., Hughes, D., Jenness, T., Knudsen, K. K., Lacey, C. G., Marsden, G., McMahon, R., Oliver, S. J., Page, M. J., Peacock, J. A., Rigopoulou, D., Robson, E. I., Spaans, M., Stevens, J., Webb, T. M. A., Willott, C., Wilson, C. D., & Zemcov, M. 2013, MNRAS, 432, 53

Gehrels, N. 1986, ApJ, 303, 336

Güsten, R., Nyman, L. Å., Schilke, P., Menten, K., Cesarsky, C., & Booth, R. 2006, A&A, 454, L13

Hatsukade, B., Kohno, K., Aretxaga, I., Austermann, J. E., Ezawa, H., Hughes, D. H., Ikarashi, S., Iono, D., Kawabe, R., Khan, S., Matsuo, H., Matsuura, S., Nakanishi, K., Oshima, T., Perera, T., Scott, K. S., Shirahata, M., Takeuchi, T. T., Tamura, Y., Tanaka, K., Tosaki, T., Wilson, G. W., & Yun, M. S. 2011, MNRAS, 411, 102

Hatsukade, B., Kohno, K., Umehata, H., Aretxaga, I., Caputi, K. I., Dunlop, J. S., Ikarashi, S., Iono, D., Ivison, R. J., Lee, M., Makiya, R., Matsuda, Y., Motohara, K., Nakanishi, K., Ohta, K., Tadaki, K.-i., Tamura, Y., Wang, W.-H., Wilson, G. W., Yamaguchi, Y., & Yun, M. S. 2016, PASJ, 68, 36

Hatsukade, B., Ohta, K., Seko, A., Yabe, K., & Akiyama, M. 2013, ApJ, 769, L27

Hayward, C. C., Behroozi, P. S., Somerville, R. S., Primack, J. R., Moreno, J., & Wechsler, R. H. 2013a, MNRAS, 434, 2572

- Hayward, C. C., Narayanan, D., Kereš, D., Jonsson, P., Hopkins, P. F., Cox, T. J., & Hernquist, L. 2013b, MNRAS, 428, 2529
- Heavens, A., Panter, B., Jimenez, R., & Dunlop, J. 2004, Nature, 428, 625
- Hezaveh, Y. D. & Holder, G. P. 2011, ApJ, 734, 52
- Hodge, J. A., Karim, A., Smail, I., Swinbank, A. M., Walter, F., Biggs, A. D., Ivison, R. J., Weiss, A., Alexander, D. M., Bertoldi, F., Brandt, W. N., Chapman, S. C., Coppin, K. E. K., Cox, P., Danielson, A. L. R., Dannerbauer, H., De Breuck, C., Decarli, R., Edge, A. C., Greve, T. R., Knudsen, K. K., Menten, K. M., Rix, H.-W., Schinnerer, E., Simpson, J. M., Wardlow, J. L., & van der Werf, P. 2013, ApJ, 768, 91
- Holland, W. S., Bintley, D., Chapin, E. L., Chrysostomou, A., Davis, G. R., Dempsey, J. T., Duncan, W. D., Fich, M., Friberg, P., Halpern, M., Irwin, K. D., Jenness, T., Kelly, B. D., MacIntosh, M. J., Robson, E. I., Scott, D., Ade, P. A. R., Atad-Ettedgui, E., Berry, D. S., Craig, S. C., Gao, X., Gibb, A. G., Hilton, G. C., Hollister, M. I., Kycia, J. B., Lunney, D. W., McGregor, H., Montgomery, D., Parkes, W., Tilanus, R. P. J., Ullom, J. N., Walther, C. A., Walton, A. J., Woodcraft, A. L., Amiri, M., Atkinson, D., Burger, B., Chuter, T., Coulson, I. M., Doriese, W. B., Dunare, C., Economou, F., Niemack, M. D., Parsons, H. A. L., Reintsema, C. D., Sibthorpe, B., Smail, I., Sudiwala, R., & Thomas, H. S. 2013, MNRAS, 430, 2513
- Hsu, L.-Y., Cowie, L. L., Chen, C.-C., Barger, A. J., & Wang, W.-H. 2016, ApJ, 829, 25
- Hughes, D. H., Serjeant, S., Dunlop, J., Rowan-Robinson, M., Blain, A., Mann, R. G., Ivison, R., Peacock, J., Efstathiou, A., Gear, W., Oliver, S., Lawrence, A., Longair, M., Goldschmidt, P., & Jenness, T. 1998, Nature, 394, 241
- Johansson, D., Sigurdarson, H., & Horellou, C. 2011, A&A, 527, A117
- Karim, A., Swinbank, A. M., Hodge, J. A., Smail, I. R., Walter, F., Biggs, A. D., Simpson, J. M., Danielson, A. L. R., Alexander, D. M., Bertoldi, F., de Breuck, C., Chapman,

- S. C., Coppin, K. E. K., Dannerbauer, H., Edge, A. C., Greve, T. R., Ivison, R. J., Knudsen, K. K., Menten, K. M., Schinnerer, E., Wardlow, J. L., Weiß, A., & van der Werf, P. 2013, MNRAS, 432, 2
- Kneib, J.-P., Ellis, R. S., Smail, I., Couch, W. J., & Sharples, R. M. 1996, ApJ, 471, 643
- Knudsen, K. K., van der Werf, P. P., & Kneib, J.-P. 2008, MNRAS, 384, 1611
- Kohno, K., Yamaguchi, Y., Tamura, Y., Tadaki, K., Hatsukade, B., Ikarashi, S., Caputi, K. I., Rujopakarn, W., Ivison, R. J., Dunlop, J. S., Motohara, K., Umehata, H., Yabe, K., Wang, W.-H., Kodama, T., Koyama, Y., Hayashi, M., Matsuda, Y., Hughes, D., Artxaga, I., Wilson, G. W., Yun, M. S., Ohta, K., Akiyama, M., Kawabe, R., Iono, D., Nakanishi, K., Lee, M., & Makiya, R. 2016, ArXiv e-prints
- Lacey, C. G., Baugh, C. M., Frenk, C. S., Benson, A. J., Bower, R. G., Cole, S., Gonzalez-Perez, V., Helly, J. C., Lagos, C. D. P., & Mitchell, P. D. 2015, ArXiv e-prints
- Lagache, G., Haffner, L. M., Reynolds, R. J., & Tufte, S. L. 2000, A&A, 354, 247
- Larson, D., Dunkley, J., Hinshaw, G., Komatsu, E., Nolta, M. R., Bennett, C. L., Gold, B., Halpern, M., Hill, R. S., Jarosik, N., Kogut, A., Limon, M., Meyer, S. S., Odegard, N., Page, L., Smith, K. M., Spergel, D. N., Tucker, G. S., Weiland, J. L., Wollack, E., & Wright, E. L. 2011, ApJS, 192, 16
- Lee, N., Sanders, D. B., Casey, C. M., Scoville, N. Z., Hung, C.-L., Le Floc'h, E., Ilbert, O., Aussel, H., Capak, P., Kartaltepe, J. S., Roseboom, I., Salvato, M., Aravena, M., Berta, S., Bock, J., Oliver, S. J., Riguccini, L., & Symeonidis, M. 2013, ApJ, 778, 131
- Limousin, M., Ebeling, H., Ma, C.-J., Swinbank, A. M., Smith, G. P., Richard, J., Edge, A. C., Jauzac, M., Kneib, J.-P., Marshall, P., & Schrabbback, T. 2010, MNRAS, 405, 777
- Limousin, M., Richard, J., Jullo, E., Kneib, J.-P., Fort, B., Soucail, G., Elíasdóttir, Á., Natarajan, P., Ellis, R. S., Smail, I., Czoske, O., Smith, G. P., Hudelot, P., Bardeau, S., Ebeling, H., Egami, E., & Knudsen, K. K. 2007, ApJ, 668, 643

Magliocchetti, M., Santini, P., Rodighiero, G., Grazian, A., Aussel, H., Altieri, B., Andreani, P., Berta, S., Cepa, J., Castañeda, H., Cimatti, A., Daddi, E., Elbaz, D., Genzel, R., Gruppioni, C., Lutz, D., Magnelli, B., Maiolino, R., Popesso, P., Poglitsch, A., Pozzi, F., Sanchez-Portal, M., Förster Schreiber, N. M., Sturm, E., Tacconi, L., & Valtchanov, I. 2011, MNRAS, 416, 1105

Mobasher, B., Dahlen, T., Hopkins, A., Scoville, N. Z., Capak, P., Rich, R. M., Sanders, D. B., Schinnerer, E., Ilbert, O., Salvato, M., & Sheth, K. 2009, ApJ, 690, 1074

Negrello, M., Hopwood, R., De Zotti, G., Cooray, A., Verma, A., Bock, J., Frayer, D. T., Gurwell, M. A., Omont, A., Neri, R., Dannerbauer, H., Leeuw, L. L., Barton, E., Cooke, J., Kim, S., da Cunha, E., Rodighiero, G., Cox, P., Bonfield, D. G., Jarvis, M. J., Serjeant, S., Ivison, R. J., Dye, S., Artxaga, I., Hughes, D. H., Ibar, E., Bertoldi, F., Valtchanov, I., Eales, S., Dunne, L., Driver, S. P., Auld, R., Buttiglione, S., Cava, A., Grady, C. A., Clements, D. L., Dariush, A., Fritz, J., Hill, D., Hornbeck, J. B., Kelvin, L., Lagache, G., Lopez-Caniego, M., Gonzalez-Nuevo, J., Maddox, S., Pascale, E., Pohlen, M., Rigby, E. E., Robotham, A., Simpson, C., Smith, D. J. B., Temi, P., Thompson, M. A., Woodgate, B. E., York, D. G., Aguirre, J. E., Beelen, A., Blain, A., Baker, A. J., Birkinshaw, M., Blundell, R., Bradford, C. M., Burgarella, D., Danese, L., Dunlop, J. S., Fleuren, S., Glenn, J., Harris, A. I., Kamenetzky, J., Lupu, R. E., Maddalena, R. J., Madore, B. F., Maloney, P. R., Matsuhara, H., Michałowski, M. J., Murphy, E. J., Naylor, B. J., Nguyen, H., Popescu, C., Rawlings, S., Rigopoulou, D., Scott, D., Scott, K. S., Seibert, M., Smail, I., Tuffs, R. J., Vieira, J. D., van der Werf, P. P., & Zmuidzinas, J. 2010, Science, 330, 800

Negrello, M., Perrotta, F., González-Nuevo, J., Silva, L., de Zotti, G., Granato, G. L., Baccigalupi, C., & Danese, L. 2007, MNRAS, 377, 1557

Oliver, S. J., Wang, L., Smith, A. J., Altieri, B., Amblard, A., Arumugam, V., Auld, R., Aussel, H., Babbedge, T., Blain, A., Bock, J., Boselli, A., Buat, V., Burgarella, D., Castro-Rodríguez, N., Cava, A., Chantal, P., Clements, D. L., Conley, A., Conversi, L.,

Cooray, A., Dowell, C. D., Dwek, E., Eales, S., Elbaz, D., Fox, M., Franceschini, A., Gear, W., Glenn, J., Griffin, M., Halpern, M., Hatziminaoglou, E., Ibar, E., Isaak, K., Ivison, R. J., Lagache, G., Levenson, L., Lu, N., Madden, S., Maffei, B., Mainetti, G., Marchetti, L., Mitchell-Wynne, K., Mortier, A. M. J., Nguyen, H. T., O'Halloran, B., Omont, A., Page, M. J., Panuzzo, P., Papageorgiou, A., Pearson, C. P., Pérez-Fournon, I., Pohlen, M., Rawlings, J. I., Raymond, G., Rigopoulou, D., Rizzo, D., Roseboom, I. G., Rowan-Robinson, M., Sánchez Portal, M., Savage, R., Schulz, B., Scott, D., Seymour, N., Shupe, D. L., Stevens, J. A., Symeonidis, M., Trichas, M., Tugwell, K. E., Vaccari, M., Valiante, E., Valtchanov, I., Vieira, J. D., Vigroux, L., Ward, R., Wright, G., Xu, C. K., & Zemcov, M. 2010, *A&A*, 518, L21

Ono, Y., Ouchi, M., Kurono, Y., & Momose, R. 2014, *ApJ*, 795, 5

Oteo, I., Zwaan, M. A., Ivison, R. J., Smail, I., & Biggs, A. D. 2016, *ApJ*, 822, 36

Paciga, G., Scott, D., & Chapin, E. L. 2009, *MNRAS*, 395, 1153

Perera, T. A., Chapin, E. L., Austermann, J. E., Scott, K. S., Wilson, G. W., Halpern, M., Pope, A., Scott, D., Yun, M. S., Lowenthal, J. D., Morrison, G., Artxaga, I., Bock, J. J., Coppin, K., Crowe, M., Frey, L., Hughes, D. H., Kang, Y., Kim, S., & Mauskopf, P. D. 2008, *MNRAS*, 391, 1227

Perrotta, F., Baccigalupi, C., Bartelmann, M., De Zotti, G., & Granato, G. L. 2002, *MNRAS*, 329, 445

Perrotta, F., Magliocchetti, M., Baccigalupi, C., Bartelmann, M., De Zotti, G., Granato, G. L., Silva, L., & Danese, L. 2003, *MNRAS*, 338, 623

Puget, J.-L., Abergel, A., Bernard, J.-P., Boulanger, F., Burton, W. B., Desert, F.-X., & Hartmann, D. 1996, *A&A*, 308, L5

Richard, J., Smith, G. P., Kneib, J.-P., Ellis, R. S., Sanderson, A. J. R., Pei, L., Targett, T. A., Sand, D. J., Swinbank, A. M., Dannerbauer, H., Mazzotta, P., Limousin, M., Egami, E., Jullo, E., Hamilton-Morris, V., & Moran, S. M. 2010, MNRAS, 404, 325

Roseboom, I. G., Dunlop, J. S., Cirasuolo, M., Geach, J. E., Smail, I., Halpern, M., van der Werf, P., Almaini, O., Arumugam, V., Asboth, V., Auld, R., Blain, A., Bremer, M. N., Bock, J., Bowler, R. A. A., Buitrago, F., Chapin, E., Chapman, S., Chrysostomou, A., Clarke, C., Conley, A., Coppin, K. E. K., Danielson, A. L. R., Farrah, D., Glenn, J., Hatziminaoglou, E., Ibar, E., Ivison, R. J., Jenness, T., van Kampen, E., Karim, A., Mackenzie, T., Marsden, G., Meijerink, R., Michałowski, M. J., Oliver, S. J., Page, M. J., Pearson, E., Scott, D., Simpson, J. M., Smith, D. J. B., Spaans, M., Swinbank, A. M., Symeonidis, M., Targett, T., Valiante, E., Viero, M., Wang, L., Willott, C. J., & Zemcov, M. 2013, MNRAS, 436, 430

Scott, K. S., Wilson, G. W., Aretxaga, I., Austermann, J. E., Chapin, E. L., Dunlop, J. S., Ezawa, H., Halpern, M., Hatsukade, B., Hughes, D. H., Kawabe, R., Kim, S., Kohno, K., Lowenthal, J. D., Montaña, A., Nakanishi, K., Oshima, T., Sanders, D., Scott, D., Scoville, N., Tamura, Y., Welch, D., Yun, M. S., & Zeballos, M. 2012, MNRAS, 423, 575

Scott, K. S., Yun, M. S., Wilson, G. W., Austermann, J. E., Aguilar, E., Aretxaga, I., Ezawa, H., Ferrusca, D., Hatsukade, B., Hughes, D. H., Iono, D., Giavalisco, M., Kawabe, R., Kohno, K., Mauskopf, P. D., Oshima, T., Perera, T. A., Rand, J., Tamura, Y., Tosaki, T., Velazquez, M., Williams, C. C., & Zeballos, M. 2010, MNRAS, 405, 2260

Scott, S. E., Fox, M. J., Dunlop, J. S., Serjeant, S., Peacock, J. A., Ivison, R. J., Oliver, S., Mann, R. G., Lawrence, A., Efstathiou, A., Rowan-Robinson, M., Hughes, D. H., Archibald, E. N., Blain, A., & Longair, M. 2002, MNRAS, 331, 817

Serjeant, S., Dunlop, J. S., Mann, R. G., Rowan-Robinson, M., Hughes, D., Efstathiou, A., Blain, A., Fox, M., Ivison, R. J., Jenness, T., Lawrence, A., Longair, M., Oliver, S., & Peacock, J. A. 2003, MNRAS, 344, 887

- Simpson, J. M., Smail, I., Swinbank, A. M., Chapman, S. C., Geach, J. E., Ivison, R. J., Thomson, A. P., Artxaga, I., Blain, A. W., Cowley, W. I., Chen, C.-C., Coppin, K. E. K., Dunlop, J. S., Edge, A. C., Farrah, D., Ibar, E., Karim, A., Knudsen, K. K., Meijerink, R., Michałowski, M. J., Scott, D., Spaans, M., & van der Werf, P. P. 2015, *ApJ*, 807, 128
- Siringo, G., Kreysa, E., Kovács, A., Schuller, F., Weiß, A., Esch, W., Gemünd, H.-P., Jethava, N., Lundershausen, G., Colin, A., Güsten, R., Menten, K. M., Beelen, A., Bertoldi, F., Beeman, J. W., & Haller, E. E. 2009, *A&A*, 497, 945
- Smail, I., Ivison, R. J., & Blain, A. W. 1997, *ApJ*, 490, L5
- Smail, I., Ivison, R. J., Blain, A. W., & Kneib, J.-P. 2002, *MNRAS*, 331, 495
- Smolčić, V., Aravena, M., Navarrete, F., Schinnerer, E., Riechers, D. A., Bertoldi, F., Feruglio, C., Finoguenov, A., Salvato, M., Sargent, M., McCracken, H. J., Albrecht, M., Karim, A., Capak, P., Carilli, C. L., Cappelluti, N., Elvis, M., Ilbert, O., Kartaltepe, J., Lilly, S., Sanders, D., Sheth, K., Scoville, N. Z., & Taniguchi, Y. 2012, *A&A*, 548, A4
- Symeonidis, M., Vaccari, M., Berta, S., Page, M. J., Lutz, D., Arumugam, V., Aussel, H., Bock, J., Boselli, A., Buat, V., Capak, P. L., Clements, D. L., Conley, A., Conversi, L., Cooray, A., Dowell, C. D., Farrah, D., Franceschini, A., Giovannoli, E., Glenn, J., Griffin, M., Hatziminaoglou, E., Hwang, H.-S., Ibar, E., Ilbert, O., Ivison, R. J., Floc'h, E. L., Lilly, S., Kartaltepe, J. S., Magnelli, B., Magdis, G., Marchetti, L., Nguyen, H. T., Nordon, R., O'Halloran, B., Oliver, S. J., Omont, A., Papageorgiou, A., Patel, H., Pearson, C. P., Pérez-Fournon, I., Pohlen, M., Popesso, P., Pozzi, F., Rigopoulou, D., Riguccini, L., Rosario, D., Roseboom, I. G., Rowan-Robinson, M., Salvato, M., Schulz, B., Scott, D., Seymour, N., Shupe, D. L., Smith, A. J., Valtchanov, I., Wang, L., Xu, C. K., Zemcov, M., & Wuyts, S. 2013, *MNRAS*, 431, 2317
- U, V., Sanders, D. B., Mazzarella, J. M., Evans, A. S., Howell, J. H., Surace, J. A., Armus, L., Iwasawa, K., Kim, D.-C., Casey, C. M., Vavilkin, T., Dufault, M., Larson,

- K. L., Barnes, J. E., Chan, B. H. P., Frayer, D. T., Haan, S., Inami, H., Ishida, C. M., Kartaltepe, J. S., Melbourne, J. L., & Petric, A. O. 2012, ApJS, 203, 9
- Valiante, E., Lutz, D., Sturm, E., Genzel, R., & Chapin, E. L. 2009, ApJ, 701, 1814
- Viero, M. P., Moncelsi, L., Quadri, R. F., Arumugam, V., Assef, R. J., Béthermin, M., Bock, J., Bridge, C., Casey, C. M., Conley, A., Cooray, A., Farrah, D., Glenn, J., Heinis, S., Ibar, E., Ikarashi, S., Ivison, R. J., Kohno, K., Marsden, G., Oliver, S. J., Roseboom, I. G., Schulz, B., Scott, D., Serra, P., Vaccari, M., Vieira, J. D., Wang, L., Wardlow, J., Wilson, G. W., Yun, M. S., & Zemcov, M. 2013, ApJ, 779, 32
- Wang, W.-H., Cowie, L. L., & Barger, A. J. 2004, ApJ, 613, 655
- Wang, W.-H., Cowie, L. L., Barger, A. J., & Williams, J. P. 2011, ApJ, 726, L18
- Wardlow, J. L., Cooray, A., De Bernardis, F., Amblard, A., Arumugam, V., Aussel, H., Baker, A. J., Béthermin, M., Blundell, R., Bock, J., Boselli, A., Bridge, C., Buat, V., Burgarella, D., Bussmann, R. S., Cabrera-Lavers, A., Calanog, J., Carpenter, J. M., Casey, C. M., Castro-Rodríguez, N., Cava, A., Chanial, P., Chapin, E., Chapman, S. C., Clements, D. L., Conley, A., Cox, P., Dowell, C. D., Dye, S., Eales, S., Farrah, D., Ferrero, P., Franceschini, A., Frayer, D. T., Frazer, C., Fu, H., Gavazzi, R., Glenn, J., González Solares, E. A., Griffin, M., Gurwell, M. A., Harris, A. I., Hatziminaoglou, E., Hopwood, R., Hyde, A., Ibar, E., Ivison, R. J., Kim, S., Lagache, G., Levenson, L., Marchetti, L., Marsden, G., Martinez-Navajas, P., Negrello, M., Neri, R., Nguyen, H. T., O'Halloran, B., Oliver, S. J., Omont, A., Page, M. J., Panuzzo, P., Papageorgiou, A., Pearson, C. P., Pérez-Fournon, I., Pohlen, M., Riechers, D., Rigopoulou, D., Roseboom, I. G., Rowan-Robinson, M., Schulz, B., Scott, D., Scoville, N., Seymour, N., Shupe, D. L., Smith, A. J., Streblyanska, A., Strom, A., Symeonidis, M., Trichas, M., Vaccari, M., Vieira, J. D., Viero, M., Wang, L., Xu, C. K., Yan, L., & Zemcov, M. 2013, ApJ, 762, 59
- Webb, T. M., Eales, S. A., Lilly, S. J., Clements, D. L., Dunne, L., Gear, W. K., Ivison, R. J., Flores, H., & Yun, M. 2003, ApJ, 587, 41

Weiβ, A., De Breuck, C., Marrone, D. P., Vieira, J. D., Aguirre, J. E., Aird, K. A., Aravena, M., Ashby, M. L. N., Bayliss, M., Benson, B. A., Béthermin, M., Biggs, A. D., Bleem, L. E., Bock, J. J., Bothwell, M., Bradford, C. M., Brodwin, M., Carlstrom, J. E., Chang, C. L., Chapman, S. C., Crawford, T. M., Crites, A. T., de Haan, T., Dobbs, M. A., Downes, T. P., Fassnacht, C. D., George, E. M., Gladders, M. D., Gonzalez, A. H., Greve, T. R., Halverson, N. W., Hezaveh, Y. D., High, F. W., Holder, G. P., Holzapfel, W. L., Hoover, S., Hrubes, J. D., Husband, K., Keisler, R., Lee, A. T., Leitch, E. M., Lueker, M., Luong-Van, D., Malkan, M., McIntyre, V., McMahon, J. J., Mehl, J., Menten, K. M., Meyer, S. S., Murphy, E. J., Padin, S., Plagge, T., Reichardt, C. L., Rest, A., Rosenman, M., Ruel, J., Ruhl, J. E., Schaffer, K. K., Shirokoff, E., Spilker, J. S., Stalder, B., Staniszewski, Z., Stark, A. A., Story, K., Vanderlinde, K., Welikala, N., & Williamson, R. 2013, ApJ, 767, 88

Weiβ, A., Kovács, A., Coppin, K., Greve, T. R., Walter, F., Smail, I., Dunlop, J. S., Knudsen, K. K., Alexander, D. M., Bertoldi, F., Brandt, W. N., Chapman, S. C., Cox, P., Dannerbauer, H., De Breuck, C., Gawiser, E., Ivison, R. J., Lutz, D., Menten, K. M., Koekemoer, A. M., Kreysa, E., Kurczynski, P., Rix, H.-W., Schinnerer, E., & van der Werf, P. P. 2009, ApJ, 707, 1201

Wilson, G. W., Austermann, J. E., Perera, T. A., Scott, K. S., Ade, P. A. R., Bock, J. J., Glenn, J., Golwala, S. R., Kim, S., Kang, Y., Lydon, D., Mauskopf, P. D., Predmore, C. R., Roberts, C. M., Souccar, K., & Yun, M. S. 2008, MNRAS, 386, 807

Zavala, J. A., Arétxaga, I., & Hughes, D. H. 2014, MNRAS, 443, 2384

Zemcov, M., Blain, A., Halpern, M., & Levenson, L. 2010, ApJ, 721, 424

Chapter 3

Radio-detected Faint Submillimeter Galaxies

Note: This chapter originally appeared as Hsu et al. (2017), with co-authors Vandana Desai, Eric J. Murphy, Lennox L. Cowie, Ian Heywood, Emmanuel Momjian, Amy J. Barger, and Ian Smail.

3.1 Introduction

Although our SCUBA-2 surveys are currently the most efficient approach to search for SMGs, the confusion limit (Condon 1974) of JCMT (~ 2 mJy at $850\ \mu\text{m}$) prevents the detection of fainter galaxies with infrared (IR) luminosities $< 10^{12}L_{\odot}$. As a result, there is little information about lower luminosity galaxies, which may be expected to have SFRs comparable to those of the UV/optical populations. Imaging of massive galaxy cluster fields is one way to reach fainter detection limits because background sources are gravitationally magnified. Previous studies have constructed number counts (e.g., Smail et al. 1997, 2002; Cowie et al. 2002; Knudsen et al. 2008; Johansson et al. 2011; Chen et al. 2013a,b; Fujimoto et al. 2016; Hsu et al. 2016) or detected individual sources (Watson et al. 2015; González-López et al. 2017) using submillimeter/millimeter observations of cluster fields.

Given the low spatial resolution of single-dish telescopes (FWHM $\sim 7.^{\circ}5$ at $450\ \mu\text{m}$ and $\sim 14.^{\circ}5$ at $850\ \mu\text{m}$ for JCMT), interferometric follow-up is required to identify the multi-wavelength counterparts to submillimeter sources. While submillimeter interferometry is

the most reliable way to do this, it is observationally expensive. Radio interferometry is an effective alternative that relies on the observed correlation between FIR emission and radio emission from local starburst galaxies (Helou et al. 1985; Condon 1992). Although the physics of this FIR-radio correlation is unclear, the non-thermal synchrotron emission from supernova remnants traces the dust-obscured star formation (e.g., Murphy 2009; Ivison et al. 2010a,b; Momjian et al. 2010). The disadvantage of radio identification is that it does not benefit from a negative K -correction, making it difficult to detect SMGs at $z > 3$.

The Janksy-VLA Frontier Fields Legacy Survey (PI: Eric Murphy) aims to characterize the dust-obscured properties of high-redshift galaxies through Karl G. Jansky Very Large Array (VLA) imaging of all five *HST* Frontier Fields observable with the VLA at 3 and 6 GHz. The goal rms sensitivity of these images is $\lesssim 1 \mu\text{Jy}$ on the image plane, which is achieved for all fields with data in hand. At 6 GHz, these data reach an angular resolution of $0.^{\prime}3$, similar to the resolution of *HST*/WFC3. These data will allow a variety of extragalactic studies, including radio morphologies of star-forming galaxies, obscured star formation out to $z \sim 8$, the evolution of supermassive black holes, and the rapid evolution of galaxies in the lensing clusters themselves. Observations and data reductions of this survey are still ongoing, and the catalogs of detected sources will be presented in a forthcoming paper (Heywood et al. 2017, in preparation).

In this chapter, we present a sample of 14 SCUBA-2 850 μm sources identified with the Janksy-VLA Frontier Fields Legacy Survey in the fields of MACS J0416.1–2403, MACS J0717.5+3745, and MACS J1149.5+2223 (hereafter, MACSJ0416, MACSJ0717, and MACSJ1149). The details of the observations and data reduction are described in Section 3.2. Section 3.3 describes source extraction and sample selection. The derived properties of our sample are discussed in Section 3.4. In Section 3.5, we discuss the detectability of submillimeter sources in radio surveys and optical-near-infrared color selections. Section 3.6 summarizes our results. Throughout this chapter, we assume a Kroupa (2001) initial mass function (IMF) and the concordance ΛCDM cosmology with $H_0 = 70 \text{ km s}^{-1} \text{ Mpc}^{-1}$, $\Omega_M = 0.3$, and $\Omega_\Lambda = 0.7$.

3.2 Data

3.2.1 SCUBA-2 Images

We combined all of our SCUBA-2 data taken between February 2012 and March 2016. We used the CV DAISY scan pattern to detect sources out to $\sim 6'$ from the cluster centers. Most of our observations were carried out under band 1 (the driest weather; $\tau_{225\text{GHz}} < 0.05$) conditions, but there are also data taken under band 2 ($0.05 < \tau_{225\text{GHz}} < 0.08$) or good band 3 conditions ($0.08 < \tau_{225\text{GHz}} < 0.1$). We summarize the details of these observations in Table 3.1.

Following Chen et al. (2013a,b) and Hsu et al. (2016), we reduced the data using the Dynamic Iterative Map Maker (DIMM) in the SMURF package from the STARLINK software (Chapin et al. 2013). DIMM performs pre-processing and cleaning of the raw data (e.g., down-sampling, dark subtraction, concatenation, flat-fielding) as well as iterative estimations to remove different signals from astronomical signal and noise. We adopted the standard “blank field” configuration file, which is commonly used for extragalactic surveys to detect low signal-to-noise ratio (S/N) point sources. Please refer to Hsu et al. (2016) for a detailed description of our SCUBA-2 data reduction and calibration. In Figure 3.1, we show the $850\text{ }\mu\text{m}$ S/N maps for the three cluster fields with the regions of *HST* and VLA 6 GHz observations overlaid.

3.2.2 VLA Images

The VLA observations¹ were carried out in the A (maximum baseline = 36.4 km) and the C (maximum baseline = 3.4 km) configurations using both the S-band (2-4 GHz) and C-band (4-8 GHz) receivers. For the S band, two 1 GHz Intermediate Frequency (IF) band pairs were used, both with right- and left-hand circular polarization, and sampled at 8 bits, while for the C band two 2 GHz IF band pairs were utilized with 3 bit sampling. The 1 and 2 GHz-wide bands were then divided by the WIDAR correlator into 8 and 16 128 MHz

¹Project codes: 14A-012, 15A-282

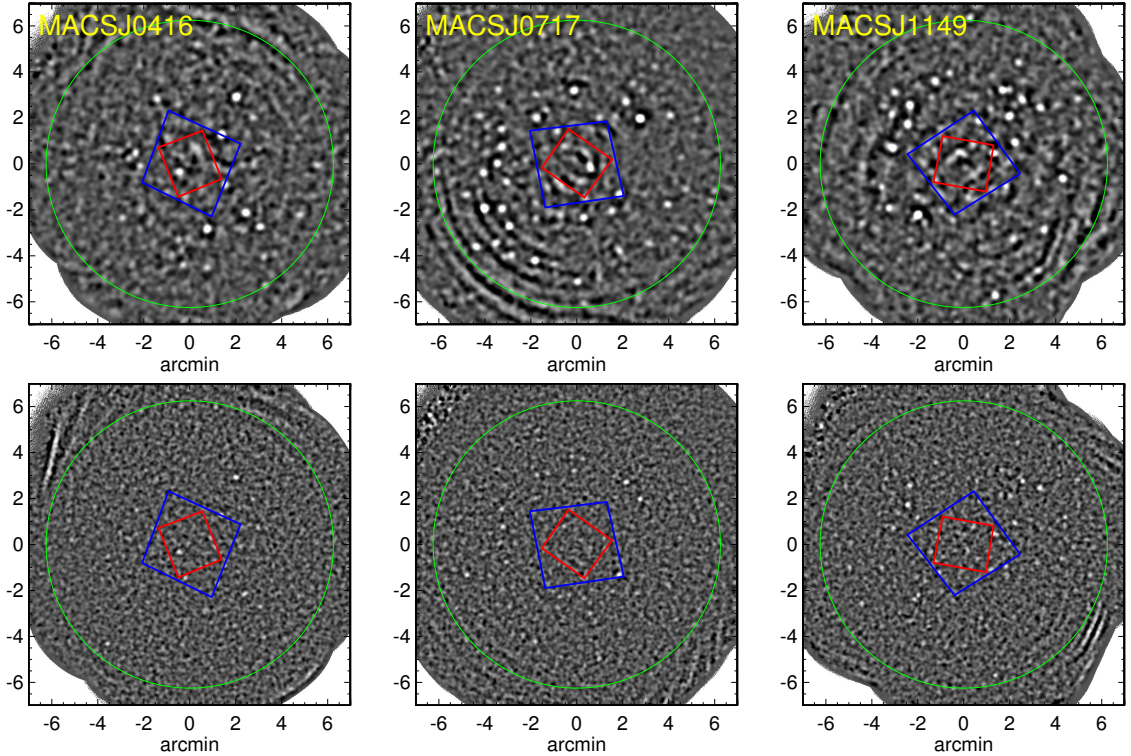


Figure 3.1: $850 \mu\text{m}$ (top) and $450 \mu\text{m}$ (bottom) S/N maps of the three Frontier Fields, MACS J0416.1–2403, MACS J0717.5+3745 and MACS J1149.5+2223. The blue and red boxes represent, respectively, the positions of ACS and WFC3 coverage for the Frontier Field program. The green circles show the coverage of our VLA 6 GHz observations. Our 3 GHz images cover four times the area of the 6 GHz observations. In this work, we focus on the areas of *HST* coverage.

Table 3.1: Summary of JCMT/SCUBA-2 Observations

	Field	R.A.	Decl.	Redshift	Weather ^a	Exposure (hr)	σ^b (mJy beam ⁻¹)
55	MACS J0416.1-2403	04 16 08.9	-24 04 28.7	0.396	1+2+3	24.0+1.0+4.0	[2.31,0.36]
	MACS J0717.5+3745	07 17 34.0	37 44 49.0	0.545	1+2+3	30.7+8.0+1.5	[2.03,0.34]
	MACS J1149.5+2223	11 49 36.3	22 23 58.1	0.543	1+2+3	29.0+3.5+3.4	[1.63,0.30]

^aData were taken in band 1 ($\tau_{225\text{GHz}} < 0.05$), band 2 ($0.05 < \tau_{225\text{GHz}} < 0.08$), or good band 3 ($0.08 < \tau_{225\text{GHz}} < 0.1$) conditions.

^bCentral 1σ sensitivity of the map at 450 and 850 μm . These are the statistical/instrumental noise values directly from the reduced rms maps.

wide spectral windows, respectively, each with 64 spectral channels and four polarization products (RR, LL, RL, and LR). The on-source integration times for each of the three targets, in each of these band / configuration pairs are given in Table 3.2, along with the equatorial coordinates of the targets themselves. The primary and secondary calibrators are also listed for each target.

The data of each individual observing session were initially processed using the NRAO VLA pipeline². This is a set of scripts for the Common Astronomy Software Applications (CASA³; McMullin et al. 2007) package designed to perform basic calibration steps on continuum data for total intensity (Stokes I) science. After Hanning-smoothing, the pipeline performs various data editing steps such as the flagging of data due to antenna shadowing, visibilities with amplitudes that are exactly zero, and integrations when the antennas are not one-source. A first pass of radio frequency interference (RFI) excision from the calibrator and target scans is performed using a sliding window statistical filter. The pipeline also performs delay and bandpass calibration using the primary calibrators. Time-dependent antenna-based complex gain corrections are derived using the secondary calibrator and interpolated for application to the target scans. A gain correction is derived independently for each spectral window.

Following the execution of the pipeline, the target field from each pointing was split into a single measurement set. The CASA MSTRANSFORM task was then used to add a WEIGHT_SPECTRUM column to the visibilities. This column has the same shape as the DATA column and allows a unique weight to be assigned to each visibility point for use in subsequent imaging. The STATWT task was then used to adjust values in the WEIGHT_SPECTRUM based on the time-dependent statistical properties of the visibilities for each baseline. This step (often) proves to be effective at suppressing low-level RFI or other issues with the data that are missed by the automated flagging routines.

The target fields were then imaged using the WSCLEAN software (Offringa et al. 2014) and Briggs weighting (robustness parameter = 0.2), producing images of $16,384 \times 16,384$

²<https://science.nrao.edu/facilities/vla/data-processing/pipeline>

³<http://casa.nrao.edu/>

Table 3.2: Summary of VLA Observations, Including Calibrators and the On-source Integration Times for Each Configuration/band Pairings.

	Band	Config	MACS J0416.1–2403	MACS J0717.5+3745	MACS J1149.5+2223
Primary cal	S		3C48	3C147	3C286
Secondary cal	C	A	J0416-1851	J0714+3534	J1158+2450
Secondary cal	S	C	J0416-1851	J0714+3534	J1150+2417
Integration time (hr)	S	A	35.2	25.2	27.3
Integration time (hr)	C	C	1.92	1.52	1.57
Integration time (hr)	C	A	18.8	13.7	13.9
Integration time (hr)	C	C	1.05	0.56	0.62

pixels, with pixel sizes of $0.^{\prime\prime}1$ and $0.^{\prime\prime}06$ for S and C bands, respectively. Images were produced for each band and each cluster by jointly gridding and deconvolving all of the relevant measurement sets. Spectral behavior of the sources (both intrinsic toward the beam center, and instrumentally perturbed off-axis) was captured during deconvolution by imaging the data in four spectral sub-bands across the band. The approach used by wsclean during deconvolution is to find peaks in the full-band image and then deconvolve these in each sub-band independently. For major-cycle purposes, clean components were fitted by a second order polynomial when predicting the visibility model. Cleaning was terminated after 100,000 iterations or when a the peak pixel in the full-band residual map reached a threshold of $1.0 \mu\text{Jy}$, whichever occurred sooner. Imaging concludes with the model being restored into the full-band residual map, using a 2D Gaussian as fitted to the main lobe of the point spread function as the restoring beam. The data from both configurations (A and C) were combined during deconvolution and imaging. In Table 3.3, we provide the synthesized beams of the images for both bands. We caution that the small beams of these images might resolve out some extended emission and therefore miss some sources.

The primary beam sizes (HPBW) are $\sim 14'$ at S band and $\sim 7'$ at C band. Primary beam correction was applied to the final image by dividing it by a model of the VLA Stokes-I beam at the band center. The model itself was obtained by running the CASA CLEAN task and using the predicted sensitivity (.FLUX) image. This is a somewhat crude approach for data with such a large fractional bandwidth; however (1) primary beam correction via projection-based gridding is not yet viable, and (2) the band center beam model differs from the zeroth-order Taylor-term beam model predicted by the WIDEBANDPBCOR task by a couple of percent at most, so for our purposes the approaches are essentially equivalent.

The data reduction at this stage is designed to provide an initial set of Stokes-I images at S and C bands. Improvements in the imaging is possible via self-calibration techniques and this work is on-going. In-band and dual band (S-C) spectral index maps will be produced

Table 3.3: Synthesized Beams of the 3 and 6 GHz Images for Each Field

Field	3 GHz			6 GHz		
	b_{\max}	b_{\min}	b_{PA}	b_{\max}	b_{\min}	b_{PA}
MACS J0416.1–2403	0''.81	0''.42	0.65°	0''.47	0''.24	20.96°
MACS J0717.5+3745	0''.49	0''.44	78.29°	0''.27	0''.23	-76.10°
MACS J1149.5+2223	0''.44	0''.41	33.38°	0''.24	0''.22	46.37°

Note: b_{\max} , b_{\min} , and b_{PA} represent the major axis FWHM (in arcsecs), minor axis FWHM (in arcsecs), and position angle (in degrees), respectively.

once the calibration is finalized. The observations were also scheduled to allow polarimetric calibration, and this is also forthcoming.

3.2.3 HST Images and Photometry

We retrieved the *HST* Frontier Fields images and the *HST* images from the Cluster Lensing And Supernova survey with Hubble (CLASH; Postman et al. 2012) archive⁴ for the passbands that are not included in the Frontier Fields program. We ran SExtractor (Bertin & Arnouts 1996) in dual-image mode using F814W and F160W as detection bands to produce two sets of photometric catalogs. The deblending parameters DEBLEND_NTHRESH and DEBLEND_MINCONT were set to be 32 and 0.005, respectively. For a source that is within the WFC3 coverage, we use the F160W-detected photometry instead of the F814W-detected one.

3.2.4 Spitzer Images and Photometry

We retrieved the *Spitzer* Frontier Fields data at 3.6 and 4.5 μ m, and we used the *Spitzer* image processing package MOPEX (Makovoz & Khan 2005; Makovoz & Marleau 2005; Makovoz et al. 2006) to extract sources. Photometry estimation and deblending were performed by the default Point Response Function (PRF) fitting algorithm.

⁴<https://archive.stsci.edu/prepds/clash/>

3.2.5 Other Ancillary Data and Photometric Catalogs

Brammer et al. (2016) recently provided deep, calibrated K_s -band images of all six of the Hubble Frontier Fields using the instruments HAWK-I on the VLT and MOSFIRE on the Keck I telescope. We retrieved the images of our three cluster fields and ran SExtractor to perform source extraction. We also obtained the images and photometric catalogs from the CLASH archive that were obtained with Supreme-Cam on the Subaru telescope, WIRCam and MegaCam on the Canada–France–Hawaii telescope (CFHT), as well as the source catalogs of *Herschel* PACS and SPIRE passbands from the *Herschel Lensing Survey* (Rawle et al. 2016).

3.3 Sample Selection

3.3.1 SCUBA-2 Source Extraction

In this work, we focus on 850 μm selected sources, and we detected sources down to a 4σ level. Casey et al. (2013) and Chen et al. (2013a,b) have shown that sources detected above a 4σ level from their SCUBA-2 maps (with central 1σ sensitivity of ~ 0.8 mJy at 850 μm) have a contamination rate of $\leq 5\%$. Following Hsu et al. (2016), we estimate the contamination rate by constructing the source-free "jackknife maps" at both wavelengths. A jackknife map is a pure noise image with sources removed; it is created by subtracting one-half of the data from the other, then scaling each pixel value by a factor of $\sqrt{t_1 \times t_2}/(t_1+t_2)$, with t_1 and t_2 representing the integration time of each pixel from the two halves of data. In each field, we searched for 4σ sources within the area where the noise values are less than three times the central noise (an area of ~ 130 arcmin 2). The ratio of the total number of sources from the jackknife maps and from the science maps is 10/292, or 3.4%. If we only consider the regions that are covered by *HST*/ACS, the ratio is 1/44, or 2.3%.

To perform source extraction, we generated the PSFs by averaging all the primary calibrators. Following the methodology of source extraction in Chen et al. (2013a,b) and Hsu et al. (2016), we identified the pixel with the maximum S/N, subtracted this pixel and

its surroundings using the PSF centered and scaled at the position and value of this pixel, and then searched for the next maximum S/N. We iterated this process until the detection threshold was hit. We only selected sources in the areas covered by the *HST* Frontier Fields since these sources are the most highly lensed ones with deep *HST* photometry. There are 44 850 μm sources within the *HST* coverage. We then measured the 450 μm flux density of each 850 μm source by searching for the maximum 450 μm peak flux within the 850 μm beam.

3.3.2 Flux Deboosting

The flux densities we measured from the SCUBA-2 maps are boosted by both Eddington bias (Eddington 1913) and confusion noise (Condon 1974). In addition, the flux errors we obtained are purely from statistical/instrumental noise, which does not include the above effects. We therefore need to run Monte Carlo simulations to correct the measured flux densities and their uncertainties. To perform such simulations, one normally uses a number counts model to populate sources onto the jackknife map, runs source extraction on this map, and then compares the input and measured flux densities. In a lensed field, however, it is tricky to run these simulations because assumptions of a lens model and a source plane redshift are required to project the simulated sources onto the image plane and to magnify their fluxes.

Here we used a simpler but rather time-consuming method that does not require lens modeling. We added three sources into our science map with random flux densities at random positions at a time and then performed source extraction, recording the input and measured flux densities of the sources we inserted. We only used the central area of each map that is covered by the *HST*. Only a small number of sources were inserted at a time in order to avoid over-crowdedness, such that the flux measurements for these sources are not influenced by each other. We repeated this procedure until we obtained 50000 pairs of input and measured flux densities. An inserted source is considered to be recovered if it is detected within the HWHM of the SCUBA-2 beam from the original input position.

In Figure 2, we show the boosting factor as a function of detection S/N at 450 and 850 μm for MACSJ0416. The boosting factor is measured as the ratio of the measured and input flux densities. The red line in each panel of Figure 2 represents the median boosting factor, and the two blue lines enclose the 1σ spread. We deboosted the flux densities of our sources in each map using the median boosting factor and the corresponding 1σ uncertainty.

3.3.3 Confusion Limit at 850 μm

To estimate the confusion limit of SCUBA-2 observations at 850 μm , we use the formalism of Condon (1974) and define the beam size as $\Omega_b = \pi(\text{FWHM}/2.35)^2$, where FWHM is 14''.5. Following Hogg (2001), an image is considered confused when the source density exceeds one source per 30 beams. We adopt a broken power law for the differential number counts

$$\frac{dN}{dS} = \begin{cases} N_0 \left(\frac{S}{S_0} \right)^{-\alpha} & \text{if } S \leq S_0 \\ N_0 \left(\frac{S}{S_0} \right)^{-\beta} & \text{if } S > S_0 \end{cases} \quad (3.1)$$

We can then calculate the cumulative counts, $N(> S)$, which represents the number density of sources that are brighter than S . Equating $N(> S)$ and $1/30\Omega_b$ leads to the confusion limit of blank fields

$$S_c = \left\{ \frac{\alpha - 1}{N_0 S_0^\alpha} \left[\frac{1}{30\Omega_b} + N_0 S_0 \left(\frac{1}{\alpha - 1} - \frac{1}{\beta - 1} \right) \right] \right\}^{\frac{1}{1-\alpha}} \quad (3.2)$$

Adopting the best-fit parameters of the broken power law in Hsu et al. (2016), we obtain $S_c = 1.64 \text{ mJy}$.

In a lensed field, the cumulative number counts become $N_{\text{lens}}(> S) = N(> S/\mu)/\mu$, where μ is the lensing magnification and S is the observed flux density. Equating $N_{\text{lens}}(> S)$ and $1/30\Omega_b$, we obtain the observed confusion limit, S_c (on the image plane), as a function of μ . The confusion limit on the source plane is S_c/μ . The observed confusion limit is higher than that of blank fields, but on the source plane it is lower. For example, S_c and S_c/μ are ~ 1.93 and 0.96 , respectively, for $\mu = 2$.

Since we have detected sources down to a deboosted flux density of ~ 1.4 mJy, many of them should be close to or below the observed confusion limit (which depends on μ and therefore position). As a consequence, we caution that our source detection at $S_{850\mu\text{m}} \lesssim 2$ mJy is not complete because there must be sources that we missed due to source confusion.

3.3.4 VLA Source Extraction

Given the higher detection rate at 3 GHz than at 6 GHz, we used the 3 GHz images to search for the counterparts to our 850 μm sources. To extract the flux densities and positions of the 3 GHz sources, we first identified all the pixels that are local maxima and have $\text{S/N} \geq 5$. We took the values of these pixels as the peak fluxes (per beam) of the sources. We then used the CASA IMFIT task to fit 2D Gaussian functions to measure another set of flux densities. Note that some of the flux densities measured with this method have $\text{S/N} < 5$, but we still keep these sources given their well detected peak fluxes.

Using the source positions at 3 GHz as prior, we searched for the 6 GHz counterparts with 5σ -detected peak fluxes. For the sources that are not detected at 6 GHz, we measured their 5σ limits at the 3 GHz positions. We again used IMFIT to measure a second set of flux densities for the detected 6 GHz sources. In addition, we measured another set of flux densities with IMFIT from the 6 GHz images that were convolved to match the beams of our 3 GHz images, using the CASA IMSMOOTH task. This set of measurements along with the 3 GHz flux densities will be used to compute the spectral indices of our radio sources (Section 3.4.2). We adopted this procedure to counter the beam/resolution difference between the two bands.

Further discussion about the source extraction as well as its completeness and contamination rate will be presented in the upcoming paper, Heywood et al. (2017, in preparation).

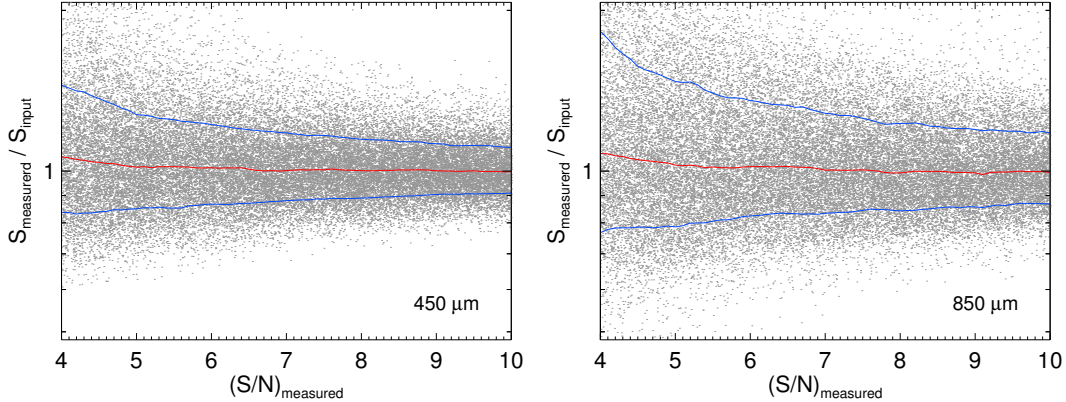


Figure 3.2: Boosting factor as a function of detection S/N at $450\text{ }\mu\text{m}$ (left) and $850\text{ }\mu\text{m}$ (right) for MACS J0416.1–2403 from our Monte Carlo simulations. The boosting factor is measured as the ratio of the measured and input flux densities. The red line in each panel represents the median boosting factor, and the two blue lines enclose the 1σ spread. We deboosted the flux densities of our sources in each map using the median boosting factor and the corresponding 1σ uncertainty.

3.3.5 Counterpart Identification at 3 GHz

We used the corrected-Poissonian probability (Downes et al. 1986), the so-called p -values, as well as redshift cuts to perform counterpart identification. A radio source is considered the counterpart to the SCUBA-2 source if $p < 0.05$ and its redshift is higher than the corresponding cluster redshift. The p -value is defined as $p = 1 - \exp(\pi n \theta^2)$, where n is the radio source density⁵ and θ is the offset between the radio and the submillimeter sources. We adopted the redshift cuts as well because galaxies at redshifts lower than the cluster redshifts are not the lensed, faint galaxies that we are interested in. Besides, $850\text{ }\mu\text{m}$ selected SMGs have been mostly found at $z > 0.5$ (Chapman et al. 2003, 2005). Therefore, those low-redshift galaxies are most likely just random radio sources that are not associated with our SCUBA-2 sources.

A total of 17 radio sources have $p < 0.05$, four of which have spectroscopic redshifts (Ebeling et al. 2014; Schmidt et al. 2014; Grillo et al. 2015; Treu et al. 2015; Balestra et al. 2016). We used the BPZ code (Bayesian photometric redshift estimation; Benítez

⁵ $n = 6.1 \times 10^{-4}\text{ arcsec}^{-2}$, $6.0 \times 10^{-4}\text{ arcsec}^{-2}$, and $8.8 \times 10^{-4}\text{ arcsec}^{-2}$ for MACSJ0416, MACSJ0717, and MACSJ1149, respectively.

2000) and the default galaxy templates (Benítez et al. 2004; Coe et al. 2006) to compute the photometric redshifts of those galaxies without spectroscopic redshifts. We fitted the templates to the *HST* photometry using isophotal magnitudes and obtained robust photometric redshifts for the sources that are detected in at least four bands (but not four ACS bands exclusively). One source in MACSJ0717 (0717-1 in Table 3.4) is only covered in three *HST*/ACS bands but is covered in the Subaru and CFHT images from CLASH. For this source, we simply took the photometric redshift ($z = 1.14^{+0.07}_{-0.10}$) from the CLASH Subaru catalog⁶. We corrected all of the magnitudes for Galactic dust extinction from Schlafly & Finkbeiner (2011) before running BPZ.

For the sources without spectroscopic and photometric redshifts (0416-4 and 0717-2 in Table 3.4), we used their 450 μm -to-850 μm flux ratios to crudely estimate the source redshifts. We converted the flux ratios to redshifts using a modified blackbody spectral energy distribution (SED) of the form $S_\nu \propto (1 - e^{-\tau(\nu)})B_\nu(T)$, where $\tau(\nu) = (\nu/\nu_0)^\beta$ and $\nu_0 = 3000$ GHz, assuming $\beta = 1.5$ and dust temperature of 41.2 K. We chose this value of the dust temperature based on the results of our model fits to the FIR photometry, which we will describe in Section 3.4.1.

We removed two of these 17 radio sources with $p < 0.05$ because of their low redshifts. Our final sample therefore consists of 14 SCUBA-2 sources and 15 3 GHz counterparts (one doublet). Only five of the SCUBA-2 sources (six of the radio counterparts) are detected at 6 GHz with peak fluxes above a 5σ level. We show the 3 GHz and *HST*/ACS images of this final sample in Figure 3. Table 3.4 gives the coordinates, redshifts, observed SCUBA-2 and radio flux densities of these galaxies. It is possible that a radio counterpart is not responsible for the total emission of the corresponding 850 μm source, given that blended multiples are common for single-dish submillimeter sources (e.g., Wang et al. 2011; Barger et al. 2012; Smolčić et al. 2012; Hodge et al. 2013; Bussmann et al. 2015; Simpson et al. 2015). However, in this work, we assume that these 15 radio sources contribute the total 850 μm

⁶Note that, in Rawle et al. (2016), the photometric redshift ($z = 0.89$) from the CLASH *HST* catalog is used for this source. We chose the value from the CLASH Subaru catalog because this source is detected in only two *HST* bands of CLASH but detected in six Subaru/CFHT bands.

emission, in order to derive the IR properties of our 14 SCUBA-2 sources (Section 3.4.1). Submillimeter/millimeter interferometry is the only method to find out whether there are other radio-faint counterparts to these SCUBA-2 sources.

Cowie et al. (2017) inspected the positional uncertainty of the SCUBA-2 850 μm sources detected in the *Chandra* Deep Field-North (CDF-N). They found that the offsets between the SCUBA-2 positions and the SMA positions or the 1.4 GHz counterparts are all $< 4''.5$ for 102 sources with 850 μm flux densities above 2 mJy. In our final sample, only 0717-4 has an offset of $\sim 5''.1$ between the radio and submillimeter positions, and the others have offsets of $< 4''.5$. Besides, $p = 0.05$ essentially corresponds to matching radii of $\sim 5''.2$, $5''.2$, and $4''.3$ for MACSJ0416, MACSJ0717, and MACSJ1149, respectively. Our results are therefore quite consistent with what Cowie et al. found. If we chose a fixed matching radius of $4''.5$ and the same redshift cuts for counterpart matching, we would obtain a sample of 14 SCUBA-2 sources with only one source different from 0717-4.

3.3.6 Lens Models

In order to compute the intrinsic flux densities, luminosities, and SFRs of our lensed SMGs, the lensing magnifications are required, which depend on both the source redshifts and the lens models of the clusters. A set of lens models from eight independent teams are available for the *HST* Frontier Fields. These teams include Bradac (Bradač et al. 2005, 2009; Hoag et al. 2016), CATS (Jullo & Kneib 2009; Jauzac et al. 2012, 2014, 2015b,a; Richard et al. 2014), Diego (Diego et al. 2005a,b, 2007, 2015), GLAFIC (Oguri 2010; Kawamata et al. 2016), Merten (Merten et al. 2009, 2011), Sharon (Jullo et al. 2007; Johnson et al. 2014), Williams (Liesenborgs et al. 2006; Mohammed et al. 2014; Grillo et al. 2015; Sebesta et al. 2016), and Zitrin (Zitrin et al. 2009, 2013).

Following Coe et al. (2015), we estimated the median and 68.3% range of the magnification values from the full range of each model in the *HST* Frontier Fields archive⁷ as well as the uncertainties of the source redshifts. The Merten models are excluded in

⁷<https://archive.stsci.edu/prepds/frontier/lensmodels/>

our estimations because they have much lower resolution ($8.\rlap{''}33$). For each field, we used the newest model from each team. However, because different models have different spatial coverage, different sources in the same field are often not covered by the same amount of lens models.

In order to be consistent for the sources in the same field, for MACSJ0416 and MACSJ0717, we only used the models that cover all the sources in each field. However, for MACSJ1149, only the CATS and Sharon models can cover all the six sources, which would result in much smaller systematic errors of magnifications than those of the sources in the other two fields. Ideally, at least three models should be included to examine the systematic effect on the magnifications. We therefore used a set of four models, which all cover 1149-1, 1149-2, 1149-3, 1149-4, and 1149-6, and a different set of three models (all the available models) for 1149-5. In Table 3.5, we tabulate the models we included and the resulting lensing magnification for each of our sources.

3.4 Properties of Radio-detected Submillimeter Sources

3.4.1 Dust Temperatures and IR SFRs

We cross-match our final sample of SCUBA-2 sources with the source catalog from the *Herschel Lensing Survey* (Rawle et al. 2016). Using the 3 GHz positions as prior, 10 of the 14 sources have a nearest *Herschel* detection with an offset of $< 1''$. On the other hand, the remaining four sources have no *Herschel* counterpart even when a $10''$ matching radius is used. For the 10 sources with *Herschel* detections, the optical counterparts we identified completely agree with the optical counterparts Rawle et al. found. Additionally, 0416-1 and 1149-2 are detected by the Atacama Large Millimeter/submillimeter Array (ALMA) 1.1 mm imaging of González-López et al. (2017) as MACSJ0416-ID01 and MACSJ1149-ID01, respectively. We also estimate the 5σ limit of 1.1 mm flux density for 1149-3, which is the only other source covered by the ALMA maps. The observed *Herschel* and ALMA 1.1 mm flux densities are shown in Table 3.6.

Table 3.4: Coordinates and Redshifts, As Well As SCUBA-2 and VLA Flux Densities of the 3 GHz Identified Sample of 850 μm Sources

ID	R.A.	Decl.	Redshift	$S_{850\mu\text{m}}$ (mJy)	$S_{450\mu\text{m}}$ (mJy)	$S_{3\text{GHz,peak}}$ ($\mu\text{Jy beam}^{-1}$)	$S_{3\text{GHz,fit}}$ (μJy)	$S_{6\text{GHz,peak}}$ ($\mu\text{Jy beam}^{-1}$)	$S_{6\text{GHz,fit}}$ (μJy)	$S_{6\text{GHz-cv,fit}}$ (μJy)	
0416-1	04 16 10.80	-24 04 47.6	2.087 (s)	4.38 ± 0.72	14.5 ± 3.5	8.0 ± 1.0	14.7 ± 3.3	< 4.3
0416-2	04 16 13.23	-24 03 19.8	0.9063 (s)	2.22 ± 0.79	7.5 ± 3.5	12.2 ± 1.1	27.8 ± 4.1	< 5.6
0416-3	2.18 ± 0.79	14.1 ± 4.0
0416-3-1	04 16 09.68	-24 05 55.4	0.99 ± 0.10 (p)	31.1 ± 1.1	55.4 ± 3.7	10.4 ± 1.1	20.8 ± 3.5	32.9 ± 4.6	...
0416-3-2	04 16 09.64	-24 05 55.2	1.01 ± 0.10 (p)	29.5 ± 1.1	31.9 ± 2.4	13.0 ± 1.1	17.0 ± 2.4	18.5 ± 2.6	...
0416-4	04 16 12.96	-24 05 43.0	2.7 ^{+2.7} _{-2.2} (r)	1.78 ± 0.83	5.5 ± 3.4	11.8 ± 1.0	13.6 ± 2.1	5.7 ± 1.0	9.0 ± 2.3	8.6 ± 2.3	...
0717-1	07 17 24.55	37 43 29.7	1.14 ^{+0.67} _{-0.10} (p)	5.65 ± 0.88	18.7 ± 3.9	6.8 ± 0.9	18.2 ± 3.4	< 6.2
0717-2	07 17 38.15	37 46 17.0	4.5 ^{+2.3} _{-1.3} (r)	3.25 ± 0.68	4.9 ± 2.9	5.6 ± 1.0	5.1 ± 1.5	< 5.5
0717-3	07 17 33.20	37 44 01.5	1.54 ± 0.13 (p)	2.21 ± 0.61	7.2 ± 2.9	6.5 ± 1.1	15.2 ± 3.5	< 5.3
0717-4	07 17 32.40	37 43 19.7	0.78 ± 0.09 (p)	2.24 ± 0.69	6.9 ± 3.1	42.1 ± 1.0	48.9 ± 1.9	18.2 ± 1.0	24.3 ± 2.3	23.4 ± 1.6	...
1149-1	11 49 30.66	22 24 27.8	1.36 ± 0.12 (p)	4.75 ± 0.76	15.4 ± 2.7	5.2 ± 1.0	27.4 ± 8.3	< 4.9
1149-2	11 49 36.07	22 24 24.5	1.28 ± 0.11 (p)	2.20 ± 0.61	5.7 ± 2.3	6.6 ± 1.0	14.1 ± 4.0	< 5.1
1149-3	11 49 34.41	22 24 45.3	0.9754 (s)	2.23 ± 0.64	7.9 ± 2.6	14.4 ± 1.0	18.0 ± 2.0	8.0 ± 1.0	12.0 ± 2.3	12.4 ± 1.8	...
1149-4	11 49 35.47	22 22 32.0	1.24 ± 0.11 (p)	2.37 ± 0.69	4.1 ± 2.3	6.9 ± 1.0	12.5 ± 3.6	< 5.1
1149-5	11 49 42.37	22 23 39.6	1.56 ± 0.13 (p)	1.93 ± 0.74	8.1 ± 2.9	10.0 ± 1.0	12.1 ± 2.1	5.3 ± 1.0	9.1 ± 2.6	7.3 ± 1.5	...
1149-6	11 49 40.14	22 22 33.4	0.93 ± 0.10 (p)	1.55 ± 0.77	3.1 ± 2.1	10.5 ± 1.0	17.2 ± 2.7	< 4.7

R.A. and Decl. are the positions of 3 GHz flux peaks. Column 4: (s) stands for spectroscopic redshifts; (p) stands for photometric redshifts; and (r) stands for redshift estimates based on 450 μm -to-850 μm flux ratios. Columns 5 & 6: deboosted SCUBA-2 flux densities. Columns 7 & 9: peak fluxes; 5 σ limits are provided for the sources that are not detected at 6 GHz. Columns 8 & 10: flux densities measured with a 2D Gaussian. Column 11: flux densities measured with a 2D Gaussian from the 6 GHz images convolved to match the beams of the 3 GHz images.

Table 3.5: Lens Models Used for Each Source and the Resulting Magnification Value

ID	Magnification	Models			
0416-1	$1.83^{+0.54}_{-0.07}$	Bradac-v3	CATS-v3.1	Sharon-v3	"
0416-2	$1.67^{+0.11}_{-0.14}$				"
0416-3	$1.57^{+0.26}_{-0.42}$				"
0416-4	$1.21^{+0.53}_{-0.08}$				"
0717-1	1.28 ± 0.16	Bradac-v1	CATS-v1	GLAFIC-v3	Sharon-v2
0717-2	$2.12^{+0.42}_{-0.36}$			Zitrin-LTM-v1	Zitrin-LTM-Gauss-v1
0717-3	$3.04^{+0.95}_{-0.43}$			"	"
0717-4	$1.20^{+0.09}_{-0.07}$			"	"
1149-1	$1.64^{+0.21}_{-0.35}$	CATS-v1	Sharon-v2.1	Zitrin-LTM-v1	Zitrin-LTM-Gauss-v1
1149-2	$2.89^{+0.66}_{-0.54}$			"	"
1149-3	$3.08^{+1.20}_{-0.44}$			"	"
1149-4	$1.19^{+0.20}_{-0.08}$	CATS-v1	Sharon-v2.1	GLAFIC-v3	"
1149-5	$1.44^{+0.07}_{-0.18}$				
1149-6	$1.18^{+0.10}_{-0.15}$	CATS-v1	Sharon-v2.1	Zitrin-LTM-v1	Zitrin-LTM-Gauss-v1

Note: The uncertainties of magnifications are propagated from the uncertainties of redshifts and lens models themselves.
A " sign means that the models are the same as the above. Note that for MACSJ0416, the CATS team provided two newest models (v3 and v3.1), which are based on the same data and method but a different amount of multiple images.
Here we use the v3.1 model.

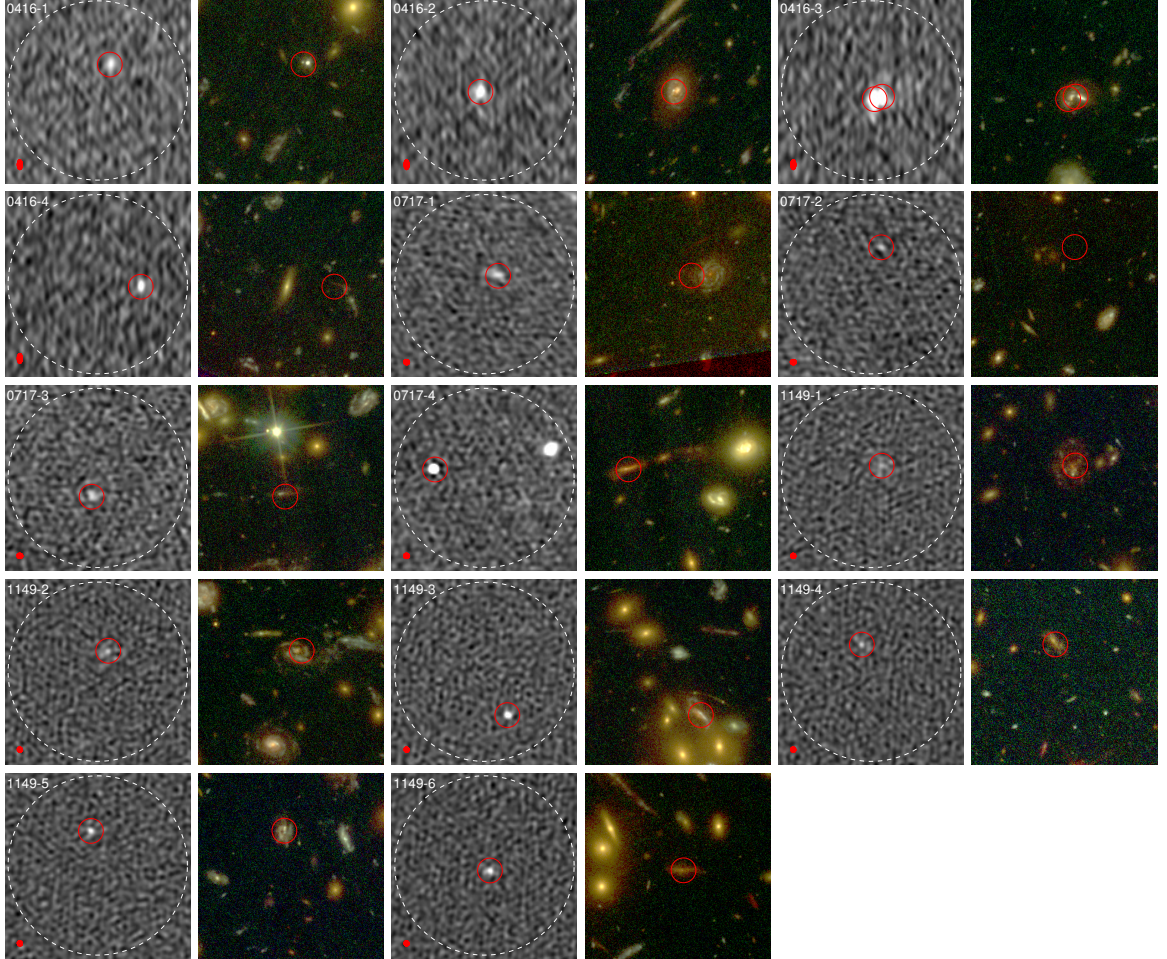


Figure 3.3: 3 GHz identified sample of SCUBA-2 $850\text{ }\mu\text{m}$ sources that are within the *HST* Frontier Fields coverage. For each source, we show the 3 GHz image on the left and the ACS false-color (F435W, F606W and F814W) image on the right. The image size is $15'' \times 15''$. In the 3 GHz images, the large dashed circles with a diameter of $14''.5$ represent the JCMT beam (FWHM) at $850\text{ }\mu\text{m}$. The positions of the 3 GHz counterparts are indicated by the $1''$ -radius red circles in both the 3 GHz and ACS images. The ellipse at the bottom-left corner of each 3 GHz image represents the synthesized beam. Note that another bright radio source also locates within the SCUBA-2 beam of 0717-4. However, this source is not considered the counterpart because $p > 0.05$ and it is at $z \sim 0.3$.

Table 3.6: *Herschel* and ALMA 1.1 mm Flux Densities from Rawle et al. (2016) and González-López et al. (2017)

ID	$S_{100\mu\text{m}}$ (mJy)	$S_{160\mu\text{m}}$ (mJy)	$S_{250\mu\text{m}}$ (mJy)	$S_{350\mu\text{m}}$ (mJy)	$S_{500\mu\text{m}}$ (mJy)	$S_{1100\mu\text{m}}$ (mJy)
0416-1	5.1 ± 1.0	12.6 ± 2.0	(9.7 ± 3.1)	(6.8 ± 2.6)	...	1.32 ± 0.10
0416-2	11.1 ± 1.2	24.5 ± 2.2	(9.1 ± 3.5)	(4.7 ± 2.9)
0416-3	20.1 ± 1.7	36.4 ± 3.2	31.5 ± 3.9	24.2 ± 3.5	10.5 ± 3.7	...
0416-4
0717-1	3.8 ± 0.8	15.2 ± 1.8	31.0 ± 3.8	34.2 ± 4.7	16.9 ± 3.0	...
0717-2
0717-3
0717-4
1149-1	7.0 ± 0.9	16.4 ± 1.8	32.3 ± 3.2	30.3 ± 3.2	21.4 ± 2.8	...
1149-2	3.7 ± 0.7	7.9 ± 1.5	(5.9 ± 2.5)	0.58 ± 0.13
1149-3	7.7 ± 1.0	18.4 ± 1.9	23.7 ± 3.7	14.2 ± 3.0	6.1 ± 3.9	< 0.57
1149-4	3.2 ± 0.7	9.6 ± 1.4
1149-5	5.0 ± 0.8	10.0 ± 1.4	12.5 ± 2.5	5.7 ± 2.8
1149-6	6.2 ± 0.9	11.3 ± 1.7	12.6 ± 2.6	7.4 ± 3.3	3.8 ± 3.4	...

Note: Flux densities enclosed by parentheses are flagged in the FIR fits described in Section 3.4.1.

For four sources, we found that the *Herschel*/SPIRE photometry does not agree well with our SCUBA-2 flux densities. Compared with the SCUBA-2 photometry, the SPIRE SEDs of these sources turn over at shorter wavelengths. This inconsistency might be caused by the PSF-fitting procedure and/or deblending photometry performed by Rawle et al. (2016). We therefore decided to flag the SPIRE flux densities that are a factor of two lower than the best-fit modified blackbody models for the SEDs constructed from the *Herschel*/PACS, SCUBA-2, and ALMA (if available) photometry. These flags are done for 0416-1, 0416-2, and 1149-2, which are presented in Table 3.6 and Figure 4.

For the sources with spectroscopic or photometric redshifts, we measure their dust temperatures by fitting a modified blackbody model with $\beta = 1.5$ (e.g., Chapman et al. 2005; Kovács et al. 2006; Pope et al. 2006) to the FIR flux densities. The resulting median dust temperature is $41.2^{+1.8}_{-2.0}$ K. We therefore use $\beta = 1.5$ and $T = 41.2$ K to estimate the redshifts for the remaining two sources (0416-4 and 0717-2) that have no redshift measurements. Note that only 450 and 850 μm flux densities are available for these two sources as well as 0717-3

Table 3.7: Dust Temperatures, IR Luminosities, and SFRs

ID	T (K)	L_{IR} ($10^{11}L_{\odot}$)	SFR_{IR} ($M_{\odot} \text{ yr}^{-1}$)	$\text{SFR}_{6\text{GHz}}$ ($M_{\odot} \text{ yr}^{-1}$)	SFR_{UV} ($M_{\odot} \text{ yr}^{-1}$)
0416-1	51.2 ± 2.0	$17.0_{-3.4}^{+2.3}$	253_{-51}^{+34}	226_{-71}^{+40}	$28.2_{-6.4}^{+1.2}$
0416-2	$41.2_{-2.3}^{+2.4}$	$4.85_{-0.49}^{+0.57}$	72_{-7}^{+8}	67 ± 11	$2.3_{-0.1}^{+0.2}$
0416-3	$44.8_{-2.4}^{+2.6}$	$9.76_{-2.31}^{+3.84}$	146_{-34}^{+57}	281_{-45}^{+87}	$5.6_{-1.0}^{+2.0}$
0416-4	519_{-482}^{+1601}	...
0717-1	29.3 ± 1.8	$8.34_{-1.99}^{+1.52}$	124_{-30}^{+23}	99_{-31}^{+23}	$4.3_{-1.2}^{+0.8}$
0717-2	372_{-225}^{+481}	...
0717-3	$27.9_{-8.9}^{+19.1}$	70_{-24}^{+20}	0.8 ± 0.2
0717-4	$17.9_{-5.8}^{+14.9}$	112_{-24}^{+27}	$0.1_{-0.1}^{+0.2}$
1149-1	$35.6_{-2.5}^{+2.6}$	$10.9_{-2.3}^{+2.4}$	162_{-34}^{+36}	176_{-60}^{+75}	$1.5_{-0.4}^{+0.7}$
1149-2	$40.4_{-3.8}^{+4.8}$	$2.40_{-0.47}^{+0.61}$	36_{-7}^{+9}	44_{-15}^{+14}	$2.3_{-0.4}^{+0.5}$
1149-3	$38.2_{-1.7}^{+1.9}$	$2.43_{-0.71}^{+0.51}$	36_{-11}^{+8}	28_{-8}^{+7}	$1.2_{-0.3}^{+0.2}$
1149-4	$41.3_{-4.8}^{+5.5}$	$5.47_{-1.37}^{+1.25}$	82_{-20}^{+19}	89_{-31}^{+29}	0.7 ± 0.1
1149-5	$54.9_{-5.2}^{+6.0}$	$8.50_{-1.65}^{+1.56}$	127_{-25}^{+23}	121_{-28}^{+40}	$3.2_{-0.8}^{+1.2}$
1149-6	$42.4_{-4.0}^{+4.2}$	$3.65_{-0.72}^{+1.01}$	55_{-11}^{+15}	63_{-16}^{+21}	0.1 ± 0.1

Note. — The uncertainties of dust temperatures include photometric errors and the uncertainties of redshifts. The uncertainties of IR luminosities and SFRs include photometric errors as well as the uncertainties of redshifts and lensing magnifications. Because 0416-1 is classified as an AGN in the GLASS survey (Schmidt et al. 2014; Treu et al. 2015), it is unclear if the radio and UV emission is dominated by the AGN or star formation. We caution that the radio and UV SFRs for this source can only be considered as upper limits.

and 0717-4 because they are not detected in *Herschel Lensing Survey*. As a consequence, what we do is simply match the models and the 450 μm -to-850 μm flux ratios instead of least chi-squared fitting.

We fit the templates of Rieke et al. (2009) to the FIR flux densities for the 10 sources that are detected by *Herschel* to derive their IR luminosities (L_{IR} ; $\lambda_{\text{rest}} = 8\text{-}1000 \mu\text{m}$). L_{IR} is then converted to SFR via the theoretical relation in Murphy et al. (2011). Both the L_{IR} and SFRs are corrected for the lensing magnifications based on our redshifts and the lens models. We do not compute the IR SFRs of 0416-4, 0717-2, 0717-3, and 0717-4 since they are only detected at 450 and 850 μm . We show these fits in Figure 4. All the derived quantities are listed in Figure 4 (without uncertainties) and Table 3.7.

3.4.2 Radio SFRs

Following Murphy et al. (2011, 2012), we compute the radio SFRs of our sources using the relation

$$\left(\frac{\text{SFR}_\nu}{M_\odot \text{ yr}^{-1}}\right) = 10^{-27} \left[2.18 \left(\frac{T_e}{10^4 \text{ K}}\right)^{0.45} \left(\frac{\nu}{\text{GHz}}\right)^{-0.1} + 15.1 \left(\frac{\nu}{\text{GHz}}\right)^{-\alpha^{\text{NT}}} \right]^{-1} \left(\frac{L_\nu}{\text{erg s}^{-1} \text{ Hz}^{-1}}\right) \quad (3.3)$$

where we assume an electron temperature of $T_e = 10^4 \text{ K}$, and a constant non-thermal radio spectral index of $\alpha^{\text{NT}} = 0.85$, which is the average non-thermal spectral index found among the 10 star-forming regions in NGC 6946 studied by Murphy et al. (2011). Since our sources are all detected at 3 GHz and have a median redshift close to one, we decide to compute the rest-frame 6 GHz SFRs. In order to K -correct an observed radio flux density to rest-frame 6 GHz, we need the radio spectral index, α , which relates the radio flux density with frequency via a power law $S_\nu \propto \nu^{-\alpha}$. We can then calculate the rest-frame 6 GHz radio luminosities using

$$L_{\nu_{\text{rest}}}(6 \text{ GHz}) = 4\pi d_L^2 S_{\nu_{\text{obs}}}(3 \text{ GHz})(1+z)^{\alpha-1} \times 2^{-\alpha} \quad (3.4)$$

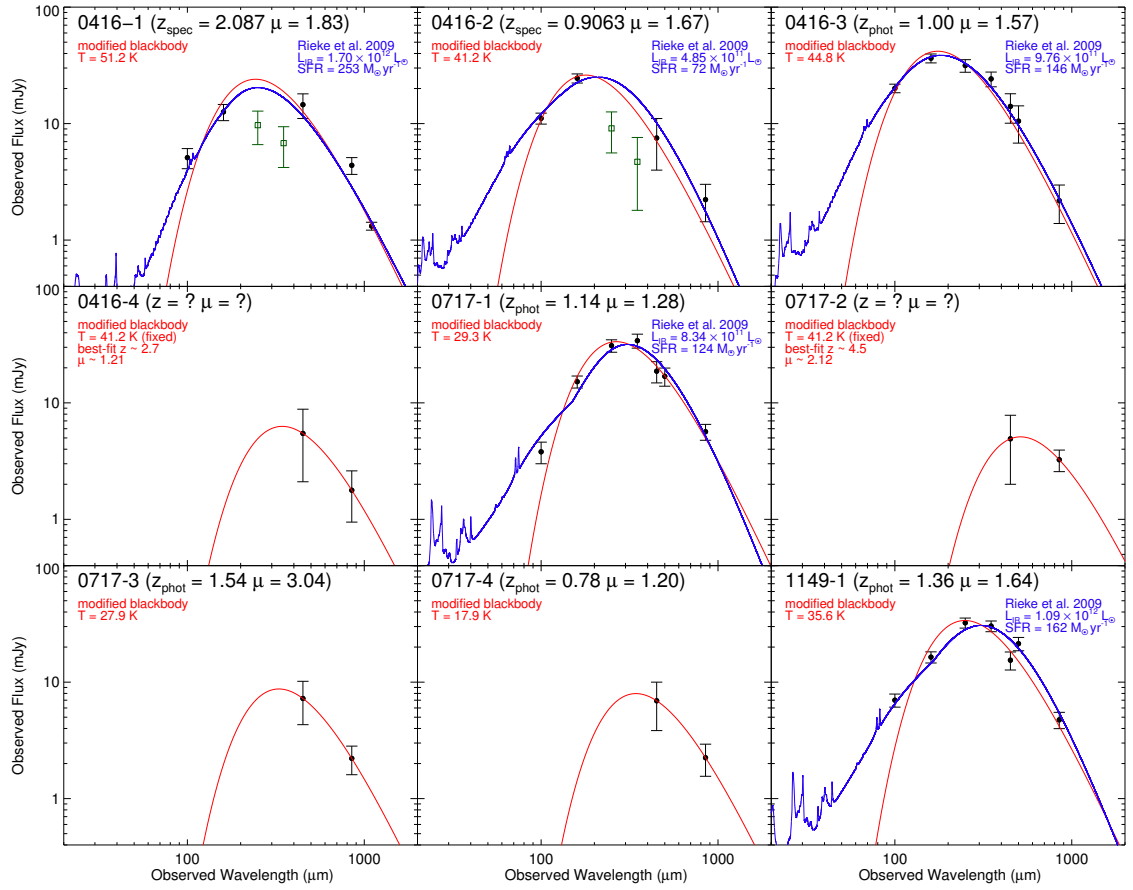


Figure 3.4: FIR SEDs of our 3 GHz identified sample of SCUBA-2 850 μm sources that illustrate the observed photometry and fits. The flux densities are from *Herschel*/PACS (100 and 160 μm), *Herschel*/SPIRE (250, 350, and 500 μm), SCUBA-2 (450 and 850 μm), and ALMA (1.1mm). The *Herschel* and ALMA flux densities are from Rawle et al. (2016) and González-López et al. (2017), respectively. The SPIRE flux densities shown as green squares are flagged in the fits. In each panel, we plot the best-fit modified blackbody (red line) and Rieke et al. (2009) template (blue line). (Note that for 0416-4, 0717-2, 0717-3, and 0717-4, only the SCUBA-2 flux densities are available. Therefore, the plotted red lines are just the modified blackbody models that match the 450 μm -to-850 μm flux ratios, and are not from least chi-squared fitting.) Derived quantities from the two models are shown in matching colors, including IR luminosities and SFRs, which take the magnifications (μ) into account. 12 of the 14 sources have spectroscopic (z_{spec}) or photometric (z_{phot}) redshifts. For the two sources without redshifts, we use a modified blackbody with the median dust temperature from the other 11 sources (41.2 K) to convert their 450 μm -to-850 μm flux ratios to redshifts and therefore magnifications. The uncertainties of all the quantities are listed in Table 3.7. This figure continues in the next page.

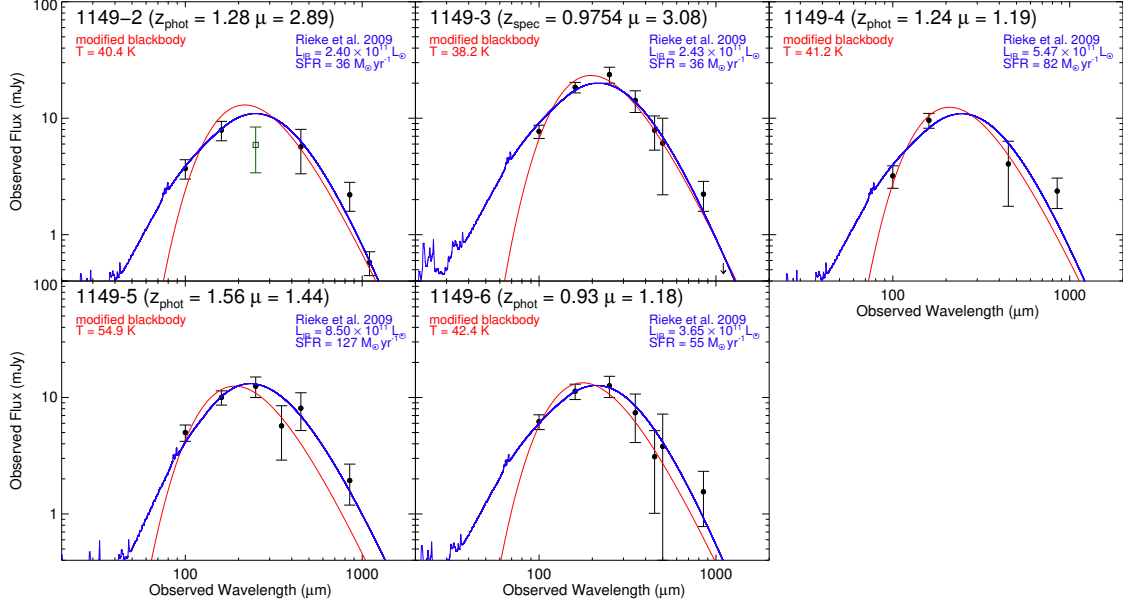


Figure 3.4: (Continued)

where d_L is the luminosity distance. This calculation includes a bandwidth compression term of $(1+z)^{-1}$ and a color term of $(\frac{2}{1+z})^{-\alpha}$. For the six radio sources that are detected at both bands, we directly compute their spectral indices using the flux densities measured from the 3 GHz images and the convolved 6 GHz images with the Gaussian fitting procedure. We obtain an average of 0.76 ± 0.12 from these six sources, which is consistent with the values in the literature (e.g., Ibar et al. 2009; Ivison et al. 2010a,b). We assume this value for the other sources. The resulting radio SFRs are tabulated in Table 3.7.

3.4.3 UV SFRs

While the radio and IR SFRs represent the total and dust-obscured SFRs, respectively, the unobscured contributions from the (observed) UV emission should be accounted as well, given that most of our sources are detected in the optical images. We use rest-frame 2271 Å (*GALEX* NUV band) flux densities and the conversion in Murphy et al. (2012) to compute the UV SFRs of our sources without extinction correction. We interpolate the *HST* photometry to obtain rest-frame 2271 Å flux densities and then compute L_{NUV} and UV SFRs. These UV SFRs are also tabulated in Table 3.7, along with radio and IR SFRs.

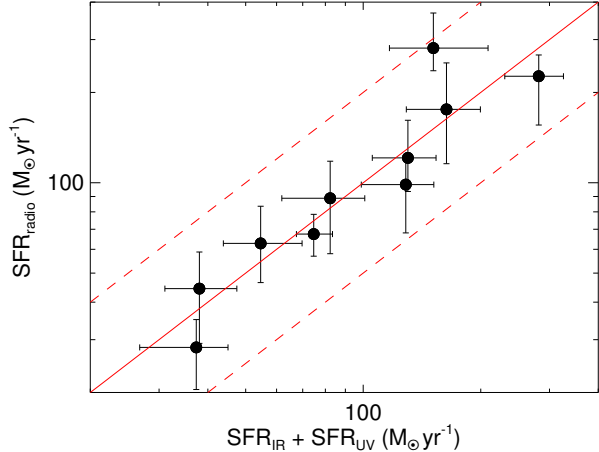


Figure 3.5: Comparison between the radio SFRs and the IR+UV SFRs for the 10 sources that have IR SFR measurements. These SFRs are corrected for the lensing magnifications. The red solid line is the one-to-one relation. All of the 10 sources are within a multiplicative factor of two about the one-to-one line (the two red dashed lines).

In Figure 5, we compare the radio SFRs with the IR+UV SFRs for the 10 sources that have IR SFR measurements. The UV SFRs are mostly too small to significantly affect the comparison except for 0416-1.

3.4.4 $850 \mu\text{m}$ Flux Density to SFR Conversion

The observed (but de-lensed) $850 \mu\text{m}$ flux density of an SMG should work as a proxy of the IR luminosity and IR SFR independent of redshift since the strong negative K -correction and the effect of distance almost exactly cancel out (e.g., Blain & Longair 1993; Blain et al. 2002). Barger et al. (2014) and Cowie et al. (2017) have both measured the mean conversion between observed $850 \mu\text{m}$ flux density and IR SFR from their samples, with a multiplicative range over the individual values of two in each direction about the mean. Here we perform the same exercise, comparing our observed $850 \mu\text{m}$ flux densities and IR SFRs for the 10 sources that have IR SFR measurements in Figure 6. The median conversion of these sources is $\text{SFR}_{\text{IR}}(M_\odot \text{ yr}^{-1}) = 54 \times S_{850\mu\text{m}} (\text{mJy})$, which is more than a factor of two smaller than the conversion (143) found in Cowie et al. (2017). However, the median redshifts of

the two samples are $z = 1.24$ (this work) and $z = 2.28$ (Cowie et al.). Therefore, it is not surprising to see different properties between the two samples.

The large difference of $\langle \text{SFR}_{\text{IR}} / S_{850\mu\text{m}} \rangle$ between the two studies is caused by the different SEDs of the two samples. If we only consider the cold dust emission at FIR wavelengths, the mean SED of our sample is close to a modified blackbody with $\beta = 1.5$ and $T = 41.2$ K. The sources in Cowie et al. (2017), on the other hand, are generally well described by an optically thin modified blackbody ($S_\nu \propto \nu^\beta B_\nu(T)$) with $\beta = 1.25$ and $T = 43$ K. If the modified blackbody model in this work is used, the resulting dust temperature would be ~ 50 K. The main difference between these two samples is therefore in the dust temperature (or equivalently, the peak wavelength λ_{peak}), and they make more than a factor of two difference in the contribution to IR luminosity at the same redshift.

The variation of $\text{SFR}_{\text{IR}} / S_{850\mu\text{m}}$ among our sources is also a result of different dust temperatures. The three higher outliers in Figure 6 are 0416-1, 0416-3, and 1149-5, which have higher dust temperatures than the rest of the sample. In contrast, the only lower outlier in Figure 6 is 0717-1, which has the lowest dust temperature among the 10 sources that have IR SFR measurements. Note that different contributions from the emission at shorter wavelengths can be another cause of the different $\text{SFR}_{\text{IR}} / S_{850\mu\text{m}}$. This result shows that our sample of low-redshift faint SMGs has lower dust temperatures (longer λ_{peak}) than those of the bright SMGs, in agreement with other studies (e.g., Casey et al. 2012; U et al. 2012; Lee et al. 2013; Symeonidis et al. 2013).

3.4.5 Individual Sources

Here we describe some details for several galaxies that have special properties.

0416-1 and 0416-3

0416-1 is classified as an AGN in the Grism Lens-Amplified Survey from Space (GLASS; Schmidt et al. 2014; Treu et al. 2015). Because it is unclear whether the radio and UV emission is dominated by the AGN or star formation, we caution that the radio and UV

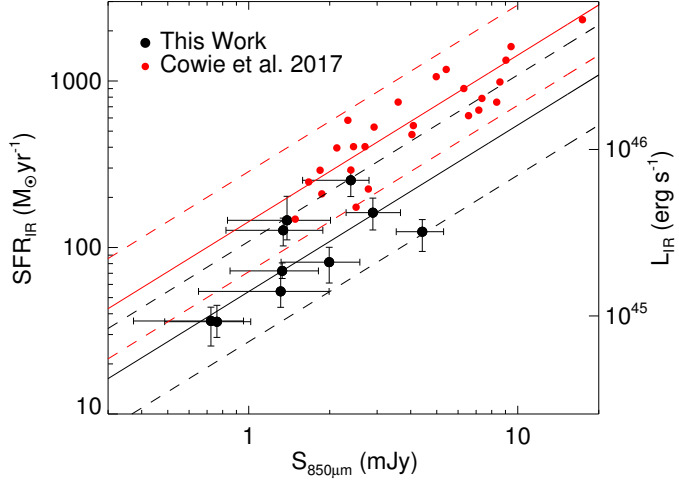


Figure 3.6: Comparison between the $850 \mu\text{m}$ flux densities and IR SFRs/luminosities for the 10 sources that have IR SFR measurements. Both of these quantities are corrected for the lensing magnifications. The black solid line is the median conversion of these 10 sources, $\text{SFR}_{\text{IR}}(M_\odot \text{ yr}^{-1}) = 54 \times S_{850\mu\text{m}} (\text{mJy})$, and the black dashed lines correspond to a multiplicative factor of two about the black solid line. The red circles are the spectroscopic sample of SMGs from Cowie et al. (2017), and the red solid line is their mean conversion, $\text{SFR}_{\text{IR}}(M_\odot \text{ yr}^{-1}) = 143 \times S_{850\mu\text{m}} (\text{mJy})$. The red dashed lines correspond to a multiplicative factor of two about the solid red line. The median redshifts of the two samples are $z = 1.24$ (this work) and $z = 2.28$ (Cowie et al.). The large difference of conversion factors between the two studies is caused by the different SEDs of the two samples.

SFRs for this source can only be considered as upper limits. The optical morphology of 0416-1 shows two peaks with a $\sim 0''.4$ offset, suggesting that it might be a merger. 0416-3 has a pair of radio counterparts that are slightly blended at 3 GHz but clearly separated at 6 GHz. These two radio sources correspond to two galaxies that have photometric redshifts of 0.99 ± 0.10 and 1.01 ± 0.10 . Both of the radio centers have $\sim 0''.5$ offsets from the optical centers. These offsets and the consistent photometric redshifts suggest that the two galaxies are an interacting pair.

0416-4 and 0717-2

0416-4 and 0717-2 are the two sources without photometric redshifts. We show the K_s -band images of these two SMGs in Figure 7. Both of these sources are outside the WFC3 coverage and not detected by *Herschel*. The *HST* magnitudes of 0416-4 are only well measured in F425W, F606W, F814W, and F850LP; a photometric redshift of $z = 1.24^{+1.99}_{-0.46}$ is reported in the CLASH catalog. The large difference between the observed brightness at optical wavelengths and K_s band for this source suggests it is likely at high redshift. We obtained a redshift estimate of $z = 2.7^{+2.7}_{-2.2}$ based on the 450 μm -to-850 μm flux ratio. 0717-2 is completely undetected in the *HST* images and also very faint in the Keck/MOSFIRE K_s -band image. This source would be an example of faint SMGs that are not included in the UV star formation history. Our redshift estimate for this source based on the 450 μm -to-850 μm flux ratio is $z = 4.5^{+2.3}_{-1.3}$.

0717-1

The radio position of 0717-1 is $\sim 1''.5$ east from the center of a spiral galaxy at $z = 1.14$. A close-up *HST*/ACS image for this source is shown in Figure 8. This source is not within the WFC3 coverage. We can see faint and red structures at the radio position. It is not clear whether these structures are from a background lensed galaxy or are related to the spiral galaxy. We assumed the case of being related to the spiral galaxy to derive the properties of this SMG. In this case, the red structures might be the core and tidal tails of a smaller

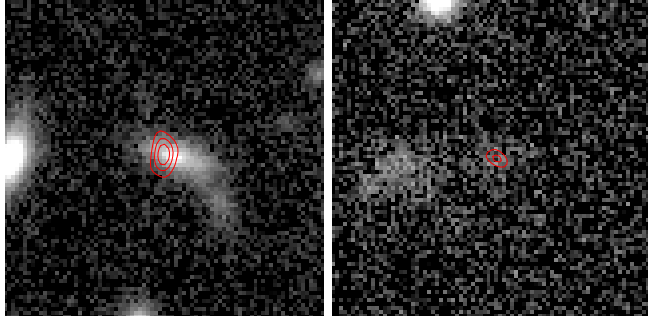


Figure 3.7: K_s -band images (Brammer et al. 2016) of 0416-4 (left) and 0717-2 (right) centered at the 3 GHz positions. The red contours are $(3.0, 6.0, 9.0)\times\sigma$ (left) and $(3.0, 5.0)\times\sigma$ (right) isophotes of the 3 GHz sources, where $\sigma \sim 1.0 \mu\text{Jy beam}^{-1}$ for both sources. The image size is $8'' \times 8''$

disrupted galaxy that is being merged into the larger spiral galaxy. Note that if this SMG is actually a background source at a higher redshift, the derived SFRs and dust temperature would all be higher.

3.5 Detectability of the Submillimeter sources

3.5.1 Bias and Redshift Distribution

In the three Frontier Fields, there are 44 SCUBA-2 850 μm sources within the *HST* coverage, and we only found 15 radio counterparts to 14 of them. 13 of these 14 identified sources are detected in the optical images. All of the sources are detected in K_s band, 3.6 μm , and 4.5 μm . 11 are at $z < 2$, and the median redshift of the entire sample is $z = 1.28^{+0.07}_{-0.09}$ (0416-3 is counted as one source at $z = 1.00$). This is much lower than the redshift distribution of the classical SMGs, which are typically found to be at $z = 2 - 3$ (e.g., Wardlow et al. 2011; Smolčić et al. 2012; Casey et al. 2013; Weiß et al. 2013; Simpson et al. 2014; Koprowski et al. 2016). The redshift distribution of our sample, which is lower than the classical SMGs, and the fact that we still miss about two-thirds of the SMGs in our radio images are caused by the bias of the radio identification technique. However, we note that some studies have suggested a “cosmic downsizing” (Cowie et al. 1996) of SMG luminosities (e.g., Heavens



Figure 3.8: Close-up *HST*/ACS false-color (F435W, F606W and F814W) image of 0717-1 centered at the 3 GHz position. The green contours are $(3.0, 4.5, 6.0)\times\sigma$ isophotes of the 3 GHz source, where $\sigma \sim 0.93 \mu\text{Jy beam}^{-1}$. The image size is $6'' \times 6''$

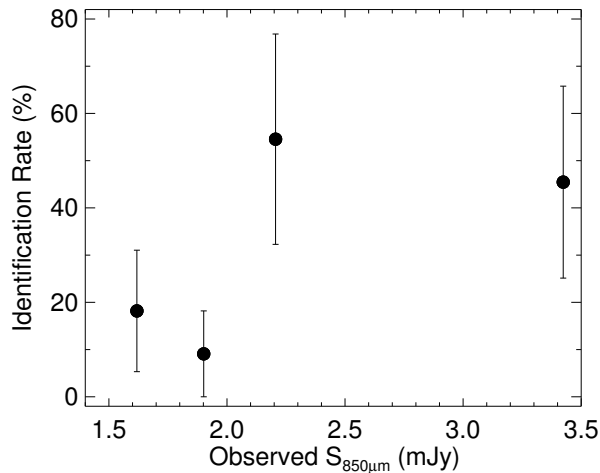


Figure 3.9: Counterpart identification rate as a function of observed (not de-lensed) 850 μm flux density for the 44 SCUBA-2 sources within the *HST* coverage. The flux range is $\sim 1.4 - 5.7 \text{ mJy}$. Each bin includes 11 sources and is plotted at the mean flux density. The errors are based on Poisson statistics.

et al. 2004; Bundy et al. 2006; Franceschini et al. 2006; Dye et al. 2008; Mobasher et al. 2009; Magliocchetti et al. 2011; Hsu et al. 2016; Cowie et al. 2017). Therefore, fainter SMGs might indeed have a lower redshift distribution.

We show the counterpart identification rate as a function of observed 850 μm flux density in Figure 9. As expected, the identification rate is lower at fainter flux bins. Also, at the brightest flux bin (~ 3.4 mJy), 55% of the sources are still not identified. Those sources without radio counterparts are likely at higher redshifts. To estimate the depth of our 3 GHz survey in terms of detecting faint SMGs, we consider a source with a specific observed 850 μm flux density. Assuming that the UV SFR is negligible and $\text{SFR}_{\text{radio}} \sim \text{SFR}_{\text{IR}}$, we can use equation (1) and our median $S_{850\mu\text{m}} - \text{SFR}_{\text{IR}}$ conversion in Section 3.4.4 to obtain the radio power L_ν at any rest-frame frequency. We can then compute the observed-frame 3 GHz flux density of this source as a function of redshift, as shown in Figure 10. This shows that, with our 5σ detection limit of $\sim 5 \mu\text{Jy beam}^{-1}$ at 3 GHz, we can only detect sources with observed $S_{850\mu\text{m}} = 2 \text{ mJy}$ out to $z \sim 1.9$. A higher $\text{SFR}_{\text{IR}}/S_{850\mu\text{m}}$ would lead to a higher redshift limit, which should be the case for the three sources at $z > 2$, 0416-1, 0416-4, and 0717-2. The value of $\text{SFR}_{\text{IR}}/S_{850\mu\text{m}}$ for 0416-1 is 106. For 0416-4 and 0717-2, $\text{SFR}_{\text{IR}}/S_{850\mu\text{m}}$ would be > 200 if their IR SFRs agree with their radio SFRs.

We can also estimate a lower limit of the median redshift of all the 44 SCUBA-2 sources. Assuming all of the other 30 radio-faint SMGs are not blended multiples and they all have $\text{SFR}_{\text{IR}}/S_{850\mu\text{m}} = 54$, we can compute the lower redshift limit for each of these sources to be detected by our 3 GHz images. Along with the 14 SMGs we already identified, the median redshift of the entire sample is at $z > 1.9$. In reality, some of these 30 sources would split into multiples, making the median redshift lower. Since a lower limit rather than an upper limit of the median redshift is estimated, it is not clear whether the redshift distribution of these cluster-lensed faint SMGs is indeed lower than those of the brighter samples. In addition, our estimated median redshift depends on the value of $\text{SFR}_{\text{IR}}/S_{850\mu\text{m}}$. Because $\text{SFR}_{\text{IR}}/S_{850\mu\text{m}}$ correlates with dust temperature (peak wavelength), the detectability of a SMG at 3 GHz is determined by both the dust temperature and the redshift. Therefore, future

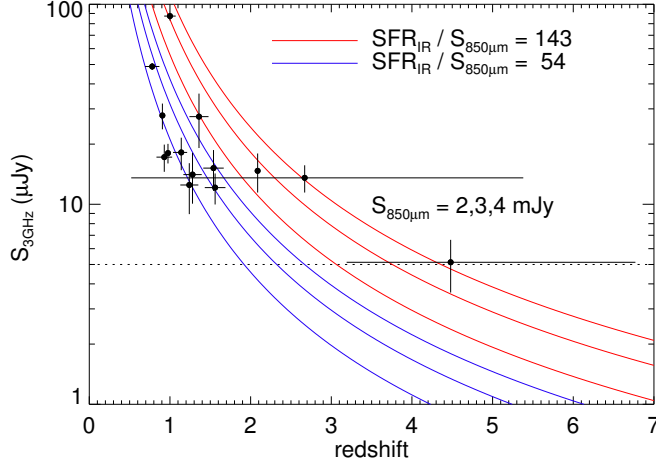


Figure 3.10: Expected observed (not de-lensed) 3 GHz flux density as a function of redshift with different observed (not de-lensed) 850 μm flux densities based on the $S_{850\mu\text{m}}\text{-SFR}_{\text{IR}}$ conversions of this work (blue) and Cowie et al. (red; 2017). For each conversion, we plot the expected relations for $S_{850\mu\text{m}} = 2, 3$, and 4 mJy (bottom to top). The horizontal dashed line corresponds to our detection limit of $\sim 5 \mu\text{Jy}$. Our sample of 14 SMGs are overplotted as black circles. We can only detect sources with observed $S_{850\mu\text{m}} = 2 \text{ mJy}$ out to $z \sim 1.9$ if $\text{SFR}_{\text{IR}}/S_{850\mu\text{m}} = 54$.

submillimeter interferometry is required to identify the multi-wavelength counterparts to the SCUBA-2 sources without radio counterparts, breaking the degeneracy of redshift and dust temperature distributions.

3.5.2 Optical-near-infrared Colors

Several previous studies have shown that optical-near-infrared colors such as $i - K$, $J - K$, and $K - [4.5]$ can effectively select high-redshift, dusty galaxies (e.g., Smail et al. 2002; Dannerbauer et al. 2004; Frayer et al. 2004; Caputi et al. 2012; Wang et al. 2012). Cowie et al. (2017) showed that among their 22 radio sources that are selected by $K - [4.5] > 1.6$ (KIERO; Wang et al. 2012), 20 have submillimeter detections at the $> 3\sigma$ level. Chen et al. (2016) proposed a triple color cut (OIRTC) of $z - K > 1.1$ and $K - [3.6] > 1.25$ and $[3.6] - [4.5] > 0.22$, which successfully selects sources from their ALMA training sample with an accuracy of 87% and a completeness of 52%.

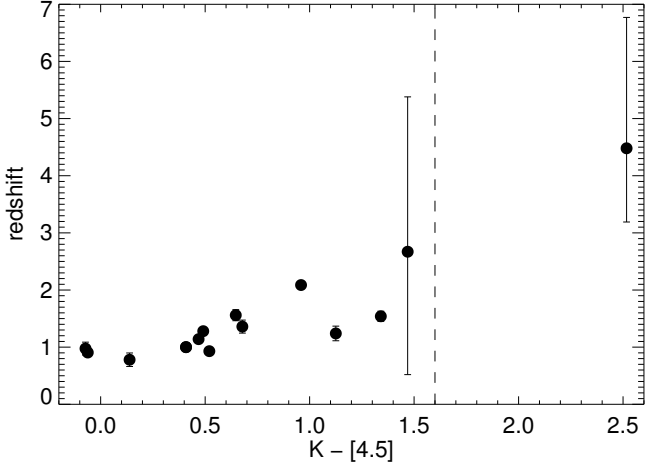


Figure 3.11: $K - [4.5]$ color (Wang et al. 2012) versus redshift for the 14 radio-identified SMGs. 0717-2 (the data point on the right) is the only source among our 14 sources that can be selected by $K - [4.5] > 1.6$ (dashed line).

We test both the KIERO and OIRTC techniques on our sample of radio-identified SMGs. Interestingly, only 0717-2, the source without an optical counterpart, can be selected by these two methods. In Figure 11, we can see a correlation between $K - [4.5]$ color and redshift. Similar trends exist for $z - K$, $K - [3.6]$ or $[3.6] - [4.5]$ as well. This suggests that both of these color cuts pick out high-redshift red galaxies. As a result, they miss the galaxies in our low-redshift sample.

3.6 Summary

We cross-match our deep SCUBA-2 survey with VLA 3 and 6 GHz images for three *HST* Frontier Fields, MACS J0416.1-2403, MACS J0717.5+3745, and MACS J1149.5+2223. Within the *HST* coverage, 14 out of 44 SCUBA-2 850 μ m sources have 5σ detected 3 GHz counterparts. A close pair of radio counterparts are identified in one of the SCUBA-2 sources, so a total of 15 radio sources are detected. Only five of the SCUBA-2 sources (six of the radio sources) are detected at 6 GHz above a 5σ level. The 850 μ m flux densities of these sources span from 0.7 to 4.4 mJy after correcting for lensing amplification. We

measure the dust temperatures, IR luminosities, and IR SFRs with our SCUBA-2 450 and 850 μm flux densities, the *Herschel* flux densities from Rawle et al. (2016), and the ALMA measurements at 1.1 mm from González-López et al. (2017). Radio and extinction-uncorrected UV SFRs are also computed based on our VLA imaging and the optical SEDs measured from the *HST* images. The radio SFRs well agree with the UV+IR SFRs.

These 14 faint SMGs are quite different from the classical, bright SMGs. First of all, the median redshift of our sample is $z = 1.28^{+0.07}_{-0.09}$, which is much lower than the typical values ($z = 2 - 3$) in the literature. 13 out of the 14 sources would not be selected from the optical-near-infrared colors techniques KIERO (Wang et al. 2012) and OIRTC (Chen et al. 2016) due to their low redshifts. Secondly, we find that our sample has lower dust temperatures (longer λ_{peak}) than those of the bright SMGs. This is also confirmed by the lower values of $\text{SFR}_{\text{IR}}/S_{850\mu\text{m}}$. However, these 14 sources may not represent the general submillimeter population at the same flux range, given that the SCUBA-2 sources without radio counterparts are likely at higher redshifts. Future submillimeter interferometry is required to identify the multi-wavelength counterparts to these radio-faint sources, creating an unbiased sample of faint SMGs for more statistical studies.

References

- Balestra, I., Mercurio, A., Sartoris, B., Girardi, M., Grillo, C., Nonino, M., Rosati, P., Biviano, A., Ettori, S., Forman, W., Jones, C., Koekemoer, A., Medezinski, E., Merten, J., Ogrean, G. A., Tozzi, P., Umetsu, K., Vanzella, E., van Weeren, R. J., Zitrin, A., Annunziatella, M., Caminha, G. B., Broadhurst, T., Coe, D., Donahue, M., Fritz, A., Frye, B., Kelson, D., Lombardi, M., Maier, C., Meneghetti, M., Monna, A., Postman, M., Scudeggio, M., Seitz, S., & Ziegler, B. 2016, ApJS, 224, 33
- Barger, A. J., Cowie, L. L., Chen, C.-C., Owen, F. N., Wang, W.-H., Casey, C. M., Lee, N., Sanders, D. B., & Williams, J. P. 2014, ApJ, 784, 9
- Barger, A. J., Wang, W.-H., Cowie, L. L., Owen, F. N., Chen, C.-C., & Williams, J. P. 2012, ApJ, 761, 89
- Benítez, N. 2000, ApJ, 536, 571
- Benítez, N., Ford, H., Bouwens, R., Menanteau, F., Blakeslee, J., Gronwall, C., Illingworth, G., Meurer, G., Broadhurst, T. J., Clampin, M., Franx, M., Hartig, G. F., Magee, D., Sirianni, M., Ardila, D. R., Bartko, F., Brown, R. A., Burrows, C. J., Cheng, E. S., Cross, N. J. G., Feldman, P. D., Golimowski, D. A., Infante, L., Kimble, R. A., Krist, J. E., Lesser, M. P., Levay, Z., Martel, A. R., Miley, G. K., Postman, M., Rosati, P., Sparks, W. B., Tran, H. D., Tsvetanov, Z. I., White, R. L., & Zheng, W. 2004, ApJS, 150, 1
- Bertin, E. & Arnouts, S. 1996, A&AS, 117, 393

- Blain, A. W. & Longair, M. S. 1993, MNRAS, 264, 509
- Blain, A. W., Smail, I., Ivison, R. J., Kneib, J.-P., & Frayer, D. T. 2002, Phys. Rep., 369, 111
- Bradač, M., Schneider, P., Lombardi, M., & Erben, T. 2005, A&A, 437, 39
- Bradač, M., Treu, T., Applegate, D., Gonzalez, A. H., Clowe, D., Forman, W., Jones, C., Marshall, P., Schneider, P., & Zaritsky, D. 2009, ApJ, 706, 1201
- Brammer, G. B., Marchesini, D., Labbé, I., Spitler, L., Lange-Vagle, D., Barker, E. A., Tanaka, M., Fontana, A., Galametz, A., Ferré-Mateu, A., Kodama, T., Lundgren, B., Martis, N., Muzzin, A., Stefanon, M., Toft, S., van der Wel, A., Vulcani, B., & Whitaker, K. E. 2016, ApJS, 226, 6
- Bundy, K., Ellis, R. S., Conselice, C. J., Taylor, J. E., Cooper, M. C., Willmer, C. N. A., Weiner, B. J., Coil, A. L., Noeske, K. G., & Eisenhardt, P. R. M. 2006, ApJ, 651, 120
- Bussmann, R. S., Riechers, D., Fialkov, A., Scudder, J., Hayward, C. C., Cowley, W. I., Bock, J., Calanog, J., Chapman, S. C., Cooray, A., De Bernardis, F., Farrah, D., Fu, H., Gavazzi, R., Hopwood, R., Ivison, R. J., Jarvis, M., Lacey, C., Loeb, A., Oliver, S. J., Pérez-Fournon, I., Rigopoulou, D., Roseboom, I. G., Scott, D., Smith, A. J., Vieira, J. D., Wang, L., & Wardlow, J. 2015, ApJ, 812, 43
- Caputi, K. I., Dunlop, J. S., McLure, R. J., Huang, J.-S., Fazio, G. G., Ashby, M. L. N., Castellano, M., Fontana, A., Cirasuolo, M., Almaini, O., Bell, E. F., Dickinson, M., Donley, J. L., Faber, S. M., Ferguson, H. C., Giavalisco, M., Grogin, N. A., Kocevski, D. D., Koekemoer, A. M., Koo, D. C., Lai, K., Newman, J. A., & Somerville, R. S. 2012, ApJ, 750, L20
- Casey, C. M., Berta, S., Béthermin, M., Bock, J., Bridge, C., Burgarella, D., Chapin, E., Chapman, S. C., Clements, D. L., Conley, A., Conselice, C. J., Cooray, A., Farrah, D., Hatziminaoglou, E., Ivison, R. J., le Floc'h, E., Lutz, D., Magdis, G., Magnelli, B., Oliver,

- S. J., Page, M. J., Pozzi, F., Rigopoulou, D., Riguccini, L., Roseboom, I. G., Sanders, D. B., Scott, D., Seymour, N., Valtchanov, I., Vieira, J. D., Viero, M., & Wardlow, J. 2012, ApJ, 761, 139
- Casey, C. M., Chen, C.-C., Cowie, L., Barger, A., Capak, P., Ilbert, O., Koss, M., Lee, N., Le Floc'h, E., Sanders, D. B., & Williams, J. P. 2013, MNRAS, 436, 1919
- Chapin, E. L., Berry, D. S., Gibb, A. G., Jenness, T., Scott, D., Tilanus, R. P. J., Economou, F., & Holland, W. S. 2013, MNRAS, 430, 2545
- Chapman, S. C., Blain, A. W., Ivison, R. J., & Smail, I. R. 2003, Nature, 422, 695
- Chapman, S. C., Blain, A. W., Smail, I., & Ivison, R. J. 2005, ApJ, 622, 772
- Chen, C.-C., Cowie, L. L., Barger, A. J., Casey, C. M., Lee, N., Sanders, D. B., Wang, W.-H., & Williams, J. P. 2013a, ApJ, 762, 81
- . 2013b, ApJ, 776, 131
- Chen, C.-C., Smail, I., Ivison, R. J., Arumugam, V., Almaini, O., Conselice, C. J., Geach, J. E., Hartley, W. G., Ma, C.-J., Mortlock, A., Simpson, C., Simpson, J. M., Swinbank, A. M., Artxaga, I., Blain, A., Chapman, S. C., Dunlop, J. S., Farrah, D., Halpern, M., Michałowski, M. J., van der Werf, P., Wilkinson, A., & Zavala, J. A. 2016, ApJ, 820, 82
- Coe, D., Benítez, N., Sánchez, S. F., Jee, M., Bouwens, R., & Ford, H. 2006, AJ, 132, 926
- Coe, D., Bradley, L., & Zitrin, A. 2015, ApJ, 800, 84
- Condon, J. J. 1974, ApJ, 188, 279
- . 1992, ARA&A, 30, 575
- Cowie, L. L., Barger, A. J., Hsu, L.-Y., Chen, C.-C., Owen, F. N., & Wang, W.-H. 2017, ApJ, 837, 139
- Cowie, L. L., Barger, A. J., & Kneib, J.-P. 2002, AJ, 123, 2197

- Cowie, L. L., Songaila, A., Hu, E. M., & Cohen, J. G. 1996, AJ, 112, 839
- Dannerbauer, H., Lehnert, M. D., Lutz, D., Tacconi, L., Bertoldi, F., Carilli, C., Genzel, R., & Menten, K. M. 2004, ApJ, 606, 664
- Diego, J. M., Broadhurst, T., Benitez, N., Umetsu, K., Coe, D., Sendra, I., Sereno, M., Izzo, L., & Covone, G. 2015, MNRAS, 446, 683
- Diego, J. M., Protopapas, P., Sandvik, H. B., & Tegmark, M. 2005a, MNRAS, 360, 477
- Diego, J. M., Sandvik, H. B., Protopapas, P., Tegmark, M., Benitez, N., & Broadhurst, T. 2005b, MNRAS, 362, 1247
- Diego, J. M., Tegmark, M., Protopapas, P., & Sandvik, H. B. 2007, MNRAS, 375, 958
- Downes, A. J. B., Peacock, J. A., Savage, A., & Carrie, D. R. 1986, MNRAS, 218, 31
- Dye, S., Eales, S. A., Artxaga, I., Serjeant, S., Dunlop, J. S., Babbedge, T. S. R., Chapman, S. C., Cirasuolo, M., Clements, D. L., Coppin, K. E. K., Dunne, L., Egami, E., Farrah, D., Ivison, R. J., van Kampen, E., Pope, A., Priddey, R., Rieke, G. H., Schael, A. M., Scott, D., Simpson, C., Takagi, T., Takata, T., & Vaccari, M. 2008, MNRAS, 386, 1107
- Ebeling, H., Ma, C.-J., & Barrett, E. 2014, ApJS, 211, 21
- Eddington, A. S. 1913, MNRAS, 73, 359
- Franceschini, A., Rodighiero, G., Cassata, P., Berta, S., Vaccari, M., Nonino, M., Vanzella, E., Hatziminaoglou, E., Antichi, J., & Cristiani, S. 2006, A&A, 453, 397
- Frayer, D. T., Reddy, N. A., Armus, L., Blain, A. W., Scoville, N. Z., & Smail, I. 2004, AJ, 127, 728
- Fujimoto, S., Ouchi, M., Ono, Y., Shibuya, T., Ishigaki, M., Nagai, H., & Momose, R. 2016, ApJS, 222, 1

González-López, J., Bauer, F. E., Romero-Cañizales, C., Kneissl, R., Villard, E., Carvajal, R., Kim, S., Laporte, N., Anguita, T., Aravena, M., Bouwens, R. J., Bradley, L., Carrasco, M., Demarco, R., Ford, H., Ibar, E., Infante, L., Messias, H., Muñoz Arancibia, A. M., Nagar, N., Padilla, N., Treister, E., Troncoso, P., & Zitrin, A. 2017, *A&A*, 597, A41

Grillo, C., Suyu, S. H., Rosati, P., Mercurio, A., Balestra, I., Munari, E., Nonino, M., Caminha, G. B., Lombardi, M., De Lucia, G., Borgani, S., Gobat, R., Biviano, A., Girardi, M., Umetsu, K., Coe, D., Koekemoer, A. M., Postman, M., Zitrin, A., Halkola, A., Broadhurst, T., Sartoris, B., Presotto, V., Annunziatella, M., Maier, C., Fritz, A., Vanzella, E., & Frye, B. 2015, *ApJ*, 800, 38

Heavens, A., Panter, B., Jimenez, R., & Dunlop, J. 2004, *Nature*, 428, 625

Helou, G., Soifer, B. T., & Rowan-Robinson, M. 1985, *ApJ*, 298, L7

Hoag, A., Huang, K.-H., Treu, T., Bradač, M., Schmidt, K. B., Wang, X., Brammer, G. B., Broussard, A., Amorin, R., Castellano, M., Fontana, A., Merlin, E., Schrabback, T., Trenti, M., & Vulcani, B. 2016, *ApJ*, 831, 182

Hodge, J. A., Karim, A., Smail, I., Swinbank, A. M., Walter, F., Biggs, A. D., Ivison, R. J., Weiss, A., Alexander, D. M., Bertoldi, F., Brandt, W. N., Chapman, S. C., Coppin, K. E. K., Cox, P., Danielson, A. L. R., Dannerbauer, H., De Breuck, C., Decarli, R., Edge, A. C., Greve, T. R., Knudsen, K. K., Menten, K. M., Rix, H.-W., Schinnerer, E., Simpson, J. M., Wardlow, J. L., & van der Werf, P. 2013, *ApJ*, 768, 91

Hogg, D. W. 2001, *AJ*, 121, 1207

Hsu, L.-Y., Cowie, L. L., Chen, C.-C., Barger, A. J., & Wang, W.-H. 2016, *ApJ*, 829, 25

Hsu, L.-Y., Desai, V., Murphy, E. J., Cowie, L. L., Heywood, I., Momjian, E., Barger, A. J., & Smail, I. 2017, *ApJ*, 840, 29

Ibar, E., Ivison, R. J., Biggs, A. D., Lal, D. V., Best, P. N., & Green, D. A. 2009, MNRAS, 397, 281

Ivison, R. J., Alexander, D. M., Biggs, A. D., Brandt, W. N., Chapin, E. L., Coppin, K. E. K., Devlin, M. J., Dickinson, M., Dunlop, J., Dye, S., Eales, S. A., Frayer, D. T., Halpern, M., Hughes, D. H., Ibar, E., Kovács, A., Marsden, G., Moncelsi, L., Netterfield, C. B., Pascale, E., Patanchon, G., Rafferty, D. A., Rex, M., Schinnerer, E., Scott, D., Semisch, C., Smail, I., Swinbank, A. M., Truch, M. D. P., Tucker, G. S., Viero, M. P., Walter, F., Weiß, A., Wiebe, D. V., & Xue, Y. Q. 2010a, MNRAS, 402, 245

Ivison, R. J., Magnelli, B., Ibar, E., Andreani, P., Elbaz, D., Altieri, B., Amblard, A., Arumugam, V., Auld, R., Aussel, H., Babbedge, T., Berta, S., Blain, A., Bock, J., Bongiovanni, A., Boselli, A., Buat, V., Burgarella, D., Castro-Rodríguez, N., Cava, A., Cepa, J., Chanial, P., Cimatti, A., Cirasuolo, M., Clements, D. L., Conley, A., Conversi, L., Cooray, A., Daddi, E., Dominguez, H., Dowell, C. D., Dwek, E., Eales, S., Farrah, D., Förster Schreiber, N., Fox, M., Franceschini, A., Gear, W., Genzel, R., Glenn, J., Griffin, M., Gruppioni, C., Halpern, M., Hatziminaoglou, E., Isaak, K., Lagache, G., Levenson, L., Lu, N., Lutz, D., Madden, S., Maffei, B., Magdis, G., Mainetti, G., Maiolino, R., Marchetti, L., Morrison, G. E., Mortier, A. M. J., Nguyen, H. T., Nordon, R., O'Halloran, B., Oliver, S. J., Omont, A., Owen, F. N., Page, M. J., Panuzzo, P., Papageorgiou, A., Pearson, C. P., Pérez-Fournon, I., Pérez García, A. M., Poglitsch, A., Pohlen, M., Popesso, P., Pozzi, F., Rawlings, J. I., Raymond, G., Rigopoulou, D., Riguccini, L., Rizzo, D., Rodighiero, G., Roseboom, I. G., Rowan-Robinson, M., Saintonge, A., Sanchez Portal, M., Santini, P., Schulz, B., Scott, D., Seymour, N., Shao, L., Shupe, D. L., Smith, A. J., Stevens, J. A., Sturm, E., Symeonidis, M., Tacconi, L., Trichas, M., Tugwell, K. E., Vaccari, M., Valtchanov, I., Vieira, J., Vigroux, L., Wang, L., Ward, R., Wright, G., Xu, C. K., & Zemcov, M. 2010b, A&A, 518, L31

Jauzac, M., Clément, B., Limousin, M., Richard, J., Jullo, E., Ebeling, H., Atek, H., Kneib, J.-P., Knowles, K., Natarajan, P., Eckert, D., Egami, E., Massey, R., & Rexroth, M.

2014, MNRAS, 443, 1549

Jauzac, M., Jullo, E., Eckert, D., Ebeling, H., Richard, J., Limousin, M., Atek, H., Kneib, J.-P., Clément, B., Egami, E., Harvey, D., Knowles, K., Massey, R., Natarajan, P., & Rexroth, M. 2015a, MNRAS, 446, 4132

Jauzac, M., Jullo, E., Kneib, J.-P., Ebeling, H., Leauthaud, A., Ma, C.-J., Limousin, M., Massey, R., & Richard, J. 2012, MNRAS, 426, 3369

Jauzac, M., Richard, J., Jullo, E., Clément, B., Limousin, M., Kneib, J.-P., Ebeling, H., Natarajan, P., Rodney, S., Atek, H., Massey, R., Eckert, D., Egami, E., & Rexroth, M. 2015b, MNRAS, 452, 1437

Johansson, D., Sigurdarson, H., & Horellou, C. 2011, A&A, 527, A117

Johnson, T. L., Sharon, K., Bayliss, M. B., Gladders, M. D., Coe, D., & Ebeling, H. 2014, ApJ, 797, 48

Jullo, E. & Kneib, J.-P. 2009, MNRAS, 395, 1319

Jullo, E., Kneib, J.-P., Limousin, M., Elíasdóttir, Á., Marshall, P. J., & Verdugo, T. 2007, New Journal of Physics, 9, 447

Kawamata, R., Oguri, M., Ishigaki, M., Shimasaku, K., & Ouchi, M. 2016, ApJ, 819, 114

Knudsen, K. K., van der Werf, P. P., & Kneib, J.-P. 2008, MNRAS, 384, 1611

Koprowski, M., Dunlop, J. S., Michalowski, M. J., Roseboom, I., Geach, J. E., Cirasuolo, M., Artxaga, I., Bowler, R. A. A., Banerji, M., Bourne, N., Coppin, K. E. K., Chapman, S., Hughes, D. H., Jenness, T., McLure, R. J., Symeonidis, M., & van der Werf, P. 2016, MNRAS, 458, 4321

Kovács, A., Chapman, S. C., Dowell, C. D., Blain, A. W., Ivison, R. J., Smail, I., & Phillips, T. G. 2006, ApJ, 650, 592

Kroupa, P. 2001, MNRAS, 322, 231

Lee, N., Sanders, D. B., Casey, C. M., Scoville, N. Z., Hung, C.-L., Le Floc'h, E., Ilbert, O., Aussel, H., Capak, P., Kartaltepe, J. S., Roseboom, I., Salvato, M., Aravena, M., Berta, S., Bock, J., Oliver, S. J., Riguccini, L., & Symeonidis, M. 2013, ApJ, 778, 131

Liesenborgs, J., De Rijcke, S., & Dejonghe, H. 2006, MNRAS, 367, 1209

Magliocchetti, M., Santini, P., Rodighiero, G., Grazian, A., Aussel, H., Altieri, B., Andreani, P., Berta, S., Cepa, J., Castañeda, H., Cimatti, A., Daddi, E., Elbaz, D., Genzel, R., Gruppioni, C., Lutz, D., Magnelli, B., Maiolino, R., Popesso, P., Poglitsch, A., Pozzi, F., Sanchez-Portal, M., Förster Schreiber, N. M., Sturm, E., Tacconi, L., & Valtchanov, I. 2011, MNRAS, 416, 1105

Makovoz, D. & Khan, I. 2005, in Astronomical Society of the Pacific Conference Series, Vol. 347, Astronomical Data Analysis Software and Systems XIV, ed. P. Shopbell, M. Britton, & R. Ebert, 81

Makovoz, D. & Marleau, F. R. 2005, PASP, 117, 1113

Makovoz, D., Roby, T., Khan, I., & Booth, H. 2006, in Proc. SPIE, Vol. 6274, Society of Photo-Optical Instrumentation Engineers (SPIE) Conference Series, 62740C

McMullin, J. P., Waters, B., Schiebel, D., Young, W., & Golap, K. 2007, in Astronomical Society of the Pacific Conference Series, Vol. 376, Astronomical Data Analysis Software and Systems XVI, ed. R. A. Shaw, F. Hill, & D. J. Bell, 127

Merten, J., Cacciato, M., Meneghetti, M., Mignone, C., & Bartelmann, M. 2009, A&A, 500, 681

Merten, J., Coe, D., Dupke, R., Massey, R., Zitrin, A., Cypriano, E. S., Okabe, N., Frye, B., Braglia, F. G., Jiménez-Teja, Y., Benítez, N., Broadhurst, T., Rhodes, J., Meneghetti, M., Moustakas, L. A., Sodré, Jr., L., Krick, J., & Bregman, J. N. 2011, MNRAS, 417, 333

Mobasher, B., Dahlen, T., Hopkins, A., Scoville, N. Z., Capak, P., Rich, R. M., Sanders, D. B., Schinnerer, E., Ilbert, O., Salvato, M., & Sheth, K. 2009, ApJ, 690, 1074

Mohammed, I., Liesenborgs, J., Saha, P., & Williams, L. L. R. 2014, MNRAS, 439, 2651

Momjian, E., Wang, W.-H., Knudsen, K. K., Carilli, C. L., Cowie, L. L., & Barger, A. J. 2010, AJ, 139, 1622

Murphy, E. J. 2009, ApJ, 706, 482

Murphy, E. J., Bremseth, J., Mason, B. S., Condon, J. J., Schinnerer, E., Aniano, G., Armus, L., Helou, G., Turner, J. L., & Jarrett, T. H. 2012, ApJ, 761, 97

Murphy, E. J., Condon, J. J., Schinnerer, E., Kennicutt, R. C., Calzetti, D., Armus, L., Helou, G., Turner, J. L., Aniano, G., Beirão, P., Bolatto, A. D., Brandl, B. R., Croxall, K. V., Dale, D. A., Donovan Meyer, J. L., Draine, B. T., Engelbracht, C., Hunt, L. K., Hao, C.-N., Koda, J., Roussel, H., Skibba, R., & Smith, J.-D. T. 2011, ApJ, 737, 67

Offringa, A. R., McKinley, B., Hurley-Walker, N., Briggs, F. H., Wayth, R. B., Kaplan, D. L., Bell, M. E., Feng, L., Neben, A. R., Hughes, J. D., Rhee, J., Murphy, T., Bhat, N. D. R., Bernardi, G., Bowman, J. D., Cappallo, R. J., Corey, B. E., Deshpande, A. A., Emrich, D., Ewall-Wice, A., Gaensler, B. M., Goeke, R., Greenhill, L. J., Hazelton, B. J., Hindson, L., Johnston-Hollitt, M., Jacobs, D. C., Kasper, J. C., Kratzenberg, E., Lenc, E., Lonsdale, C. J., Lynch, M. J., McWhirter, S. R., Mitchell, D. A., Morales, M. F., Morgan, E., Kudryavtseva, N., Oberoi, D., Ord, S. M., Pindor, B., Procopio, P., Prabu, T., Riding, J., Roshi, D. A., Shankar, N. U., Srivani, K. S., Subrahmanyan, R., Tingay, S. J., Waterson, M., Webster, R. L., Whitney, A. R., Williams, A., & Williams, C. L. 2014, MNRAS, 444, 606

Oguri, M. 2010, PASJ, 62, 1017

- Pope, A., Scott, D., Dickinson, M., Chary, R.-R., Morrison, G., Borys, C., Sajina, A., Alexander, D. M., Daddi, E., Frayer, D., MacDonald, E., & Stern, D. 2006, MNRAS, 370, 1185
- Postman, M., Coe, D., Benítez, N., Bradley, L., Broadhurst, T., Donahue, M., Ford, H., Graur, O., Graves, G., Jouvel, S., Koekemoer, A., Lemze, D., Medezinski, E., Molino, A., Moustakas, L., Ogaz, S., Riess, A., Rodney, S., Rosati, P., Umetsu, K., Zheng, W., Zitrin, A., Bartelmann, M., Bouwens, R., Czakon, N., Golwala, S., Host, O., Infante, L., Jha, S., Jimenez-Teja, Y., Kelson, D., Lahav, O., Lazkoz, R., Maoz, D., McCully, C., Melchior, P., Meneghetti, M., Merten, J., Moustakas, J., Nonino, M., Patel, B., Regös, E., Sayers, J., Seitz, S., & Van der Wel, A. 2012, ApJS, 199, 25
- Rawle, T. D., Altieri, B., Egami, E., Pérez-González, P. G., Boone, F., Clement, B., Ivison, R. J., Richard, J., Rujopakarn, W., Valtchanov, I., Walth, G., Weiner, B., Blain, A. W., Dessauges-Zavadsky, M., Kneib, J.-P., Lutz, D., Rodighiero, G., Schaerer, D., & Smail, I. 2016, MNRAS, 459, 1626
- Richard, J., Jauzac, M., Limousin, M., Jullo, E., Clément, B., Ebeling, H., Kneib, J.-P., Atek, H., Natarajan, P., Egami, E., Livermore, R., & Bower, R. 2014, MNRAS, 444, 268
- Rieke, G. H., Alonso-Herrero, A., Weiner, B. J., Pérez-González, P. G., Blaylock, M., Donley, J. L., & Marcillac, D. 2009, ApJ, 692, 556
- Schlafly, E. F. & Finkbeiner, D. P. 2011, ApJ, 737, 103
- Schmidt, K. B., Treu, T., Brammer, G. B., Bradač, M., Wang, X., Dijkstra, M., Dressler, A., Fontana, A., Gavazzi, R., Henry, A. L., Hoag, A., Jones, T. A., Kelly, P. L., Malkan, M. A., Mason, C., Pentericci, L., Poggianti, B., Stiavelli, M., Trenti, M., von der Linden, A., & Vulcani, B. 2014, ApJ, 782, L36
- Sebesta, K., Williams, L. L. R., Mohammed, I., Saha, P., & Liesenborgs, J. 2016, MNRAS, 461, 2126

Simpson, J. M., Smail, I., Swinbank, A. M., Chapman, S. C., Geach, J. E., Ivison, R. J., Thomson, A. P., Arétxaga, I., Blain, A. W., Cowley, W. I., Chen, C.-C., Coppin, K. E. K., Dunlop, J. S., Edge, A. C., Farrah, D., Ibar, E., Karim, A., Knudsen, K. K., Meijerink, R., Michałowski, M. J., Scott, D., Spaans, M., & van der Werf, P. P. 2015, *ApJ*, 807, 128

Simpson, J. M., Swinbank, A. M., Smail, I., Alexander, D. M., Brandt, W. N., Bertoldi, F., de Breuck, C., Chapman, S. C., Coppin, K. E. K., da Cunha, E., Danielson, A. L. R., Dannerbauer, H., Greve, T. R., Hodge, J. A., Ivison, R. J., Karim, A., Knudsen, K. K., Poggianti, B. M., Schinnerer, E., Thomson, A. P., Walter, F., Wardlow, J. L., Weiß, A., & van der Werf, P. P. 2014, *ApJ*, 788, 125

Smail, I., Ivison, R. J., & Blain, A. W. 1997, *ApJ*, 490, L5

Smail, I., Ivison, R. J., Blain, A. W., & Kneib, J.-P. 2002, *MNRAS*, 331, 495

Smolčić, V., Aravena, M., Navarrete, F., Schinnerer, E., Riechers, D. A., Bertoldi, F., Feruglio, C., Finoguenov, A., Salvato, M., Sargent, M., McCracken, H. J., Albrecht, M., Karim, A., Capak, P., Carilli, C. L., Cappelluti, N., Elvis, M., Ilbert, O., Kartaltepe, J., Lilly, S., Sanders, D., Sheth, K., Scoville, N. Z., & Taniguchi, Y. 2012, *A&A*, 548, A4

Symeonidis, M., Vaccari, M., Berta, S., Page, M. J., Lutz, D., Arumugam, V., Aussel, H., Bock, J., Boselli, A., Buat, V., Capak, P. L., Clements, D. L., Conley, A., Conversi, L., Cooray, A., Dowell, C. D., Farrah, D., Franceschini, A., Giovannoli, E., Glenn, J., Griffin, M., Hatziminaoglou, E., Hwang, H.-S., Ibar, E., Ilbert, O., Ivison, R. J., Floc'h, E. L., Lilly, S., Kartaltepe, J. S., Magnelli, B., Magdis, G., Marchetti, L., Nguyen, H. T., Nordon, R., O'Halloran, B., Oliver, S. J., Omont, A., Papageorgiou, A., Patel, H., Pearson, C. P., Pérez-Fournon, I., Pohlen, M., Popesso, P., Pozzi, F., Rigopoulou, D., Riguccini, L., Rosario, D., Roseboom, I. G., Rowan-Robinson, M., Salvato, M., Schulz, B., Scott, D., Seymour, N., Shupe, D. L., Smith, A. J., Valtchanov, I., Wang, L., Xu, C. K., Zemcov, M., & Wuyts, S. 2013, *MNRAS*, 431, 2317

- Treu, T., Schmidt, K. B., Brammer, G. B., Vulcani, B., Wang, X., Bradač, M., Dijkstra, M., Dressler, A., Fontana, A., Gavazzi, R., Henry, A. L., Hoag, A., Huang, K.-H., Jones, T. A., Kelly, P. L., Malkan, M. A., Mason, C., Pentericci, L., Poggianti, B., Stiavelli, M., Trenti, M., & von der Linden, A. 2015, ApJ, 812, 114
- U, V., Sanders, D. B., Mazzarella, J. M., Evans, A. S., Howell, J. H., Surace, J. A., Armus, L., Iwasawa, K., Kim, D.-C., Casey, C. M., Vavilkin, T., Dufault, M., Larson, K. L., Barnes, J. E., Chan, B. H. P., Frayer, D. T., Haan, S., Inami, H., Ishida, C. M., Kartaltepe, J. S., Melbourne, J. L., & Petric, A. O. 2012, ApJS, 203, 9
- Wang, W.-H., Barger, A. J., & Cowie, L. L. 2012, ApJ, 744, 155
- Wang, W.-H., Cowie, L. L., Barger, A. J., & Williams, J. P. 2011, ApJ, 726, L18
- Wardlow, J. L., Smail, I., Coppin, K. E. K., Alexander, D. M., Brandt, W. N., Danielson, A. L. R., Luo, B., Swinbank, A. M., Walter, F., Weiß, A., Xue, Y. Q., Zibetti, S., Bertoldi, F., Biggs, A. D., Chapman, S. C., Dannerbauer, H., Dunlop, J. S., Gawiser, E., Ivison, R. J., Knudsen, K. K., Kovács, A., Lacey, C. G., Menten, K. M., Padilla, N., Rix, H.-W., & van der Werf, P. P. 2011, MNRAS, 415, 1479
- Watson, D., Christensen, L., Knudsen, K. K., Richard, J., Gallazzi, A., & Michałowski, M. J. 2015, Nature, 519, 327
- Weiß, A., De Breuck, C., Marrone, D. P., Vieira, J. D., Aguirre, J. E., Aird, K. A., Aravena, M., Ashby, M. L. N., Bayliss, M., Benson, B. A., Béthermin, M., Biggs, A. D., Bleem, L. E., Bock, J. J., Bothwell, M., Bradford, C. M., Brodwin, M., Carlstrom, J. E., Chang, C. L., Chapman, S. C., Crawford, T. M., Crites, A. T., de Haan, T., Dobbs, M. A., Downes, T. P., Fassnacht, C. D., George, E. M., Gladders, M. D., Gonzalez, A. H., Greve, T. R., Halverson, N. W., Hezaveh, Y. D., High, F. W., Holder, G. P., Holzapfel, W. L., Hoover, S., Hrubes, J. D., Husband, K., Keisler, R., Lee, A. T., Leitch, E. M., Lueker, M., Luong-Van, D., Malkan, M., McIntyre, V., McMahon, J. J., Mehl, J., Menten, K. M., Meyer, S. S., Murphy, E. J., Padin, S., Plagge, T., Reichardt, C. L., Rest, A.,

Rosenman, M., Ruel, J., Ruhl, J. E., Schaffer, K. K., Shirokoff, E., Spilker, J. S., Stalder, B., Staniszewski, Z., Stark, A. A., Story, K., Vanderlinde, K., Welikala, N., & Williamson, R. 2013, ApJ, 767, 88

Zitrin, A., Broadhurst, T., Umetsu, K., Coe, D., Benítez, N., Ascaso, B., Bradley, L., Ford, H., Jee, J., Medezinski, E., Rephaeli, Y., & Zheng, W. 2009, MNRAS, 396, 1985

Zitrin, A., Meneghetti, M., Umetsu, K., Broadhurst, T., Bartelmann, M., Bouwens, R., Bradley, L., Carrasco, M., Coe, D., Ford, H., Kelson, D., Koekemoer, A. M., Medezinski, E., Moustakas, J., Moustakas, L. A., Nonino, M., Postman, M., Rosati, P., Seidel, G., Seitz, S., Sendra, I., Shu, X., Vega, J., & Zheng, W. 2013, ApJ, 762, L30

Chapter 4

SMA-detected Faint Submillimeter Galaxies

4.1 Introduction

Bright SMGs from confusion-limited surveys and the extinction-corrected UV population are essentially disjoint (Barger et al. 2014; Cowie et al. 2017), so their contributions to the cosmic star formation history must be added. Fainter SMGs, on the other hand, are more common objects that contribute the majority of the EBL (e.g., Chen et al. 2013; Hsu et al. 2016; Zavala et al. 2017) and therefore most of the dusty star formation. However, some of these faint SMGs could also be selected in the UV samples. In order to combine the UV- and FIR-inferred star formation history precisely, it is critical to obtain a complete census of faint SMGs that have SFRs comparable to those of the UV population. Such a sample bridges the SFR gap between the two populations and allows us to determine the critical SFR below which UV-selected galaxies alone account for all the star formation. In addition, bright SMGs are often shown to have complex morphologies and are suggested to be major mergers (e.g., Chen et al. 2015; Hodge et al. 2016), though some may be massive disks fed by cold flow (e.g., Hodge et al. 2012). Follow-up studies of fainter sources will allow us to determine if there is any physical change in the star formation mechanism with decreasing luminosity/SFR.

In Chapter 3 (Hsu et al. 2017), we used 3 GHz observations with the VLA to identify the multi-wavelength counterparts to our SCUBA-2 sources in three Frontier Fields, relying on

the FIR-radio correlation for starburst galaxies (Helou et al. 1985; Condon 1992). However, the disadvantage of radio interferometry is that the observed flux densities do not benefit from a negative K -correction, making it difficult to detect SMGs at the highest redshifts. We have shown that about two-thirds of the sources within the *HST*/ACS footprints are not detected in the deep VLA images. Submillimeter interferometry is required to observe such radio-faint sources and produce an unbiased sample of faint SMGs.

In this chapter, we present our SMA follow-up observations of six intrinsically faint SCUBA-2 sources discovered in the fields of A1689, A2390, A370, MACS J0717.5+3745, and MACS J1423.8+2404 (hereafter, MACSJ0717 and MACSJ1423). The observations and data reduction are described in Section 4.2. We present our results in Section 4.3 and discuss their implications in Section 4.4. Section 4.5 summarizes this chapter. We assume the concordance Λ CDM cosmology with $H_0 = 70 \text{ km s}^{-1} \text{ Mpc}^{-1}$, $\Omega_M = 0.3$, and $\Omega_\Lambda = 0.7$.

4.2 Data

4.2.1 SCUBA-2 Observations

The targets for the SMA observations were selected from our SCUBA-2 lensing cluster surveys, based on the 850 μm images we had at different times. However, the SCUBA-2 measurements we present in this work (Section 4.3) are based on all the 850 μm data taken with the CV DAISY scan pattern between February 2012 and March 2017. We summarize these observations in Table 4.1. Please refer to Chapters 2 (Hsu et al. 2016) and 3 (Hsu et al. 2017) for details on the data reduction and source extraction procedures. In order to correct for the effects of Eddington bias (Eddington 1913) and confusion noise (Condon 1974), we deboosted the SCUBA-2 flux densities using the method described in Chapter 3.

4.2.2 SMA Observations

We carried out SMA observations from 2014 to 2016 for six SCUBA-2 850 μm sources in the five cluster fields. The local oscillator frequency was set at 343 GHz, or 870 μm .

Table 4.1: Summary of JCMT/SCUBA-2 Observations

Field	R.A.	Decl.	Redshift	Weather ^a	Exposure (hr)	σ_{850} ^b (mJy beam ⁻¹)
A370	02 39 53.1	-01 34 35.0	0.375	1+2+3	28.5+1.5+7.0	0.38
MACSJ0717	07 17 34.0	37 44 49.0	0.545	1+2+3	32.2+10.5+1.5	0.31
A1689	13 11 29.0	-01 20 17.0	0.184	1+2	22.4+1.9	0.39
MACSJ1423	14 23 48.3	24 04 47.0	0.545	1+2+3	36.5+20.5+1.6	0.28
A2390	21 53 36.8	17 41 44.2	0.231	1+2+3	17.4+36.0+9.0	0.32

^aData were taken in band 1 ($\tau_{225\text{GHz}} < 0.05$), band 2 ($0.05 < \tau_{225\text{GHz}} < 0.08$), or good band 3 ($0.08 < \tau_{225\text{GHz}} < 0.1$) conditions.

^bCentral 1σ sensitivity of the 850 μm map. These are the statistical/instrumental noise values directly from the reduced rms maps.

The new SWARM (SMA Wideband Astronomical ROACH2 Machine) correlator and dual receiver mode became available during the course of our program, which greatly improved the continuum sensitivity. We summarize these observations in Table 4.2.

We used the SMA data reduction package MIR to calibrate our data. The visibilities were first weighted in inverse proportion to the square of the system temperatures. The continuum data were generated by averaging all the spectral channels after performing passband phase calibration. We used the gain calibrators to correct for the variations of phase/amplitude in time, and then we performed the flux calibration to set the absolute flux level. For the track executed in dual receiver mode (20161017 in Table 4.2), we ran all the calibrations for the two receivers separately.

The visibilities from all the available tracks for each source were combined and imaged using the interferometry data reduction package MIRIAD (Sault et al. 1995). We made the dirty maps and the synthesized dirty beam images in a $0.^{\circ}2$ (compact configuration) or $0.^{\circ}1$ (extended configuration) grid using the routine INVERT with natural weighting on the baselines. We also performed multi-frequency synthesis, which gives better coverage in the frequency-dependent uv coordinate. The CLEAN routine was used to deconvolve the dirty map. We CLEANed the images around detected sources to approximately 1.5σ to remove the effects of sidelobes. The resulting source fluxes are not sensitive to the depth to which we chose to clean. Primary beam correction was applied to the images by dividing the CLEANed fluxes by the off-axis gain. In Table 4.3, we summarize the synthesized beams and central sensitivities of the final images.

4.2.3 HST and Spitzer Images

For the Frontier Field clusters, we retrieved the Advanced Camera for Surveys (ACS) and Wide-Field Camera 3 (WFC3) images from the *HST* Frontier Field archive¹. The images for MACSJ1423 are taken from the Cluster Lensing And Supernova survey with Hubble

¹<https://archive.stsci.edu/pub/hlsp/frontier/>

Table 4.2: Summary of SMA Observations

ID	Field	Configuration	Track Dates	Receiver(s)	Bandwidth ^a	Passband Calibrator	Gain Calibrator(s)	Flux Calibrator(s)
SMA-1	A370	extended	20151001	345	8 GHz	3c454.3	0224+069, 0309+104	Neptune
			20161017	345, 400 ^b	12 GHz	3c454.3	0224+069, 0309+104	Uranus
SMA-2	MACSJ0717	compact	20160102	345	8 GHz	3c84	0818+423, 0927+390	Neptune
SMA-3	A1689	compact	20160104	345	12 GHz	3c279	1337-129, 3c279	Callisto
SMA-4	MACSJ1423	compact	20160301	345	8 GHz	3c273	1504+104	Ganymede
SMA-5	A2390	compact	20140625	345	8 GHz	3c273	1357+193, 1415+133	Ganymede
			20140626	345	8 GHz	3c279	2148+069, 3c454.3	Titan, Neptune
			20141024	345	8 GHz	3c454.3	2148+069, 3c454.3	Neptune
			20141029	345	8 GHz	3c454.3	2148+069, 3c454.3	Neptune
			20141030	345	8 GHz	3c454.3	2148+069, 3c454.3	Neptune
SMA-6	A2390	compact	20140629	345	8 GHz	3c279	2148+069, 3c454.3	Titan, Neptune
			20140630	345	8 GHz	3c279	2148+069, 3c454.3	Titan, Neptune
			20140702	345	8 GHz	3c454.3	2148+069, 3c454.3	Titan, Neptune
			20141024	345	8 GHz	3c454.3	2148+069, 3c454.3	Neptune
			20141029	345	8 GHz	3c454.3	2148+069, 3c454.3	Neptune

^aTotal bandwidth combining upper and lower sidebands. When the SWARM correlator operated, an additional 2 GHz was available for each sideband.

^bDual receiver mode. The two receivers cover the same spectral range.

Table 4.3: Synthesized Beam Sizes and Position Angles As Well As Central Sensitivities of the SMA Images

ID	Beam FWHM (" × ")	Beam P.A. (deg)	σ (mJy beam $^{-1}$)
SMA-1	0.86×0.60	85.0	0.44
SMA-2	2.20×1.88	-64.6	0.38
SMA-3	2.03×1.92	-0.9	0.50
SMA-4	2.15×1.78	-86.3	0.48
SMA-5	2.28×1.60	-73.9	0.55
SMA-6	2.21×1.53	-83.0	0.43

(CLASH; Postman et al. 2012) archive². For A1689 and A2390, we used SWARP (Bertin et al. 2002) to combine individual archival images³ for each passband.

We also retrieved the *Spitzer* Frontier Fields data⁴, as well as the “Super Mosaics” and their source catalogs for the other three clusters from the *Spitzer* archive. These include data from the Infrared Array Camera (IRAC) at 3.6, 4.5, 5.8, and 8 μm , and the Multiband Imaging Photometer of Spitzer (MIPS) at 24 μm .

4.2.4 K_s -band Images

We carried out K_s -band observations of A1689 and A2390 (PI: Hsu; PID: 15AH83) with WIRCam on the Canada–France–Hawaii Telescope (CFHT) in 2015. Along with the archival data of A2390 (PI: Umetsu; PID: 07AT98), the total integration times are 2800 and 3515 seconds for A1689 and A2390, respectively. We reduced and combined these images using Imaging and Mosaicking PipeLinE (SIMPLE; Wang et al. 2010), an IDL-based package for galactic/extragalactic imaging with CFHT/WIRCam or MOIRCS on the Subaru Telescope.

SIMPLE performs flat fielding, background subtraction, distortion correction, absolute astrometry, photometric calibration, wide-field mosaicking, cosmic ray removal, and image

²<https://archive.stsci.edu/prepds/clash/>

³PI (PIDs): Blakeslee (11710), Ellis (10504), Ford (9289, 11802), Rigby (11678), Siana (12201, 12931)

⁴<http://irsa.ipac.caltech.edu/data/SPITZER/Frontier/>

weighting. Absolute astrometry was obtained by comparing the image with the source catalogs of the Sloan Digital Sky Survey (SDSS). The photometry was calibrated with bright stars in the source catalogs of the Two Micron All Sky Survey (2MASS). We reduced the data chip by chip before mosaicking, and the pixel scale of the images is $0.^{\prime\prime}3$.

We also retrieved the K_s -band images of the Frontier Fields A370 (VLT/HAWK-I), MACSJ0717 (Keck/MOSFIRE), and MACSJ1423 (CFHT/WIRCam) from Brammer et al. (2016) and the CLASH archive, respectively.

4.2.5 VLA Images

We make use of the 3 GHz image of MACSJ0717 taken with the VLA from Chapter 3 (Hsu et al. 2017). For A370 and A2390, we obtained the VLA 1.4 GHz images from Wold et al. (2012). The A370 (A2390) image has a synthesized beam of $\sim 1.^{\prime\prime}7$ ($1.^{\prime\prime}4$) and a noise level of ~ 5.7 (5.6) μ Jy near the cluster center.

4.3 Results

4.3.1 SMA Detections and Multi-wavelength Counterparts

We detected eight sources above a 4σ level in the six SMA images, where SMA-2 and SMA-3 both split into doublets. The positions and flux densities of the original SCUBA-2 sources and these SMA detections are summarized in Table 4.4. In Figure 4.1, we show the postage stamp images centered at the original SCUBA-2 positions. Although there is inconsistency between the SCUBA-2 and SMA flux densities for SMA-1 and SMA-6, the difference can be caused by multiple faint sources that are below our detection limit. This is clear for SMA-6, where we can see some emission with $S/N > 3$ coming from an optically detected galaxy (possibly a pair of interacting galaxies).

Three (SMA-1, SMA-2-1, and SMA-5) of the eight SMA sources are detected in the optical or NIR. Note that for SMA-4, there is one elliptical galaxy that has a $< 1''$ offset from the SMA position. Based on the photometric catalog from CLASH, this source is a

Table 4.4: Positions and Flux Densities of the SCUBA-2 Sources and Their SMA Detections

ID	SCUBA-2				SMA			
	R.A.	Decl.	S_{850}	(mJy)	R.A.	Decl.	S_{870}	(mJy)
SMA-1	02 39 57.57	-01 34 53.0	4.71 ± 0.73		02 39 57.58	-01 34 53.6	2.14 ± 0.44	
SMA-2	07 17 38.22	37 46 15.0	2.97 ± 0.63	
SMA-2-1		07 17 38.12	37 46 16.6	1.78 ± 0.39	
SMA-2-2		07 17 37.90	37 46 15.0	2.15 ± 0.40	
SMA-3	13 11 23.93	-01 20 46.4	4.26 ± 0.77	
SMA-3-1		13 11 23.64	-01 20 47.2	2.14 ± 0.53	
SMA-3-2		13 11 24.22	-01 20 52.4	2.49 ± 0.57	
SMA-4	14 23 48.14	24 04 11.1	2.70 ± 0.51		14 23 48.51	24 04 14.1	2.64 ± 0.54	
SMA-5	21 53 34.63	17 40 31.2	3.39 ± 0.64		21 53 34.50	17 40 29.2	2.49 ± 0.56	
SMA-6	21 53 38.69	17 42 17.2	4.01 ± 0.66		21 53 38.86	17 42 17.6	1.97 ± 0.43	

cluster member galaxy at $z \sim 0.5$. Thus, it is unlikely to be the counterpart to the SMG. There is also a small offset between the peaks of the submillimeter and optical emission for SMA-5. However, the offset becomes smaller in the K_s -band image. We suggest that the optical/NIR source is the correct counterpart to the SMG, and the offset is due to different regions of unobscured and dust-obscured star formation, which is very typical for SMGs.

As we will discuss in Section 4.4, we use K_s -band photometry to quantify the NIR emission, given that K_s -band images are available for all of our sources. In addition, they have better spatial resolution than the *Spitzer* images. We used SExtractor (Bertin & Arnouts 1996) to measure AUTO magnitudes of the SMA sources detected at K_s band. The deblending parameters DEBLEND_NTHRESH and DEBLEND_MINCONT were set to be 32 and 0.005, respectively. For the sources that are not detected in the K_s -band images, we measured their 3σ limiting magnitudes in a $1''$ -radius aperture.

4.3.2 Redshift Estimates

We measured the photometric redshifts of SMA-1 and SMA-5 using the BPZ code (Bayesian photometric redshift estimation; Benítez 2000) and the Bruzual & Charlot (2003) models with the Chabrier (2003) initial mass function. SMA-1 is covered by *HST* observations at

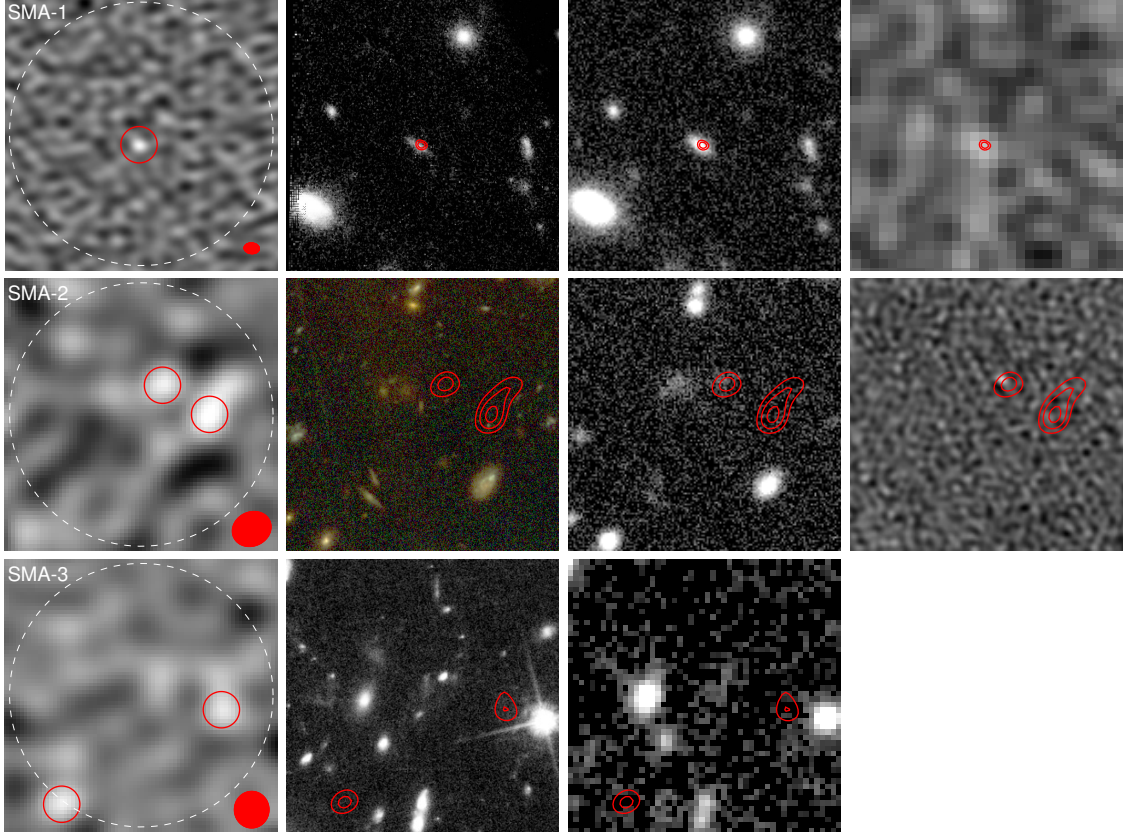


Figure 4.1: Postage stamp images for the SMA detections centered at the SCUBA-2 850 μm positions. From left to right are SMA 870 μm , *HST* (from top to bottom: F160W, F435W-F606W-F814W false color, F814W), K_s -band (from top to bottom: VLT/HAWK-I, Keck/MOSFIRE, and CFHT/WIRCam), and VLA (SMA-1: 1.4 GHz; SMA-2: 3 GHz) images. The image size is $15'' \times 15''$. In the SMA images, the large dashed circles with a diameter of $14''.5$ represent the JCMT beam (FWHM); we use $1''$ -radius red circles to denote the SMA detections, and the ellipses at the bottom-right corners represent the synthesized beams. The red contours in the other images are $(3, 4, 5) \times \sigma$ isophotes of the SMA sources. This figure continues in the next page.

F435W, F606W, F814W, F110W, F140W, and F160W. We ran SExtractor in dual-image mode using F160W as the detection band to obtain AUTO magnitudes. The deblending parameters DEBLEND_NTHRESH and DEBLEND_MINCONT were again chosen to be 32 and 0.005, respectively. For SMA-5, F850LP is the only available *HST* passband. We took the IRAC 1.9''-radius aperture photometry from the *Spitzer* source catalog of A2390 and ran SExtractor in single-image mode to measure the AUTO magnitudes at F850LP and K_s . Before running BPZ, we corrected all the magnitudes for Galactic dust extinction from

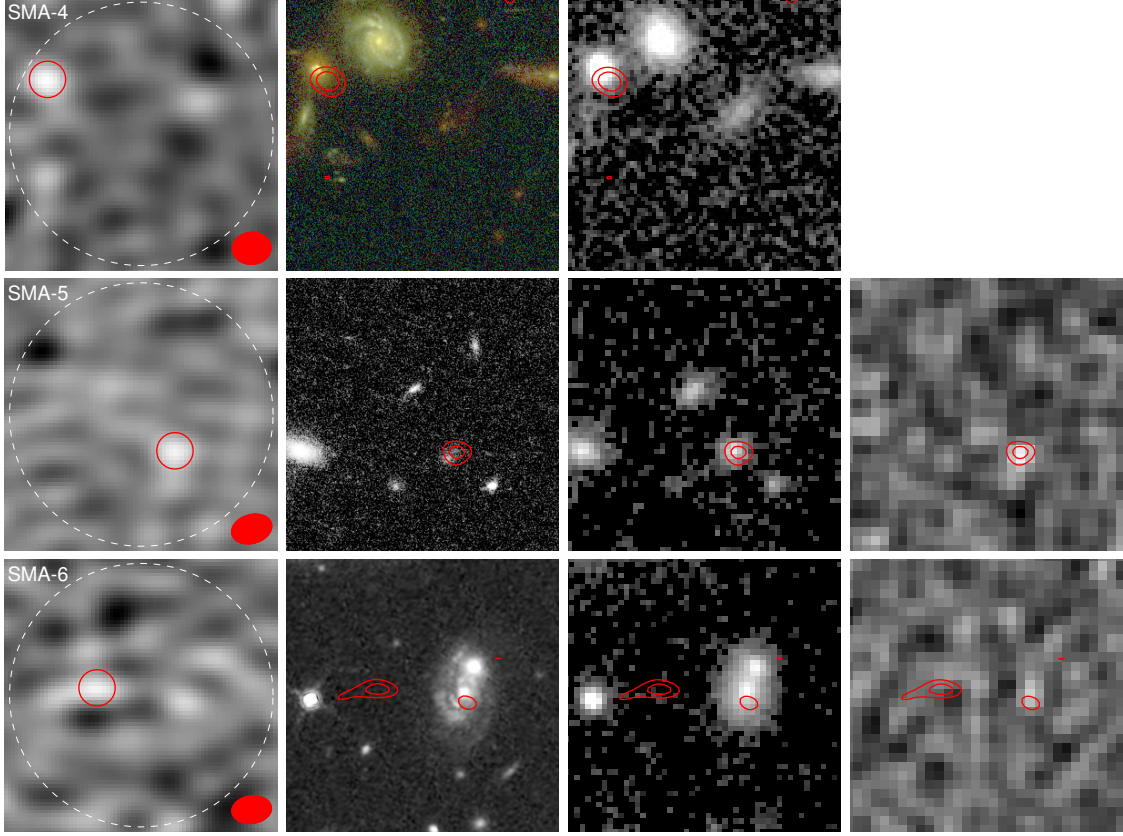


Figure 4.1: (Continued) From left to right are SMA 870 μm , *HST* (from top to bottom: F435W-F606W-F814W false color, F850LP, and F125W), CFHT/WIRCam K_s -band, and VLA 1.4 GHz images.

Schlafly & Finkbeiner (2011). We obtained $z = 2.39 \pm 0.17$ and 2.00 ± 0.15 for SMA-1 and SMA-5, respectively.

For SMA-2-1, SMA-2-2 and SMA-6, we used the submillimeter-to-radio flux ratios to compute their “millimetric redshifts”, following the method in Barger et al. (2000). The relation between the redshift and the submillimeter-to-radio flux ratio is

$$z = (S_{343\text{GHz}}/S_{1.4\text{GHz}})^{0.26} - 1 = 0.85(S_{343\text{GHz}}/S_{3\text{GHz}})^{0.26} - 1 \quad (4.1)$$

With $S_{3\text{GHz}} = 5.13 \pm 1.51 \mu\text{Jy}$ (Hsu et al. 2017), we obtained $z = 2.9 \pm 0.4$ for SMA-2-1. Because SMA-2-2 and SMA-6 are not detected in the radio images, we used their 3σ limits, 3.05 μJy (3 GHz) and 22.6 μJy (1.4 GHz), to compute the lower redshift limits. The results

are $z > 3.7$ and $z > 2.2$ for SMA-2-2 and SMA-6, respectively. Note that SMA-1 and SMA-5 are also detected at 1.4 GHz with $S_{1.4\text{GHz}} = 26.9 \pm 6.2 \mu\text{Jy}$ and $35.8 \pm 6.9 \mu\text{Jy}$, respectively. Their millimetric redshifts are 2.1 ± 0.3 and 2.0 ± 0.2 , respectively, in agreement with the photometric redshifts.

For the three SMA sources in A1689 and MACSJ1423, there are no deep radio images available. Because these sources are not detected in *HST*, K_s -band, or *Spitzer* images, we expect them to be at high redshifts. We assume a conservative lower limit at $z = 1.0$ to estimate their lensing magnifications, which we will describe in the next section.

4.3.3 Lens Models

In order to compute the magnifications and intrinsic flux densities of our faint SMGs, the lens models of the clusters and source redshifts are required. A set of lens models are available for the *HST* Frontier Fields from ten teams, including Bradac (Bradač et al. 2005, 2009; Hoag et al. 2016), Caminha (Caminha et al. 2017), CATS (Jullo & Kneib 2009; Jauzac et al. 2012, 2014, 2015b,a; Richard et al. 2014), Diego (Diego et al. 2005a,b, 2007, 2015), GLAFIC (Oguri 2010; Kawamata et al. 2016), Keeton (Keeton 2010; Ammons et al. 2014; McCully et al. 2014), Merten (Merten et al. 2009, 2011), Sharon (Jullo et al. 2007; Johnson et al. 2014), Williams (Liesenborgs et al. 2006; Mohammed et al. 2014; Grillo et al. 2015; Sebesta et al. 2016), and Zitrin (Zitrin et al. 2009, 2013).

For A1689, A2390, and MACSJ1423, we used the models from Limousin et al. (2007), Richard et al. (2010), and the CLASH archive, respectively. Both the Frontier Fields and CLASH archives provide a set of images to account for the full range (i.e., the uncertainty) of each model, and we used the newest model from each team. On the other hand, only the best-fit models⁵ are available for A1689 and A2390 by running the LENSTOOL software (Kneib et al. 1996). In Table 4.5, we tabulate the models we used for each cluster field.

Following Coe et al. (2015), we estimated the median and 68.3% range of the magnification values from Monte Carlo simulations. For each source, we propagated the

⁵<https://projets.lam.fr/projects/lenstool/wiki>

positional and redshift uncertainties, as well as the full range (except for A1689 and A2390) of all the available lens models. The positional uncertainties were measured using the MIRIAD IMFIT routine, and the typical values are $0.^{\prime\prime}1 \sim 0.^{\prime\prime}3$ in both right ascension and declination. To propagate the redshift uncertainties of SMA-2-1, SMA-2-2, SMA-3-1, SMA-3-2, SMA-4, and SMA-6, we used a uniform distribution between their lower limits and an upper limit at $z = 6$. The resulting magnification error for SMA-4 is very large, because the critical lines at $z = 1 - 6$ are close to this source. We therefore decided to only use $z > 1.0$ to compute the lower limit of its magnification. In Table 4.6, we summarize the redshifts, lensing magnifications, de-lensed submillimeter flux densities, and observed K_s -band magnitudes of the SMA sources.

4.4 Discussion

Five of our eight SMA sources are not detected in optical or NIR images. This agrees with Chen et al. (2014) and suggests that many faint SMGs are still missed by optical surveys and would not be included in the UV star formation history. However, studies of low-redshift starburst galaxies (e.g., Chary & Elbaz 2001; Le Floc'h et al. 2005; Reddy et al. 2010) have shown that fainter sources are generally less dusty. In addition, some recent work suggests that fainter SMGs are on average at lower redshifts (e.g., Heavens et al. 2004; Bundy et al. 2006; Franceschini et al. 2006; Dye et al. 2008; Mobasher et al. 2009; Magliocchetti et al. 2011; Hsu et al. 2016; Cowie et al. 2017). Based on these results, the NIR-to-submillimeter flux ratios of SMGs are expected to increase with decreasing luminosity/flux.

Recently, we have obtained different samples of SCUBA/SCUBA-2 sources followed up by the SMA (Chen et al. 2014; Cowie et al. 2017), ALMA (Cowie et. al., in preparation), or VLA (Cowie et al. 2017; Hsu et al. 2017). Since K_s -band imaging is available for these samples and this work, we can combine them and inspect the change of K_s -to-submillimeter flux ratio over a wide flux range. In Figure 4.2 (4.3), we show K_s -to-870 (850) μm flux ratio as a function of 870 (850) μm flux density for the submillimeter (radio) identified samples.

Table 4.5: Lens Models Used for Each Cluster Field

Field	Models
A370	Brada-c-v1 CATS-v1 Merten-v1 Sharon-v2 Williams-v2 Zitrin-LTM-v1 Zitrin-LTM-Gauss-v1 Zitrin-NFW-v1
MACSJ0717	Brada-c-v1 CATS-v4.1 Diego-v4.1 GLAFIC-v3 Keeton-v4
A1689	Merten-v1 Sharon-v4 Williams-v4 Zitrin-LTM-v1 Zitrin-LTM-Gauss-v1 Limousin et al. (2007)
MACSJ1423	Zitrin-LTM-Gauss-v2 Zitrin-NFW-v2
A2390	Richard et al. (2010)

Table 4.6: Redshifts, Lensing Magnifications, De-lensed Submillimeter Flux Densities, and Observed K_s -band Magnitudes of the SMA Sources

ID	z	μ	$S_{870,\text{int}}$ (mJy)	m_{K_s} (mag)
SMA-1	2.39 ± 0.17	$1.88^{+0.35}_{-0.36}$	1.14 ± 0.32	22.5
SMA-2-1	2.9 ± 0.4	$1.86^{+0.26}_{-0.49}$	$0.96^{+0.33}_{-0.25}$	24.4 ± 0.2
SMA-2-2	> 3.7	$2.09^{+0.34}_{-0.59}$	$1.03^{+0.35}_{-0.25}$	> 25.4
SMA-3-1	...	$2.81^{+0.10}_{-0.20}$	$0.76^{+0.20}_{-0.19}$	> 23.8
SMA-3-2	...	$3.31^{+0.15}_{-0.35}$	$0.75^{+0.19}_{-0.18}$	> 23.8
SMA-4	...	> 1.96	< 1.35	> 23.3
SMA-5	2.00 ± 0.15	2.09 ± 0.02	1.19 ± 0.27	21.4 ± 0.2
SMA-6	> 2.2	$3.96^{+0.12}_{-0.20}$	0.50 ± 0.11	> 24.0

The 1.1 mm lensed sources in the Frontier Fields from González-López et al. (2017) and the 1.3 mm sources in the Hubble Ultra Deep Field (HUDF; Beckwith et al. 2006) from Dunlop et al. (2017)⁶ are also included in Figure 4.2. We scaled their flux densities to 870 μm values using an Arp 220 SED (Silva et al. 1998) redshifted to their redshifts (Laporte et al. 2017; Dunlop et al. 2017). For example, the conversions are $S_{870\mu\text{m}}/S_{1.1\text{mm}} = 1.92$ and $S_{870\mu\text{m}}/S_{1.3\text{mm}} = 3.10$ for a source at $z = 2$. For the K_s -band photometry⁷, we ran SExtractor on the images from Brammer et al. (2016) and Fontana et al. (2014) for the 1.1 and 1.3 mm sources, respectively.

We can see in Figures 4.2 and 4.3 that most of the SMGs show a trend of increasing K_s -to-submillimeter flux ratios as we go from brighter to fainter sources. The 3 GHz-identified lensed SMGs from Hsu et al. (2017) and the faintest sources in the CDF-S ALMA sample (Cowie et. al., in preparation) occupy roughly the same space of the diagrams. However, the majority of SMA-detected lensed SMGs from Chen et al. (2014) and this work do not seem

⁶The final sample of Dunlop et al. (2017) consists of sixteen 3.5 σ -detected sources that have NIR counterparts in the *HST* image. This is a clean but biased sample, since any real source without a NIR counterpart is rejected. We therefore only include their five 6 σ -detected sources, which comprise a clean and unbiased sample.

⁷Two of the twelve 1.1 mm sources from González-López et al. (2017), A2744-ID02 and A2744-ID03, are seriously blended in the K_s -band image, so we did not measure their photometry. These two sources are therefore not included in Figures 4.2 and 4.4. Laporte et al. (2017) simply used a 0''.4-radius aperture with the IRAF NOAO daophot package and applied aperture corrections to measure the magnitudes for 11 of these sources. However, here we performed our own measurements with SExtractor instead of taking their results.

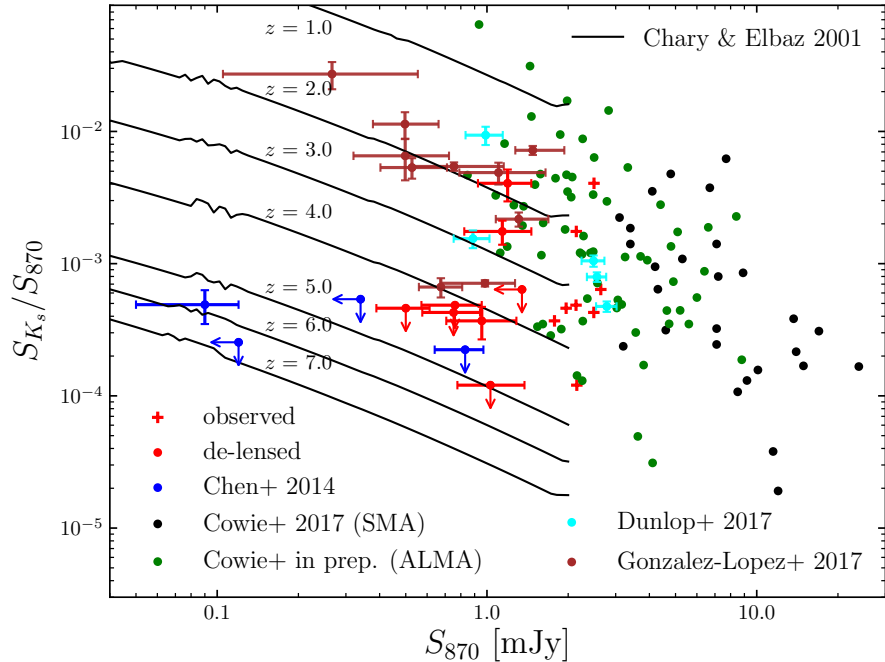


Figure 4.2: K_s -to-870 μm flux ratios versus 870 μm flux densities of our SMA-detected SMGs (red crosses: observed; red circles: de-lensed) and other samples. Blue circles represent SMA-detected lensed SMGs in A1689 and A2390 from Chen et al. (2014). Cyan circles are ALMA-detected 1.3 mm sources in HUDF from Dunlop et al. (2017), and we scaled their flux densities to 870 μm values assuming an Arp 220 SED (Silva et al. 1998). ALMA-detected lensed SMGs from González-López et al. (2017) are shown in brown, where we again used an Arp 220 SED to scale their 1.1 mm flux densities to 870 μm values. The flux densities of Chen et al. (2014) and González-López et al. (2017) are corrected for lensing magnifications. Black circles are SMA-detected bright SMGs in CDF-N from Cowie et al. (2017). ALMA-detected SMGs in CDF-S (Cowie et. al., in preparation) are shown in green. The predictions based on the SED templates of Chary & Elbaz (2001) at various redshifts are plotted in black curves. There is a trend of increasing K_s -to-870 μm flux ratio with decreasing flux density for most of the sources. However, the majority of SMA-detected lensed SMGs do not follow the same trend.

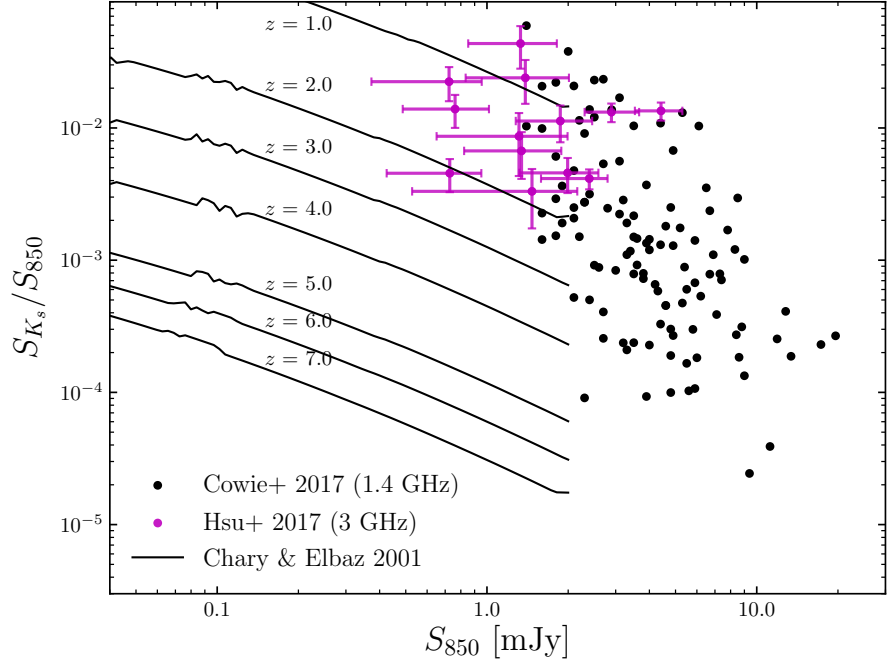


Figure 4.3: K_s -to-850 μm flux ratios versus SCUBA-2 850 μm flux densities of the bright SMGs identified with VLA 1.4 GHz in CDF-N (black) from Cowie et al. (2017) and the lensed SMGs identified with VLA 3 GHz (purple) from Hsu et al. (2017). Note that one of the 14 sources (0717–2) in Hsu et al. (2017) is removed because it corresponds to SMA-2-1 in this work. The predictions based on the SED templates of Chary & Elbaz (2001) at various redshifts are plotted in black curves.

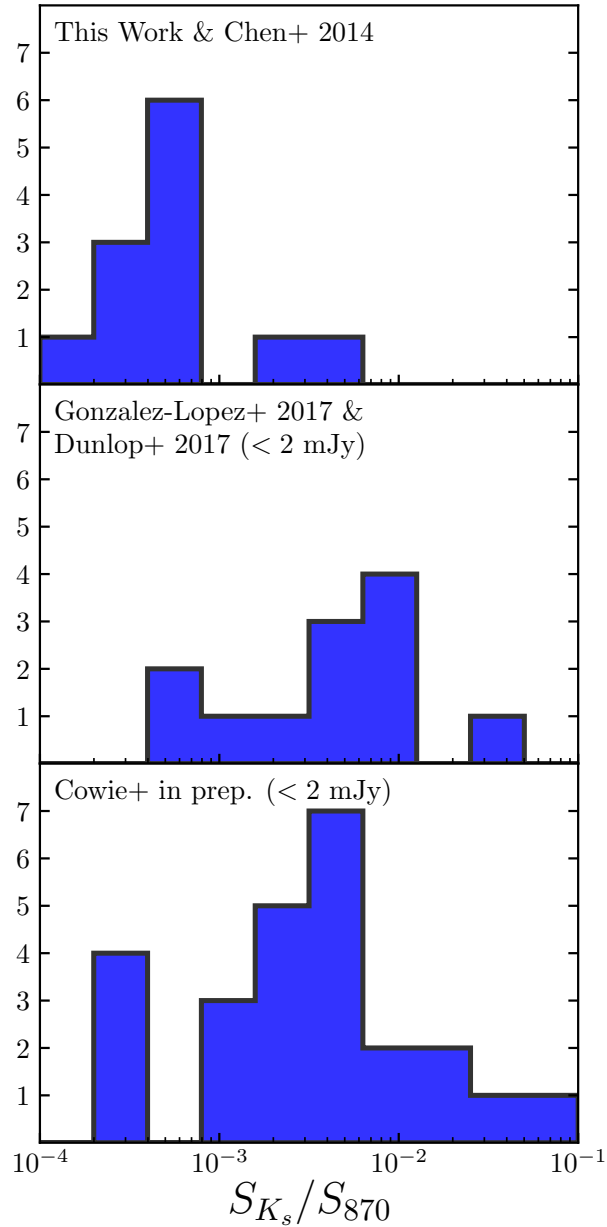


Figure 4.4: Histograms of the K_s -to-870 μm flux ratios for various samples of faint SMGs. Top: SMA-detected sources from this work and Chen et al. (2014). Middle: González-López et al. (2017) and the sources that are fainter than 2 mJy from Dunlop et al. (2017), with the flux densities scaled to 870 μm values. Bottom: the sources that are fainter than 2 mJy from Cowie et. al. (in preparation). The median (de-lensed) 870 μm flux densities for these samples are 0.80, 0.82, and 1.54 mJy, respectively. A K-S test suggests that the top and middle samples are not drawn from the same distribution.

to be drawn from the same population to which the other samples belong. In Figure 4.4, we compare the distributions of the K_s -to-870 μm flux ratios for the SMA-detected lensed SMGs from this work and Chen et al. (2014), the ALMA-detected lensed 1.1 mm sources (González-López et al. 2017) and 1.3 mm sources (Dunlop et al. 2017) that are fainter than 2 mJy at 870 μm , and the ALMA-detected blank-field SMGs (Cowie et. al., in preparation) that are fainter than 2 mJy. The median (de-lensed) 870 μm flux densities for these three samples are 0.80, 0.82, and 1.54 mJy, respectively. A K-S test for the first and the second samples results in a p -value < 0.001 and therefore suggests that they are not drawn from the same distribution. Note that SMA-1 and SMA-5, the two sources that have the highest K_s -to-870 μm flux ratios among our SMA sample (see Figures 4.2 and 4.4), are both detected at 1.4 GHz above a 4σ level.

We can see a bimodal color distribution in the left side of Figure 4.2. This suggests that besides optically bright and/or low-redshift sources, there is a population of faint SMGs that are extremely dusty and/or at very high redshifts. However, based on the K-S test, there might be a selection bias in our SMA samples. These sources were chosen for SMA observations because they were candidates to be highly magnified SMGs, especially for the ones of Chen et al. (2014). Because galaxies at higher redshifts have a higher probability of being lensed and generally have higher magnifications (e.g., Hezaveh & Holder 2011), these SMA-detected sources might not be a representative sample of faint SMGs either. ALMA imaging of our SCUBA-2 sources in the cluster centers will be the best approach to obtain a large and even sample of faint SMGs. Given the efficiency of ALMA observations, other pre-selections based on magnifications or observed flux densities are not required. As a consequence, we will be able to decide whether the bimodality we observe here really exists.

4.5 Summary

We carried out SMA observations of six intrinsically faint 850 μm sources detected by SCUBA-2 in lensing cluster fields, A1689, A2390, A370, MACS J0717.5+3745, and

MACS J1423.8+2404, yielding a total of eight SMA detections. Two of the SCUBA-2 sources split into doublets. Based on the lens models from the literature, the intrinsic 870 μm flux densities of these SMGs are ~ 1 mJy. Five of the sources have no optical or NIR counterparts. The NIR-to-submillimeter flux ratios of these faint SMGs suggest that most of them are extremely dusty and/or at very high redshifts. Combining this work and several other samples of SMGs identified with ALMA or SMA, we found a bimodal distribution for the faint sources in the space of submillimeter flux versus NIR-to-submillimeter flux ratio. However, there might be a selection bias in the SMA-detected lensed sources (this work and Chen et al. 2014). Future ALMA observations of a large sample of SCUBA-2 sources in cluster fields will allow us to decide whether the bimodality we observe here really exists.

References

- Ammons, S. M., Wong, K. C., Zabludoff, A. I., & Keeton, C. R. 2014, ApJ, 781, 2
- Barger, A. J., Cowie, L. L., Chen, C.-C., Owen, F. N., Wang, W.-H., Casey, C. M., Lee, N., Sanders, D. B., & Williams, J. P. 2014, ApJ, 784, 9
- Barger, A. J., Cowie, L. L., & Richards, E. A. 2000, AJ, 119, 2092
- Beckwith, S. V. W., Stiavelli, M., Koekemoer, A. M., Caldwell, J. A. R., Ferguson, H. C., Hook, R., Lucas, R. A., Bergeron, L. E., Corbin, M., Jogee, S., Panagia, N., Robberto, M., Royle, P., Somerville, R. S., & Sosey, M. 2006, AJ, 132, 1729
- Benítez, N. 2000, ApJ, 536, 571
- Bertin, E. & Arnouts, S. 1996, A&AS, 117, 393
- Bertin, E., Mellier, Y., Radovich, M., Missonnier, G., Didelon, P., & Morin, B. 2002, in Astronomical Society of the Pacific Conference Series, Vol. 281, Astronomical Data Analysis Software and Systems XI, ed. D. A. Bohlender, D. Durand, & T. H. Handley, 228
- Bradač, M., Schneider, P., Lombardi, M., & Erben, T. 2005, A&A, 437, 39
- Bradač, M., Treu, T., Applegate, D., Gonzalez, A. H., Clowe, D., Forman, W., Jones, C., Marshall, P., Schneider, P., & Zaritsky, D. 2009, ApJ, 706, 1201

- Brammer, G. B., Marchesini, D., Labb  , I., Spitler, L., Lange-Vagle, D., Barker, E. A., Tanaka, M., Fontana, A., Galametz, A., Ferr  -Mateu, A., Kodama, T., Lundgren, B., Martis, N., Muzzin, A., Stefanon, M., Toft, S., van der Wel, A., Vulcani, B., & Whitaker, K. E. 2016, ApJS, 226, 6
- Bruzual, G. & Charlot, S. 2003, MNRAS, 344, 1000
- Bundy, K., Ellis, R. S., Conselice, C. J., Taylor, J. E., Cooper, M. C., Willmer, C. N. A., Weiner, B. J., Coil, A. L., Noeske, K. G., & Eisenhardt, P. R. M. 2006, ApJ, 651, 120
- Caminha, G. B., Grillo, C., Rosati, P., Balestra, I., Mercurio, A., Vanzella, E., Biviano, A., Caputi, K. I., Delgado-Correal, C., Karman, W., Lombardi, M., Meneghetti, M., Sartoris, B., & Tozzi, P. 2017, A&A, 600, A90
- Chabrier, G. 2003, PASP, 115, 763
- Chary, R. & Elbaz, D. 2001, ApJ, 556, 562
- Chen, C.-C., Cowie, L. L., Barger, A. J., Casey, C. M., Lee, N., Sanders, D. B., Wang, W.-H., & Williams, J. P. 2013, ApJ, 776, 131
- Chen, C.-C., Cowie, L. L., Barger, A. J., Wang, W.-H., & Williams, J. P. 2014, ApJ, 789, 12
- Chen, C.-C., Smail, I., Swinbank, A. M., Simpson, J. M., Ma, C.-J., Alexander, D. M., Biggs, A. D., Brandt, W. N., Chapman, S. C., Coppin, K. E. K., Danielson, A. L. R., Dannerbauer, H., Edge, A. C., Greve, T. R., Ivison, R. J., Karim, A., Menten, K. M., Schinnerer, E., Walter, F., Wardlow, J. L., Wei  , A., & van der Werf, P. P. 2015, ApJ, 799, 194
- Coe, D., Bradley, L., & Zitrin, A. 2015, ApJ, 800, 84
- Condon, J. J. 1974, ApJ, 188, 279
- . 1992, ARA&A, 30, 575

Cowie, L. L., Barger, A. J., Hsu, L.-Y., Chen, C.-C., Owen, F. N., & Wang, W.-H. 2017, ApJ, 837, 139

Diego, J. M., Broadhurst, T., Benitez, N., Umetsu, K., Coe, D., Sendra, I., Sereno, M., Izzo, L., & Covone, G. 2015, MNRAS, 446, 683

Diego, J. M., Protopapas, P., Sandvik, H. B., & Tegmark, M. 2005a, MNRAS, 360, 477

Diego, J. M., Sandvik, H. B., Protopapas, P., Tegmark, M., Benítez, N., & Broadhurst, T. 2005b, MNRAS, 362, 1247

Diego, J. M., Tegmark, M., Protopapas, P., & Sandvik, H. B. 2007, MNRAS, 375, 958

Dunlop, J. S., McLure, R. J., Biggs, A. D., Geach, J. E., Michałowski, M. J., Ivison, R. J., Rujopakarn, W., van Kampen, E., Kirkpatrick, A., Pope, A., Scott, D., Swinbank, A. M., Targett, T. A., Arétxaga, I., Austermann, J. E., Best, P. N., Bruce, V. A., Chapin, E. L., Charlot, S., Cirasuolo, M., Coppin, K., Ellis, R. S., Finkelstein, S. L., Hayward, C. C., Hughes, D. H., Ibar, E., Jagannathan, P., Khochfar, S., Koprowski, M. P., Narayanan, D., Nyland, K., Papovich, C., Peacock, J. A., Rieke, G. H., Robertson, B., Vernstrom, T., Werf, P. P. v. d., Wilson, G. W., & Yun, M. 2017, MNRAS, 466, 861

Dye, S., Eales, S. A., Arétxaga, I., Serjeant, S., Dunlop, J. S., Babbedge, T. S. R., Chapman, S. C., Cirasuolo, M., Clements, D. L., Coppin, K. E. K., Dunne, L., Egami, E., Farrah, D., Ivison, R. J., van Kampen, E., Pope, A., Priddey, R., Rieke, G. H., Schael, A. M., Scott, D., Simpson, C., Takagi, T., Takata, T., & Vaccari, M. 2008, MNRAS, 386, 1107

Eddington, A. S. 1913, MNRAS, 73, 359

Fontana, A., Dunlop, J. S., Paris, D., Targett, T. A., Boutsia, K., Castellano, M., Galametz, A., Grazian, A., McLure, R., Merlin, E., Pentericci, L., Wuyts, S., Almaini, O., Caputi, K., Chary, R.-R., Cirasuolo, M., Conselice, C. J., Cooray, A., Daddi, E., Dickinson, M., Faber, S. M., Fazio, G., Ferguson, H. C., Giallongo, E., Giavalisco, M., Grogin, N. A., Hathi, N., Koekemoer, A. M., Koo, D. C., Lucas, R. A., Nonino, M., Rix, H. W., Renzini,

- A., Rosario, D., Santini, P., Scarlata, C., Sommariva, V., Stark, D. P., van der Wel, A., Vanzella, E., Wild, V., Yan, H., & Zibetti, S. 2014, *A&A*, 570, A11
- Franceschini, A., Rodighiero, G., Cassata, P., Berta, S., Vaccari, M., Nonino, M., Vanzella, E., Hatziminaoglou, E., Antichi, J., & Cristiani, S. 2006, *A&A*, 453, 397
- González-López, J., Bauer, F. E., Romero-Cañizales, C., Kneissl, R., Villard, E., Carvajal, R., Kim, S., Laporte, N., Anguita, T., Aravena, M., Bouwens, R. J., Bradley, L., Carrasco, M., Demarco, R., Ford, H., Ibar, E., Infante, L., Messias, H., Muñoz Arancibia, A. M., Nagar, N., Padilla, N., Treister, E., Troncoso, P., & Zitrin, A. 2017, *A&A*, 597, A41
- Grillo, C., Suyu, S. H., Rosati, P., Mercurio, A., Balestra, I., Munari, E., Nonino, M., Caminha, G. B., Lombardi, M., De Lucia, G., Borgani, S., Gobat, R., Biviano, A., Girardi, M., Umetsu, K., Coe, D., Koekemoer, A. M., Postman, M., Zitrin, A., Halkola, A., Broadhurst, T., Sartoris, B., Presotto, V., Annunziatella, M., Maier, C., Fritz, A., Vanzella, E., & Frye, B. 2015, *ApJ*, 800, 38
- Heavens, A., Panter, B., Jimenez, R., & Dunlop, J. 2004, *Nature*, 428, 625
- Helou, G., Soifer, B. T., & Rowan-Robinson, M. 1985, *ApJ*, 298, L7
- Hezaveh, Y. D. & Holder, G. P. 2011, *ApJ*, 734, 52
- Hoag, A., Huang, K.-H., Treu, T., Bradač, M., Schmidt, K. B., Wang, X., Brammer, G. B., Broussard, A., Amorin, R., Castellano, M., Fontana, A., Merlin, E., Schrabbach, T., Trenti, M., & Vulcani, B. 2016, *ApJ*, 831, 182
- Hodge, J. A., Carilli, C. L., Walter, F., de Blok, W. J. G., Riechers, D., Daddi, E., & Lentati, L. 2012, *ApJ*, 760, 11
- Hodge, J. A., Swinbank, A. M., Simpson, J. M., Smail, I., Walter, F., Alexander, D. M., Bertoldi, F., Biggs, A. D., Brandt, W. N., Chapman, S. C., Chen, C. C., Coppin, K. E. K., Cox, P., Dannerbauer, H., Edge, A. C., Greve, T. R., Ivison, R. J., Karim, A., Knudsen,

K. K., Menten, K. M., Rix, H.-W., Schinnerer, E., Wardlow, J. L., Weiss, A., & van der Werf, P. 2016, ApJ, 833, 103

Hsu, L.-Y., Cowie, L. L., Chen, C.-C., Barger, A. J., & Wang, W.-H. 2016, ApJ, 829, 25

Hsu, L.-Y., Desai, V., Murphy, E. J., Cowie, L. L., Heywood, I., Momjian, E., Barger, A. J., & Smail, I. 2017, ApJ, 840, 29

Jauzac, M., Clément, B., Limousin, M., Richard, J., Jullo, E., Ebeling, H., Atek, H., Kneib, J.-P., Knowles, K., Natarajan, P., Eckert, D., Egami, E., Massey, R., & Rexroth, M. 2014, MNRAS, 443, 1549

Jauzac, M., Jullo, E., Eckert, D., Ebeling, H., Richard, J., Limousin, M., Atek, H., Kneib, J.-P., Clément, B., Egami, E., Harvey, D., Knowles, K., Massey, R., Natarajan, P., & Rexroth, M. 2015a, MNRAS, 446, 4132

Jauzac, M., Jullo, E., Kneib, J.-P., Ebeling, H., Leauthaud, A., Ma, C.-J., Limousin, M., Massey, R., & Richard, J. 2012, MNRAS, 426, 3369

Jauzac, M., Richard, J., Jullo, E., Clément, B., Limousin, M., Kneib, J.-P., Ebeling, H., Natarajan, P., Rodney, S., Atek, H., Massey, R., Eckert, D., Egami, E., & Rexroth, M. 2015b, MNRAS, 452, 1437

Johnson, T. L., Sharon, K., Bayliss, M. B., Gladders, M. D., Coe, D., & Ebeling, H. 2014, ApJ, 797, 48

Jullo, E. & Kneib, J.-P. 2009, MNRAS, 395, 1319

Jullo, E., Kneib, J.-P., Limousin, M., Elíasdóttir, Á., Marshall, P. J., & Verdugo, T. 2007, New Journal of Physics, 9, 447

Kawamata, R., Oguri, M., Ishigaki, M., Shimasaku, K., & Ouchi, M. 2016, ApJ, 819, 114

Keeton, C. R. 2010, General Relativity and Gravitation, 42, 2151

Kneib, J.-P., Ellis, R. S., Smail, I., Couch, W. J., & Sharples, R. M. 1996, ApJ, 471, 643

- Laporte, N., Bauer, F. E., Troncoso-Iribarren, P., Huang, X., González-López, J., Kim, S., Anguita, T., Aravena, M., Barrientos, L. F., Bouwens, R., Bradley, L., Brammer, G., Carrasco, M., Carvajal, R., Coe, D., Demarco, R., Ellis, R. S., Ford, H., Francke, H., Ibar, E., Infante, L., Kneissl, R., Koekemoer, A. M., Messias, H., Muñoz-Arcibia, A., Nagar, N., Padilla, N., Pelló, R., Postman, M., Quénard, D., Romero-Cañizales, C., Treister, E., Villard, E., Zheng, W., & Zitrin, A. 2017, ArXiv e-prints
- Le Floc'h, E., Papovich, C., Dole, H., Bell, E. F., Lagache, G., Rieke, G. H., Egami, E., Pérez-González, P. G., Alonso-Herrero, A., Rieke, M. J., Blaylock, M., Engelbracht, C. W., Gordon, K. D., Hines, D. C., Misselt, K. A., Morrison, J. E., & Mould, J. 2005, ApJ, 632, 169
- Liesenborgs, J., De Rijcke, S., & Dejonghe, H. 2006, MNRAS, 367, 1209
- Limousin, M., Richard, J., Jullo, E., Kneib, J.-P., Fort, B., Soucail, G., Elíasdóttir, Á., Natarajan, P., Ellis, R. S., Smail, I., Czoske, O., Smith, G. P., Hudelot, P., Bardeau, S., Ebeling, H., Egami, E., & Knudsen, K. K. 2007, ApJ, 668, 643
- Magliocchetti, M., Santini, P., Rodighiero, G., Grazian, A., Aussel, H., Altieri, B., Andreani, P., Berta, S., Cepa, J., Castañeda, H., Cimatti, A., Daddi, E., Elbaz, D., Genzel, R., Gruppioni, C., Lutz, D., Magnelli, B., Maiolino, R., Popesso, P., Poglitsch, A., Pozzi, F., Sanchez-Portal, M., Förster Schreiber, N. M., Sturm, E., Tacconi, L., & Valtchanov, I. 2011, MNRAS, 416, 1105
- McCully, C., Keeton, C. R., Wong, K. C., & Zabludoff, A. I. 2014, MNRAS, 443, 3631
- Merten, J., Cacciato, M., Meneghetti, M., Mignone, C., & Bartelmann, M. 2009, A&A, 500, 681
- Merten, J., Coe, D., Dupke, R., Massey, R., Zitrin, A., Cypriano, E. S., Okabe, N., Frye, B., Braglia, F. G., Jiménez-Teja, Y., Benítez, N., Broadhurst, T., Rhodes, J., Meneghetti, M., Moustakas, L. A., Sodré, Jr., L., Krick, J., & Bregman, J. N. 2011, MNRAS, 417, 333

Mobasher, B., Dahlen, T., Hopkins, A., Scoville, N. Z., Capak, P., Rich, R. M., Sanders, D. B., Schinnerer, E., Ilbert, O., Salvato, M., & Sheth, K. 2009, ApJ, 690, 1074

Mohammed, I., Liesenborgs, J., Saha, P., & Williams, L. L. R. 2014, MNRAS, 439, 2651

Oguri, M. 2010, PASJ, 62, 1017

Postman, M., Coe, D., Benítez, N., Bradley, L., Broadhurst, T., Donahue, M., Ford, H., Graur, O., Graves, G., Jouvel, S., Koekemoer, A., Lemze, D., Medezinski, E., Molino, A., Moustakas, L., Ogaz, S., Riess, A., Rodney, S., Rosati, P., Umetsu, K., Zheng, W., Zitrin, A., Bartelmann, M., Bouwens, R., Czakon, N., Golwala, S., Host, O., Infante, L., Jha, S., Jimenez-Teja, Y., Kelson, D., Lahav, O., Lazkoz, R., Maoz, D., McCully, C., Melchior, P., Meneghetti, M., Merten, J., Moustakas, J., Nonino, M., Patel, B., Regös, E., Sayers, J., Seitz, S., & Van der Wel, A. 2012, ApJS, 199, 25

Reddy, N. A., Erb, D. K., Pettini, M., Steidel, C. C., & Shapley, A. E. 2010, ApJ, 712, 1070

Richard, J., Jauzac, M., Limousin, M., Jullo, E., Clément, B., Ebeling, H., Kneib, J.-P., Atek, H., Natarajan, P., Egami, E., Livermore, R., & Bower, R. 2014, MNRAS, 444, 268

Richard, J., Smith, G. P., Kneib, J.-P., Ellis, R. S., Sanderson, A. J. R., Pei, L., Targett, T. A., Sand, D. J., Swinbank, A. M., Dannerbauer, H., Mazzotta, P., Limousin, M., Egami, E., Jullo, E., Hamilton-Morris, V., & Moran, S. M. 2010, MNRAS, 404, 325

Sault, R. J., Teuben, P. J., & Wright, M. C. H. 1995, in Astronomical Society of the Pacific Conference Series, Vol. 77, Astronomical Data Analysis Software and Systems IV, ed. R. A. Shaw, H. E. Payne, & J. J. E. Hayes, 433

Schlafly, E. F. & Finkbeiner, D. P. 2011, ApJ, 737, 103

Sebesta, K., Williams, L. L. R., Mohammed, I., Saha, P., & Liesenborgs, J. 2016, MNRAS, 461, 2126

- Silva, L., Granato, G. L., Bressan, A., & Danese, L. 1998, ApJ, 509, 103
- Wang, W.-H., Cowie, L. L., Barger, A. J., Keenan, R. C., & Ting, H.-C. 2010, ApJS, 187, 251
- Wold, I. G. B., Owen, F. N., Wang, W.-H., Barger, A. J., & Keenan, R. C. 2012, ApJS, 202, 2
- Zavala, J. A., Artxaga, I., Geach, J. E., Hughes, D. H., Birkinshaw, M., Chapin, E., Chapman, S., Chen, C.-C., Clements, D. L., Dunlop, J. S., Farrah, D., Ivison, R. J., Jenness, T., Michałowski, M. J., Robson, E. I., Scott, D., Simpson, J., Spaans, M., & van der Werf, P. 2017, MNRAS, 464, 3369
- Zitrin, A., Broadhurst, T., Umetsu, K., Coe, D., Benítez, N., Ascaso, B., Bradley, L., Ford, H., Jee, J., Medezinski, E., Rephaeli, Y., & Zheng, W. 2009, MNRAS, 396, 1985
- Zitrin, A., Meneghetti, M., Umetsu, K., Broadhurst, T., Bartelmann, M., Bouwens, R., Bradley, L., Carrasco, M., Coe, D., Ford, H., Kelson, D., Koekemoer, A. M., Medezinski, E., Moustakas, J., Moustakas, L. A., Nonino, M., Postman, M., Rosati, P., Seidel, G., Seitz, S., Sendra, I., Shu, X., Vega, J., & Zheng, W. 2013, ApJ, 762, L30

Chapter 5

Conclusions and Future Directions

Even at ~ 2 mJy at $850 \mu\text{m}$, the number density of SMGs is only ~ 1 per arcmin^2 (Hsu et al. 2016). Therefore, it is much more efficient to select samples using single-dish telescopes (at least down to their confusion limits) than to use mosaics of small field-of-view interferometric observations (e.g., González-López et al. 2017; Dunlop et al. 2017). ALMA follow-up observations can be done based on the priors determined from single-dish surveys. Our Hawaii SCUBA-2 Lensing Cluster Survey has constructed a large sample of faint SMGs for this study.

Combining deep SCUBA-2 data for multiple fields, we computed the EBL at 450 and $850 \mu\text{m}$ down to very faint flux densities, which are otherwise not accessible from blank-field observations. We showed that LIRGs and normal galaxies selected at optical/NIR wavelengths cannot fully account for the EBL that originates from sources with $L_{\text{IR}} < 10^{12} L_{\odot}$. This suggests that many faint SMGs may not be included in the UV star formation history. A statistical analysis on the $450 \mu\text{m}$ -to- $850 \mu\text{m}$ flux ratio indicates that SMGs at higher redshifts generally have higher luminosities.

We characterized individual sources with their positions determined by the VLA and SMA. Our radio-detected faint SMGs are mostly low-redshift sources that are bright in the optical/NIR; they have lower dust temperatures and therefore different SED shapes than those of the bright SMGs. On the other hand, our SMA sample consists of mostly very dusty and/or high-redshift faint galaxies; their distribution in the space of submillimeter flux

versus NIR-to-submillimeter color does not follow the trend that the brighter SMGs have. However, all these results require further confirmation based on a large unbiased sample of lensed SMGs identified with ALMA. We are awarded ALMA 7 imaging of a sample of SCUBA-2 sources detected within the *HST*/ACS footprints of four Frontier Fields, A370, MACSJ0416, MACSJ0717, and MACSJ1149. The rich multi-wavelength data for these fields will allow us to tightly constrain the properties of the ALMA-detected sources.

With the current capabilities of ALMA, spectroscopic surveys will be the critical next step to further characterize faint SMGs. Because many SMGs are faint at optical/NIR wavelengths, it is not possible to measure their photometric or spectroscopic redshifts. ALMA line-scans will detect the atomic or molecular lines of these sources, providing their redshift distribution and precise physical constraints. For example, some previous studies had successfully used ALMA to detect [CII] emission from ULIRGs ($L_{\text{IR}} > 10^{12} L_{\odot}$) at $z > 4$ (e.g., Swinbank et al. 2012; Carilli et al. 2013; Aravena et al. 2016); even fainter galaxies are detected in lensed fields (e.g., Knudsen et al. 2016; Bradač et al. 2016). Additionally, as the dominant cooling lines for the diffuse interstellar medium (ISM), [CII] detections can provide an insight to the gas cooling process in SMGs.

Detections of CO lines explore the properties of molecular gas (e.g., Carilli & Walter 2013), which traces H₂ gas and star formation (Kennicutt 1989). The ALMA Spectroscopic Survey (ASPECS; Walter et al. 2016) recently observed the Hubble Ultra Deep Field (HUDF; Beckwith et al. 2006) at ALMA band 3 and band 6, allowing the detections of CO transitions over a wide redshift range. The Next Generation Very Large Array (ngVLA) and the future ALMA band 1 receivers (35–52 GHz; Di Francesco et al. 2013) will be able to detect low-J CO lines in high-redshift galaxies, which are more sensitive to the total gas mass.

The maps of atomic or molecular lines also serve as gas dynamic tracers for us to measure the sizes, morphologies and rotation of ISM (e.g., Wang et al. 2013; Rawle et al. 2014; Oteo et al. 2016). The morphologies and kinematics of these SMGs allow us to understand the gas fueling mechanisms and to find their connections to the formation of

massive quiescent galaxies (e.g., Simpson et al. 2014; Chen et al. 2015; Hodge et al. 2016). With ALMA’s sub-arcsecond resolution, we can study the dust and gas components of SMGs at kpc scales. These results can be compared with the stellar sizes and morphologies measured in optical/NIR images, which will help us determine whether these systems are triggered by major mergers or fed by cold flow.

A lot of future observations can be done to improve our understanding of SMGs. The important questions we might address in the next few years include (1) what is the redshift distribution of SMGs, (2) the fraction of faint SMGs that are detected in the rest-frame UV as a function of flux and redshift, and how it determines the cosmic star formation history, and (3) what can we learn about the formation of SMGs from the sizes, morphologies and dynamics of their gas, dust, and stellar components.

References

- Aravena, M., Decarli, R., Walter, F., Bouwens, R., Oesch, P. A., Carilli, C. L., Bauer, F. E., Da Cunha, E., Daddi, E., Gómez-López, J., Ivison, R. J., Riechers, D. A., Smail, I., Swinbank, A. M., Weiss, A., Anguita, T., Bacon, R., Bell, E., Bertoldi, F., Cortes, P., Cox, P., Hodge, J., Ibar, E., Inami, H., Infante, L., Karim, A., Magnelli, B., Ota, K., Popping, G., van der Werf, P., Wagg, J., & Fudamoto, Y. 2016, ApJ, 833, 71
- Beckwith, S. V. W., Stiavelli, M., Koekemoer, A. M., Caldwell, J. A. R., Ferguson, H. C., Hook, R., Lucas, R. A., Bergeron, L. E., Corbin, M., Jogee, S., Panagia, N., Robberto, M., Royle, P., Somerville, R. S., & Sosey, M. 2006, AJ, 132, 1729
- Bradač, M., Garcia-Appadoo, D., Huang, K.-H., Vallini, L., Finney, E., Hoag, A., Lemaux, B., Schmidt, K., Treu, T., Carilli, C., Dijkstra, M., Ferrara, A., Fontana, A., Jones, T., Ryan, R., & Wagg, J. 2016, ArXiv e-prints
- Carilli, C. L., Riechers, D., Walter, F., Maiolino, R., Wagg, J., Lentati, L., McMahon, R., & Wolfe, A. 2013, ApJ, 763, 120
- Carilli, C. L. & Walter, F. 2013, ARA&A, 51, 105
- Chen, C.-C., Smail, I., Swinbank, A. M., Simpson, J. M., Ma, C.-J., Alexander, D. M., Biggs, A. D., Brandt, W. N., Chapman, S. C., Coppin, K. E. K., Danielson, A. L. R., Dannerbauer, H., Edge, A. C., Greve, T. R., Ivison, R. J., Karim, A., Menten, K. M., Schinnerer, E., Walter, F., Wardlow, J. L., Weiβ, A., & van der Werf, P. P. 2015, ApJ, 799, 194

Di Francesco, J., Johnstone, D., Matthews, B. C., Bartel, N., Bronfman, L., Casassus, S., Chitsazzadeh, S., Chou, H., Cunningham, M., Duchene, G., Geisbuesch, J., Hales, A., Ho, P. T. P., Houde, M., Iono, D., Kemper, F., Kepley, A., Koch, P. M., Kohno, K., Kothes, R., Lai, S.-P., Lin, K. Y., Liu, S.-Y., Mason, B., Maccarone, T. J., Mizuno, N., Morata, O., Schieven, G., Scaife, A. M. M., Scott, D., Shang, H., Shimojo, M., Su, Y.-N., Takakuwa, S., Wagg, J., Wootten, A., & Yusef-Zadeh, F. 2013, ArXiv e-prints

Dunlop, J. S., McLure, R. J., Biggs, A. D., Geach, J. E., Michałowski, M. J., Ivison, R. J., Rujopakarn, W., van Kampen, E., Kirkpatrick, A., Pope, A., Scott, D., Swinbank, A. M., Targett, T. A., Artxaga, I., Austermann, J. E., Best, P. N., Bruce, V. A., Chapin, E. L., Charlot, S., Cirasuolo, M., Coppin, K., Ellis, R. S., Finkelstein, S. L., Hayward, C. C., Hughes, D. H., Ibar, E., Jagannathan, P., Khochfar, S., Koprowski, M. P., Narayanan, D., Nyland, K., Papovich, C., Peacock, J. A., Rieke, G. H., Robertson, B., Vernstrom, T., Werf, P. P. v. d., Wilson, G. W., & Yun, M. 2017, MNRAS, 466, 861

González-López, J., Bauer, F. E., Romero-Cañizales, C., Kneissl, R., Villard, E., Carvajal, R., Kim, S., Laporte, N., Anguita, T., Aravena, M., Bouwens, R. J., Bradley, L., Carrasco, M., Demarco, R., Ford, H., Ibar, E., Infante, L., Messias, H., Muñoz Arancibia, A. M., Nagar, N., Padilla, N., Treister, E., Troncoso, P., & Zitrin, A. 2017, A&A, 597, A41

Hodge, J. A., Swinbank, A. M., Simpson, J. M., Smail, I., Walter, F., Alexander, D. M., Bertoldi, F., Biggs, A. D., Brandt, W. N., Chapman, S. C., Chen, C. C., Coppin, K. E. K., Cox, P., Dannerbauer, H., Edge, A. C., Greve, T. R., Ivison, R. J., Karim, A., Knudsen, K. K., Menten, K. M., Rix, H.-W., Schinnerer, E., Wardlow, J. L., Weiss, A., & van der Werf, P. 2016, ApJ, 833, 103

Hsu, L.-Y., Cowie, L. L., Chen, C.-C., Barger, A. J., & Wang, W.-H. 2016, ApJ, 829, 25

Kennicutt, Jr., R. C. 1989, ApJ, 344, 685

Knudsen, K. K., Richard, J., Kneib, J.-P., Jauzac, M., Clément, B., Drouart, G., Egami, E., & Lindroos, L. 2016, MNRAS, 462, L6

Oteo, I., Ivison, R. J., Dunne, L., Smail, I., Swinbank, A. M., Zhang, Z.-Y., Lewis, A., Maddox, S., Riechers, D., Serjeant, S., Van der Werf, P., Biggs, A. D., Bremer, M., Cigan, P., Clements, D. L., Cooray, A., Dannerbauer, H., Eales, S., Ibar, E., Messias, H., Michałowski, M. J., Pérez-Fournon, I., & van Kampen, E. 2016, ApJ, 827, 34

Rawle, T. D., Egami, E., Bussmann, R. S., Gurwell, M., Ivison, R. J., Boone, F., Combes, F., Danielson, A. L. R., Rex, M., Richard, J., Smail, I., Swinbank, A. M., Altieri, B., Blain, A. W., Clement, B., Dessauges-Zavadsky, M., Edge, A. C., Fazio, G. G., Jones, T., Kneib, J.-P., Omont, A., Pérez-González, P. G., Schaerer, D., Valtchanov, I., van der Werf, P. P., Walth, G., Zamojski, M., & Zemcov, M. 2014, ApJ, 783, 59

Simpson, J. M., Swinbank, A. M., Smail, I., Alexander, D. M., Brandt, W. N., Bertoldi, F., de Breuck, C., Chapman, S. C., Coppin, K. E. K., da Cunha, E., Danielson, A. L. R., Dannerbauer, H., Greve, T. R., Hodge, J. A., Ivison, R. J., Karim, A., Knudsen, K. K., Poggianti, B. M., Schinnerer, E., Thomson, A. P., Walter, F., Wardlow, J. L., Weiß, A., & van der Werf, P. P. 2014, ApJ, 788, 125

Swinbank, A. M., Karim, A., Smail, I., Hodge, J., Walter, F., Bertoldi, F., Biggs, A. D., de Breuck, C., Chapman, S. C., Coppin, K. E. K., Cox, P., Danielson, A. L. R., Dannerbauer, H., Ivison, R. J., Greve, T. R., Knudsen, K. K., Menten, K. M., Simpson, J. M., Schinnerer, E., Wardlow, J. L., Weiß, A., & van der Werf, P. 2012, MNRAS, 427, 1066

Walter, F., Decarli, R., Aravena, M., Carilli, C., Bouwens, R., da Cunha, E., Daddi, E., Ivison, R. J., Riechers, D., Smail, I., Swinbank, M., Weiss, A., Anguita, T., Assef, R., Bacon, R., Bauer, F., Bell, E. F., Bertoldi, F., Chapman, S., Colina, L., Cortes, P. C., Cox, P., Dickinson, M., Elbaz, D., Gómez-López, J., Ibar, E., Inami, H., Infante, L., Hodge, J., Karim, A., Le Fevre, O., Magnelli, B., Neri, R., Oesch, P., Ota, K., Popping,

G., Rix, H.-W., Sargent, M., Sheth, K., van der Wel, A., van der Werf, P., & Wagg, J. 2016, ApJ, 833, 67

Wang, R., Wagg, J., Carilli, C. L., Walter, F., Lentati, L., Fan, X., Riechers, D. A., Bertoldi, F., Narayanan, D., Strauss, M. A., Cox, P., Omont, A., Menten, K. M., Knudsen, K. K., Neri, R., & Jiang, L. 2013, ApJ, 773, 44

Appendix A

Simulations for Submillimeter Number Counts, Flux Ratios, and Source Plane Redshift Estimates

As we described in Section 2.3.3, we compared the measured submillimeter flux ratios with what we measured from the simulated maps for the cluster fields. In these simulations, we populated the pure noise maps with sources with constant flux ratios. In order to simulate maps for a cluster field, we need the underlying count model (de-lensed and Eddington-bias-corrected) to place sources on the source plane and then project them onto the image plane using LENSTOOL. However, what we tried to find out is the redshift of the source plane, which is also needed for measuring the de-lensed, corrected count model. Therefore, we measured the number counts and ran simulations in the following iterative way. We first located source planes at $z = 1.4$ at $450 \mu\text{m}$ (Roseboom et al. 2013) and $z = 3.0$ at $850 \mu\text{m}$ (Barger et al. 2012, 2014; Hayward et al. 2013; Vieira et al. 2013) to measure the number counts of all the cluster fields using the procedure we describe in Sections 2.3.4 and 2.3.5 (which also involved simulations). We then used the final count models we obtained and the assumed source plane redshifts to run simulations on the pure noise maps. To simulate the flux ratio measurement of 450 (850) μm selected sources, we generated sources on a source plane at $z = 1.4$ ($z = 3.0$) using the count model we measured, projected them onto the 450 (850) μm pure noise map at the image plane using LENSTOOL, and computed the flux of their 850 (450) μm counterparts based on the source plane redshift

and a modified blackbody SED with $\beta = 1.5$, $T = 40$ K. We then populated the 850 (450) μm pure noise map with these counterparts (which again includes lensing projection), and finally, we added additional sources onto the map until it matched the 850 (450) μm count model.

With all the simulated maps, we could measure the 850 μm -to-450 μm and 450 μm -to-850 μm flux ratios in the way we describe in Section 2.3.3. By doing the exercise we show in Figure 2.1, we found that our simulated 450 μm and 850 μm sources need to be redder and slightly bluer, respectively, to match what we measured from the real science maps. We therefore did a second iteration of the whole procedures above, with new input flux ratios and their corresponding source plane redshifts. It took us only three iterations to converge our source plane redshifts to $z = 2.2$ at 450 μm and $z = 2.8$ at 850 μm . We also used a dust temperature of 30 K or 50 K to run all the procedure above, which yielded to different source plane redshifts but still the same input flux ratios. With $T = 30$ K, the redshifts are $z \sim 1.5$ (450 μm) and $z \sim 2.0$ (850 μm); with $T = 50$ K, the redshifts are $z \sim 2.8$ (450 μm) and $z \sim 3.5$ (850 μm). In our simulations, although the spatial distribution of the lensed sources and the de-lensed, corrected count models are determined by the source plane redshift we used, it does not influence the flux ratio we measured. In other words, only the input constant flux ratio influence the result, even though we convert it to a redshift using a modified black body SED. In summary, Figures 2.1 and 2.2 were made after iterations of all the procedures we describe in Sections 2.3.3, 2.3.4 and 2.3.5.

In order to see how the image noise affect the flux ratio measurements in Figure 2.8, we again generated sources with constant flux ratios in our simulations. Figure A1 shows some examples for our cluster fields. We note that the measured flux ratios from the simulated maps are not constant as a function of the observed flux. We also found that the ratio between the input, constant value and the recovered value at a certain flux is rather independent of the input value. Therefore, we ran multiple simulations with different input constant values and calculated the averaged ratio between the input and recovered values

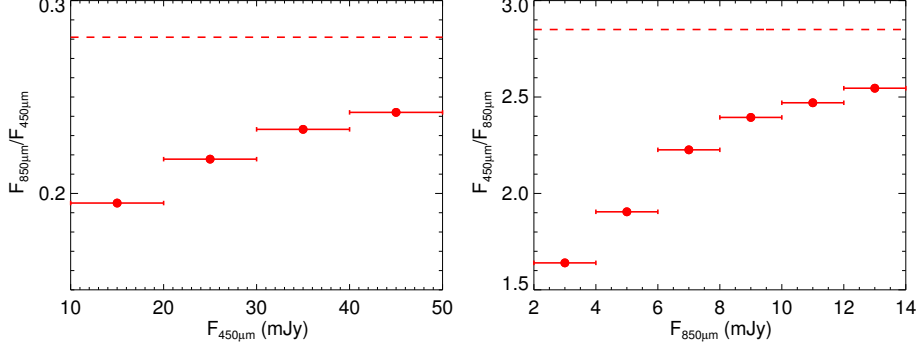


Figure A1: Input (dashed lines) and recovered median (filled circles) submillimeter flux ratios against the observed flux in our simulations for the 450 μm (left) and 850 μm selected sources (right) in our cluster fields. Here the input values are 0.281 and 2.85, which correspond to $z = 2.2$ and $z = 2.8$ for the 450 μm and 850 μm populations, respectively, based on a modified blackbody SED with $\beta = 1.5$, $T = 40$ K. The recovered flux ratio is measured using the method we describe in Section 2.3.3.

as a function of the flux. We then used the ratio to correct our measurements from the real science maps. The final corrected plots are what we show in Figure 2.8.

References

- Barger, A. J., Cowie, L. L., Chen, C.-C., Owen, F. N., Wang, W.-H., Casey, C. M., Lee, N., Sanders, D. B., & Williams, J. P. 2014, ApJ, 784, 9
- Barger, A. J., Wang, W.-H., Cowie, L. L., Owen, F. N., Chen, C.-C., & Williams, J. P. 2012, ApJ, 761, 89
- Hayward, C. C., Narayanan, D., Kereš, D., Jonsson, P., Hopkins, P. F., Cox, T. J., & Hernquist, L. 2013, MNRAS, 428, 2529
- Roseboom, I. G., Dunlop, J. S., Cirasuolo, M., Geach, J. E., Smail, I., Halpern, M., van der Werf, P., Almaini, O., Arumugam, V., Asboth, V., Auld, R., Blain, A., Bremer, M. N., Bock, J., Bowler, R. A. A., Buitrago, F., Chapin, E., Chapman, S., Chrysostomou, A., Clarke, C., Conley, A., Coppin, K. E. K., Danielson, A. L. R., Farrah, D., Glenn, J., Hatziminaoglou, E., Ibar, E., Ivison, R. J., Jenness, T., van Kampen, E., Karim, A., Mackenzie, T., Marsden, G., Meijerink, R., Michałowski, M. J., Oliver, S. J., Page, M. J., Pearson, E., Scott, D., Simpson, J. M., Smith, D. J. B., Spaans, M., Swinbank, A. M., Symeonidis, M., Targett, T., Valiante, E., Viero, M., Wang, L., Willott, C. J., & Zemcov, M. 2013, MNRAS, 436, 430
- Vieira, J. D., Marrone, D. P., Chapman, S. C., De Breuck, C., Hezaveh, Y. D., Weiβ, A., Aguirre, J. E., Aird, K. A., Aravena, M., Ashby, M. L. N., Bayliss, M., Benson, B. A., Biggs, A. D., Bleem, L. E., Bock, J. J., Bothwell, M., Bradford, C. M., Brodwin, M., Carlstrom, J. E., Chang, C. L., Crawford, T. M., Crites, A. T., de Haan, T., Dobbs,

M. A., Fomalont, E. B., Fassnacht, C. D., George, E. M., Gladders, M. D., Gonzalez, A. H., Greve, T. R., Gullberg, B., Halverson, N. W., High, F. W., Holder, G. P., Holzapfel, W. L., Hoover, S., Hrubes, J. D., Hunter, T. R., Keisler, R., Lee, A. T., Leitch, E. M., Lueker, M., Luong-van, D., Malkan, M., McIntyre, V., McMahon, J. J., Mehl, J., Menten, K. M., Meyer, S. S., Mocanu, L. M., Murphy, E. J., Natoli, T., Padin, S., Plagge, T., Reichardt, C. L., Rest, A., Ruel, J., Ruhl, J. E., Sharon, K., Schaffer, K. K., Shaw, L., Shirokoff, E., Spilker, J. S., Stalder, B., Staniszewski, Z., Stark, A. A., Story, K., Vanderlinde, K., Welikala, N., & Williamson, R. 2013, Nature, 495, 344